

**Spectroscopy of Neutron-Rich Nuclei Produced
in the Spontaneous Fission of ^{252}Cf**

by

Michael Wilhelm Simon

Submitted in Partial Fulfillment

of the

Requirements for the Degree

Doctor of Philosophy

Supervised by

Professor Douglas Cline

Department of Physics and Astronomy

The College

Arts and Sciences

University of Rochester

Rochester, New York

1999

To my Parents

Curriculum Vitae

The author was born in San Diego, California on October 5, 1964. He attended the University of California, Berkeley from 1982 to 1986 and worked at the UCB Earthquake Engineering Research Center and Fire Research Laboratory from 1985 to 1991. He attended San Francisco State University from 1988 to 1991 and graduated with a Bachelor of Science degree in Physics in 1991. During his enrollment he performed research on superconducting tunnel junctions under the direction of Professor Roger Bland. He entered the graduate physics program at the University of Rochester in the fall of 1991. He was awarded the Graduate Student Teaching Award in 1992 and received the Master of Arts degree in Physics in 1993. His dissertation research was carried out at the Nuclear Structure Research Laboratory under the direction of Professor Douglas Cline.

Acknowledgments

The research presented in this thesis represents not only my effort, but also the contributions of many people. I would like to extend thanks to all those involved.

I would like to thank first my advisor, Dr. Douglas Cline, for his continued support and encouragement. I would also like to thank Dr. Ching-Yen Wu for his a continued interest in this work and for innumerable useful discussions. Thanks are also due to the other members of the research group. Dr. Rich Ibbotson and Dr. Matt Devlin deserve thanks for their contributions and efforts in the ^{165}Ho experiment. The contributions of Robert Gray and Carl Welch in the development of CHICO and during experiments are also gratefully acknowledged.

Thanks are also due to the collaborators at LBNL and LLNL. Dr. Kai Vetter, Dr. A. O. Machiavelli, Dr. I. Y. Lee, Dr. Ken Gregorich, Dr. Steve Asztalos, and Dr. R. W. MacLeod contributed significantly by insuring that the CHICO plus GAMMASPHERE experiments were successful. I would also like to thank Dr. Jacob Gilat for his careful work with the data and for many discussions. Discussions with Dr. John Rasmussen are also gratefully acknowledged. Dr. Mark Stoyer deserves thanks for his efforts in suggesting the experiment, providing the fission source, and assistance during the course of this research.

The support offered by the staff at the Nuclear Structure Research Laboratory was invaluable. Thanks are due to Chris Long, Clint Cross, Ray Teng, Dave Munson, and Eileen Pullara.

Finally, I would like to thank my family and many friends for their support.

Abstract

A new experimental technique has been developed for the spectroscopic investigation of the neutron-rich products of $^{252}\text{Cf}(\text{SF})$. The charged-particle detector CHICO was coupled to the Ge-detector array GAMMASPHERE and a thin fission source was used allowing the collection of high-statistics, high-fold γ -ray data in kinematic coincidence with the recoiling fission partners. The selectivity provided by this technique allows the γ -rays to be assigned unambiguously to the heavy or light fission partner. The added sensitivity allows many rotational bands to be extended to $\sim 20 \hbar$, and a sensitivity to nuclei produced with a yield of 5×10^{-5} /fission was achieved by mass-gating the γ -ray spectra.

The charged-particle detector CHICO was developed for this experiment and for studies utilizing other binary reactions, such as Coulomb excitation, transfer and fusion-fission reactions. The detector covers a total solid angle of 2.8π sr and has a time resolution of 500 ps, resulting in a mass resolution of $\Delta m/m=5\%$ for beam experiments, or 8 mass units for spontaneous fission.

This technique was used to set limits, in agreement with shell model predictions, on the $E3$ decay of the $\frac{23}{2}^-$ level in ^{135}I . Rotational bands in $^{102,104,106,108}\text{Mo}$, ^{112}Ru , $^{152,154,156}\text{Nd}$, $^{156,158,160}\text{Sm}$ were extended to higher spin. Band crossings were observed in the ground and γ -band in ^{104}Mo . The γ -band of ^{112}Ru shows continued triaxial behavior at higher spin. The yrast rotational bands in $^{112,113,114,115,116}\text{Pd}$ were extended and rotational bands built on the low-lying isomeric levels in $^{113,115}\text{Pd}$ were newly identified. The behavior of the observed band crossings in the ground and isomer bands of $^{113,115}\text{Pd}$, when compared to the neighboring $^{111,113}\text{Rh}$ and cranked shell model calculations indicate that the predicted change from prolate to oblate shapes in the neutron-rich Pd does not occur before ^{116}Pd .

In a separate experiment, the lifetimes in ^{165}Ho of the $K = \frac{7}{2}^-$ ground band, up to spin $\frac{27}{2}^- \hbar$, and $K = \frac{11}{2}$ band, up to spin $\frac{19}{2}^- \hbar$, were measured by the recoil-distance method. The extracted matrix elements confirm earlier Coulomb excitation results, and indicate that the $K = \frac{11}{2}^-$ γ -vibrational band has a deformation $\sim 40\%$ larger than the ground band.

Contents

List of Tables	ix
List of Figures	x
1 Introduction	1
2 Theory and Models	5
2.1 Microscopic Models of the Nucleus	5
2.1.1 Spherical Shell Model	5
2.1.2 Deformed Shell Model	6
2.2 Collective Rotations and Vibrations	7
2.2.1 Coupling of Single Particle Motion and Rotations	10
2.3 Band Crossings	11
2.3.1 Phenomenological Classification of Rotational Bands	11
3 Experimental Techniques and Equipment	14
3.1 Introduction	14
3.2 GAMMASPHERE	15
3.3 The CHICO Detector	17
3.3.1 Design Requirements	17
3.3.2 CHICO Description	19
3.3.3 PPACs	23
3.3.4 Electronics	27
3.3.5 Position Measurement and Calibration	30
3.3.6 Time Measurement and Particle Identification	35
3.3.7 Performance of GAMMASPHERE with CHICO	37
3.4 Summary	38
4 ^{252}Cf Spontaneous Fission Experiment Description	40
4.1 Introduction	40
4.2 The Experiment	41
4.2.1 The Fission Source	42

4.3	Thick Source Data	43
4.4	Analysis	43
4.4.1	Mass Measurement	44
4.4.2	Gamma-ray Analysis	46
4.5	Gamma-ray Spectrum Analysis	50
4.6	Selectivity	54
4.6.1	Mass Gating	54
4.6.2	Selectivity Provided by the Doppler Correction	55
4.6.3	H-K Measurement	57
4.6.4	Observation of Levels at Higher Spins and Excitation Energy	58
4.7	Summary	62
5	Neutron $h\frac{11}{2}$ band structures in the neutron-rich Pd	63
5.1	Introduction	63
5.2	$^{113,115}\text{Pd}$ Ground Bands	65
5.3	Isomeric bands in $^{113,115}\text{Pd}$	67
5.4	$^{112,114,116}\text{Pd}$	71
5.5	$^{111,113}\text{Rh}$	72
5.6	Discussion	75
5.7	Summary	82
6	Lifetime measurement of ^{135}I	83
6.1	Matrix Elements from ^{134}Te	84
6.2	Shell Model prediction of the $\frac{23}{2}^-$ level lifetime in ^{135}I	87
6.3	Measurement of the $\frac{23}{2}^-$ level lifetime in ^{135}I	89
7	High Spin Results	93
7.1	^{112}Ru	93
7.2	$^{102,104,106,108}\text{Mo}$	95
7.3	$^{150,152,154,156}\text{Nd}$	95
7.4	$^{156,158,160}\text{Sm}$	97
7.5	Summary	99
8	Conclusion	101
	Bibliography	104
A	Lifetime Measurement of low-lying levels in ^{165}Ho	114
A.1	Introduction	114
A.1.1	The Coulomb Excitation Experiments	115
A.1.2	Intrinsic Moments of Bands in ^{165}Ho from In-Band Matrix Elements	116
A.1.3	Motivation for the Lifetime Measurement Experiment	117

A.2	The Recoil-Distance Lifetime Experiment	119
A.2.1	Experimental Method	119
A.2.2	Lifetime analysis	120
A.3	Matrix elements derived from the lifetime measurement	122
A.3.1	Ground Band Matrix Elements	126
A.3.2	$K=\frac{11}{2}^-$ In-Band Matrix Elements	126
A.3.3	$K=\frac{11}{2}^-$ Band to Ground Band Matrix Elements	128
A.4	Summary	129
B	Gammasphere Calibration	132
B.1	Energy and Efficiency Calibration	132

List of Tables

3.1	Logic tables programmed into the Programmable Logic Unit (PLU) used to define the first level trigger. The “Forward only” section refers to experiments with inverse kinematics. “Forward and Backward” would be used for experiments with a projectile with less mass than the target. A valid particle signal is given only if one of the conditions is met.	30
3.2	Contributions to the time resolution for 780 MeV ^{162}Dy on a $250\mu\text{g}/\text{cm}^2$ ^{118}Sn target.	37
4.1	Selection criteria for a thin fission source isotope.	43
A.1	Quadrupole moments and deformations of the $K=\frac{7}{2}^-$ ground band and the $K=\frac{11}{2}^-$, $\frac{3}{2}^-$ γ -bands of ^{165}Ho measured by Coulomb excitation. . .	118
A.2	^{165}Ho Ground Band Lifetimes	124
A.3	^{165}Ho $K=\frac{11}{2}$ Band Lifetimes	124

List of Figures

1.1	Nuclei populated in $^{252}\text{Cf}(\text{SF})$ which have been studied spectroscopically.	2
3.1	Schematic view of part of the GAMMASPHERE array (from [24]).	17
3.2	Sectional view of CHICO. The target chamber housing the PPACs and the pressure window is on the right. The transmission lines carrying the signals from the PPACs to the amplifier boards can also be seen. The length of the assembly is 91 cm.	20
3.3	Cross-section view of the CHICO target chamber. The heavy lines show the vacuum envelope containing the gas volume.	21
3.4	One half of CHICO coupled with one half of GAMMASPHERE.	22
3.5	Assembly of an individual PPAC. The asymmetrically segmented anode and the cathode board with the attached Lexan spacer are shown.	24
3.6	Front and back of a cathode board.	25
3.7	Schematic for ideal and current three-layer cathode board delay lines.	26
3.8	Schematic for two-layer cathode board delay lines.	26
3.9	Simulation of the response of the two and three layer cathode-board delay lines.	27
3.10	Schematic of the acquisition and trigger electronics.	29
3.11	Segmentation of Anode Pairs. Co-planar anode pairs (front-front and front-back) are segmented in a way to uniquely define the ϕ of the reaction plane. For example, if the large section of both anodes trigger, then the reaction plane is in ϕ slice 2.	31
3.12	Scattering angle position spectrum. The various features of the position spectrum are discussed in the text of Section 3.3.5.	32
3.13	Calibration of the front counter theta positions. The heavy lines (experimental data) are fit to the calculated angular correlations (light lines) for a given reaction to obtain the θ calibration coefficients for the front counter.	33
3.14	Calibration of the back counter theta positions using the $^{252}\text{Cf}(\text{SF})$ data. The heavy line is the position measurement and the light line is the fit to the data.	34

3.15	Particle identification. Measurement of the time-of-flight difference and scattering angles allows the two scattering solutions to be cleanly separated. The time difference for the two solutions is 6.6 ns at 45° (channel 112)	35
3.16	Measured mass spectrum from the reaction $^{114}\text{Sm} + ^{248}\text{Cm}$ at 888 MeV.	36
3.17	GEANT simulation of the effect of CHICO on the peak efficiency of GAMMASPHERE for γ -rays emitted at the target location.	38
3.18	GEANT simulation of the effect of CHICO on the peak-to-total ratio of GAMMASPHERE for γ -rays emitted at the target location.	39
4.1	Schematic of the fission experiment setup. The PPAC array (CHICO), is shown with two representative GAMMASPHERE Ge detectors and the fission source.	41
4.2	The mass division between the fission partners can be uniquely mapped from the time-of-flight difference of the recoiling nuclei and angular position of the fission axis.	46
4.3	Position spectrum from the $^{252}\text{Cf}(\text{SF})$ experiment. The solid line shows the expected solid-angle dependence of the yield. Above 60° the yield drops due to target effects.	47
4.4	Measured Mass Resolution. The measured mass for individual nuclei are projected by setting double gates on γ ray transitions. The relative intensities of the mass distributions are not to scale.	48
4.5	Effect of heavy/light Doppler correction on raw γ data. This figure shows the results of a simulation of the raw line shape and the line shapes after the complimentary Doppler corrections are applied.	49
4.6	Measured γ -ray energy resolution in the thin source $^{252}\text{Cf}(\text{SF})$ experiment. The effect of detector noise, counting statistics and Doppler broadening are included.	51
4.7	The multiplicity distribution (normalized to the number of triple events) and number of unpacked triples from clean γ rays events from the thin source $^{252}\text{Cf}(\text{SF})$ experiment.	52
4.8	Observation of ^{166}Dy in $^{252}\text{Cf}(\text{SF})$. The top figure shows the ground rotational band of ^{166}Dy . The bottom figure shows the coincident transitions in ^{82}Ge	56
4.9	The top figure shows a gated spectrum from the thin source data. The bottom spectra is with the same applied gates in the thick source data.	57
4.10	Delayed γ ray “isomer” spectrum.	58
4.11	Total energy and multiplicity in $^{252}\text{Cf}(\text{SF})$	59
4.12	γ ray spectra with the ‘light’ applied Doppler correction gated on the total energy and multiplicity regions shown in Figure 4.11. The top figure is from the higher total energy region and the lower figure is from the lower total energy region.	60

4.13	Using a thin source eliminates Doppler-broadened line shape problems and allows observation of levels with shorter lifetimes and high spin. The spectrum on the right [40] is from ^{248}Cm in a KCl crystal and shows the effect Doppler-broadening has for higher lying transitions. .	61
5.1	Spectra double gated on the 189.7 and 265 γ -rays in the thin (upper) and thick (lower) source data	66
5.2	^{113}Pd level diagram	67
5.3	^{115}Pd level diagram	68
5.4	Systematics of $\nu h_{\frac{11}{2}}$ band heads in the odd Pd isotopes.	69
5.5	Identification of ^{113}Pd isomer band. The top spectra (a) is from the light Doppler shifted thin source $^{252}\text{Cf}(\text{SF})$ data. The middle spectra (b) is from an asymmetric cube from the thin source $^{252}\text{Cf}(\text{SF})$ data with the Te coincident transitions projected out. The bottom (c) spectra is from a thick source experiment [10, 41]	70
5.6	The average masses of the Te fission partners calculated from the $2^+ \rightarrow 0^+$ Te transitions in coincidence with the Pd. This was used to identify the mass number of the isomeric Pd bands.	72
5.7	Even Pd band crossings	73
5.8	^{112}Pd level diagram	73
5.9	^{114}Pd level diagram	74
5.10	^{116}Pd level diagram	74
5.11	^{111}Rh level diagram [72]	75
5.12	^{113}Rh level diagram [72]	76
5.13	^{116}Pd single particle routhians for neutrons in an oblate shape.	77
5.14	^{116}Pd single particle routhians for neutrons in an prolate shape.	77
5.15	^{116}Pd single particle routhians for protons in an oblate shape.	78
5.16	^{116}Pd single particle routhians for protons in an prolate shape.	78
5.17	The aligned angular momentum of the ground bands of ^{111}Rh and ^{112}Pd and the $\frac{11}{2}^-$ isomer band in ^{111}Pd [59].	79
5.18	The aligned angular momentum of the ground bands in ^{113}Rh , ^{113}Pd , and ^{114}Pd , and the $\frac{9}{2}^-$ isomer band in ^{113}Pd	80
5.19	The aligned angular momentum of the ground bands of $^{114,115,116}\text{Pd}$ and the $\frac{9}{2}^-$ isomer band in ^{115}Pd	80
6.1	^{134}Te level diagram	85
6.2	^{135}I level diagram	88
6.3	^{135}I spectrum	91
6.4	GEANT calculation of the peak-efficiency away from the center of GAMMASPHERE [81]	91
7.1	Level diagram for ^{112}Ru . New levels added from the present work are shown as thick lines in the level diagram.	94

7.2	The left figure shows the RTR model predictions for the energy levels of the γ -band as a function of the γ shape parameter. The right figure shows the value of the shape parameter γ extracted from the level diagram.	95
7.3	Level diagram for $^{102,104,106,108}\text{Mo}$. New levels observed in the present work are shown as thick lines.	96
7.4	Kinetic and dynamic moments of inertia for the ground bands of $^{102,104,106,108}\text{Mo}$	96
7.5	Kinetic and dynamic moments of inertia for ^{104}Mo ground and even and odd spin sequences of the γ -band.	97
7.6	Level diagrams for the ground bands of $^{150,152,154,156}\text{Nd}$	98
7.7	Kinetic and dynamic moments of inertia for the ground bands of $^{150,152,154,156}\text{Nd}$	98
7.8	Level diagrams for the ground bands of $^{156,158,160}\text{Sm}$	100
7.9	Kinetic and dynamic moments of inertia for the ground bands of $^{156,158,160}\text{Sm}$	100
A.1	Level diagram for ^{165}Ho . The matrix elements connecting the levels shown were measured in the Coulomb excitation experiments [87, 88]. The level energies are given in KeV.	116
A.2	Schematic of the Recoil-Distance Lifetime Experiment	120
A.3	Lifetime of the $\frac{11}{2}$ GSB level measured from the $\frac{11}{2}\text{GSB} \rightarrow \frac{9}{2}\text{GSB}$ transition	122
A.4	Lifetime of the $\frac{11}{2} K=\frac{11}{2}$ level measured from the $\frac{11}{2} K=\frac{11}{2} \rightarrow \frac{9}{2}\text{GSB}$ transition	123
A.5	Lifetime of the $\frac{11}{2} K=\frac{11}{2}^-$ level measured from the $\frac{11}{2} K=\frac{11}{2} \rightarrow \frac{7}{2}\text{GSB}$ transition	123
A.6	Ground Band E2 matrix elements from the Coulomb excitation work and from the Recoil-Distance lifetime measurement.	127
A.7	Ground Band M1 matrix elements from Coulomb excitation work and Recoil-Distance lifetime measurement	127
A.8	E2 matrix elements for $K=\frac{11}{2}$, from $\Delta J=2$ in-band transitions	128
A.9	$K=\frac{11}{2}$ M1 in-band matrix elements	129
A.10	E2 $\Delta J=2$ matrix elements connecting the $K=\frac{11}{2}$ band to the ground band	130
A.11	E2 $\Delta J=1$ matrix elements connecting the $K=\frac{11}{2}$ band to the ground band	130
A.12	M1 matrix elements connecting the $K=\frac{11}{2}$ band to the ground band	131
B.1	Energy Calibration curve for GAMMASPHERE.	133
B.2	Intrinsic γ ray energy resolution for GAMMASPHERE	133
B.3	Relative efficiency curve for GAMMASPHERE.	134
B.4	BGO calibration spectra. The spectrum shown is the sum of all the BGO elements of the GAMMASPHERE array.	134

Chapter 1

Introduction

The study of neutron-rich region of the nuclear landscape is expected to yield new and interesting physics. New features such as modification of the nuclear shell structure and new excitation modes ensuing from the weak binding of the neutrons are expected in the extremely neutron-rich region. These prospects motivate the study of the largely unexplored region of neutron-rich nuclei.

There is a paucity of production mechanisms which populate the very neutron-rich nuclei. The fission products of the actinides provide access towards this mass region that is difficult to access by other experimental techniques. The spontaneous fission (SF) of ^{252}Cf , the process used in this work, populates the mass regions centered around $\sim A = 105$ and $\sim A = 145$ with $Z = 42$ and $Z = 56$, respectively. These nuclei lie on the neutron-rich side of the valley of β stability, and nuclei with up to 12 additional neutrons beyond their heaviest stable isotope are produced with enough yield for spectroscopic study (see Figure 1.1). In addition, the fission products are populated to moderate spins, with rotational bands observed up to spin $20 \hbar$. Various nuclear reaction mechanisms have been used to populate neutron-rich nuclei. Deep inelastic [1, 2] and heavy-ion transfer reactions [3] have been used to create neutron-rich nuclei, but the current sensitivity of the γ -ray detector arrays limits the observation of nuclei to those which are ≤ 4 neutrons beyond the stable isotopes. The rotational bands in the nuclei in the $A \geq 160$ region populated by these reactions also have been observed to spins around $14 \hbar$ to $20 \hbar$. Induced fission and fusion-

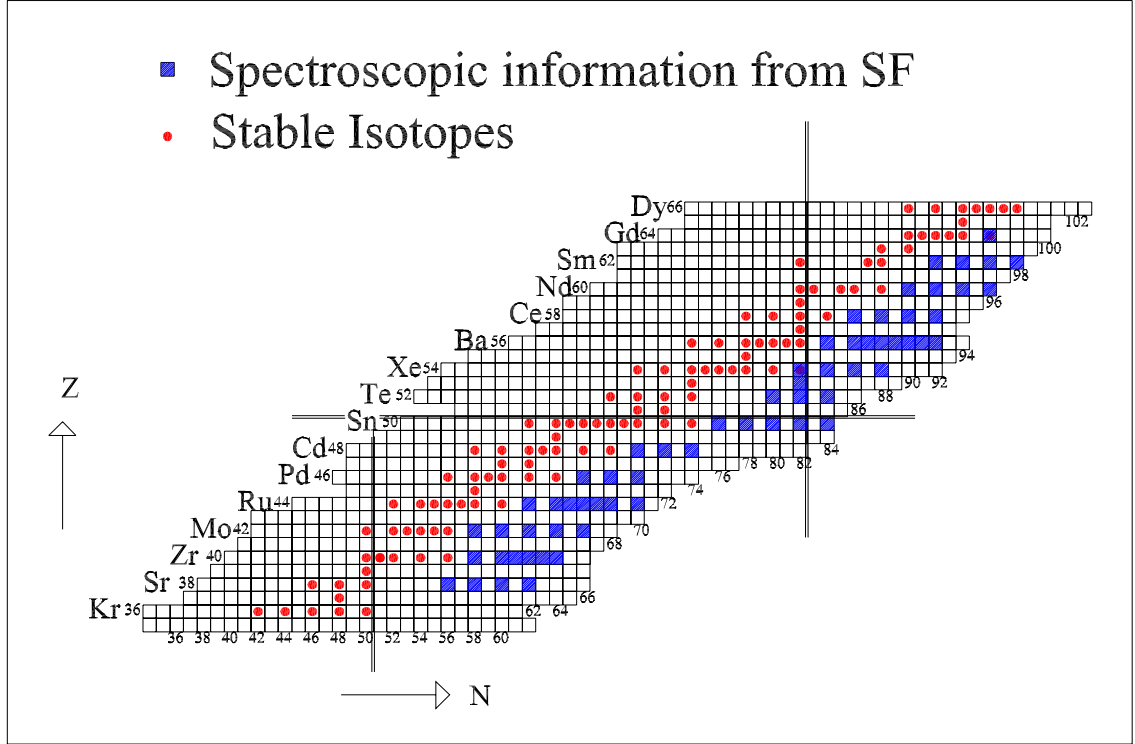


Figure 1.1: Nuclei populated in $^{252}\text{Cf}(\text{SF})$ which have been studied spectroscopically.

fission reactions also can populate neutron-rich nuclei in the same mass region as spontaneous fission, but the additional energy brought into the system results in more neutron emission and, hence, the production of less neutron-rich nuclei. Medium and relativistic energy nuclear fragmentation [4, 5, 6] have been used to create beams of neutron-rich nuclei but, because of the large recoil velocities and low intensities produced, it is currently not possible to perform prompt spectroscopy of high spin states with these beams. The current possibilities for studying neutron-rich nuclei by reaction mechanisms largely do not overlap with the region populated in spontaneous fission.

The neutron-rich nuclei produced in fission have been a rich field of study that has progressed by the development of a variety of experimental techniques and detectors. Because of the numerous nuclei produced in spontaneous fission and, therefore, the large number of γ rays emitted during the de-excitation of these nuclei, the selectiv-

ity provided by these experimental methods are essential in fission product studies. Even the earliest spectroscopic study of $^{252}\text{Cf}(\text{SF})$ suggesting that the spectroscopy of individual fission products was feasible [7] employed the technique of detecting the fission fragments in coincidence with the γ rays. The coincident detection of the fission partners and de-excitation γ -rays along with a measurement of the kinetic energy of the fission partners provided the possibility of assigning the γ -ray peaks to the heavy or light fission partner and provided a mass measurement for the nuclei emitting the γ ray. Another early experiment [8, 9] utilized these methods, in addition to using two γ -ray detectors, to identify the rotational bands of 12 light and 16 heavy fission partners populated with the largest yield. The use of multiple γ -ray detectors allowed the observation of these bands up to spins of $8 \hbar$ and illustrated the utility of γ -ray coincidence techniques in fission product spectroscopy.

The most significant recent advance in the study of these neutron-rich fission products has been the development of high resolution γ -ray detector arrays. The latest generation of these arrays, such as GAMMASPHERE and Euroball, provide high efficiency allowing the collection of high-statistics data sets where three or more γ rays are detected in coincidence for a fission event. The sensitivity imparted by these high efficiency arrays and the selectivity provided by the high-fold collection of γ rays has extended the region of fission products that can be studied and increased the observation of de-excitation cascades to higher spins and excitation energy. In certain cases rotational bands up to spin $20 \hbar$ have been observed with these arrays. Experiments using these arrays have been performed with sources that are thick with respect to the recoiling fission products, that is the fission products are stopped in the source material. The information gathered in these experiments comes primarily from the analysis of the coincidence relationships of the γ rays. These arrays have opened up the spectroscopic study of these otherwise difficult to populate nuclei. Interesting physics that has been produced from these studies include the identification of new regions of quadrupole and octupole deformed nuclear shapes, shape coexistence, and contributed to the study of shell structures around the doubly magic ^{132}Sn region (see, for example, [10] and references therein).

The next suggested experimental advance for the study of fission products is the

coupling of the techniques of coincident fission-product detection with the collection of high-fold γ -ray data. This requires using a thin fission source and large solid-angle fission-fragment detector system compatible with the large γ -ray detector arrays. The benefits of this type of experiment combine the additional selectivity of the mass information and association of the γ rays to either the light or heavy fission partner with the selectivity provided by the γ -ray coincident technique. This type of experiment is expected to allow observation of levels in the neutron-rich nuclei at even higher spin and excitation energy. The possibilities for studying the neutron-rich nuclei produced in the spontaneous fission of ^{252}Cf using high statistics data combining the particle- γ coincident technique and high-fold γ -ray data are explored in this work.

This thesis begins with a description of the theoretical models used in the interpretation of the results of the thin source fission experiment. Next, the “ 4π ” charged-particle detector system, CHICO, is described. The development of CHICO comprises a major component of this thesis. CHICO when used in conjunction with GAMMASPHERE provides a powerful new facility for nuclear spectroscopy. This combination has been used in studies using elastic and quasi-elastic reactions and other binary processes, such as fusion-fission and spontaneous fission, the latter being the focus of this thesis. The present thin source $^{252}\text{Cf}(\text{SF})$ experiment and a discussion of the selectivity provided by coupling a fission-fragment detector with the latest generation of large γ -ray detector arrays then is presented, followed by the results obtained utilizing this new technique.

Chapter 2

Theory and Models

2.1 Microscopic Models of the Nucleus

2.1.1 Spherical Shell Model

The observance of special properties in nuclei with “magic” number of neutrons or protons, occurring at 2, 8, 20, 56, 82, and 126 [11], suggests that the nucleus has a shell structure analogous to that of the atomic electrons. Experimental evidence for shell closures occurring at these magic numbers include the single-particle separation energies, which are the energy required to remove the least bound nucleon from the nucleus. Nuclei with a magic number of neutrons or protons are more strongly bound and have larger separation energies than their neighbors with additional nucleons.

Unlike the electrons in the shell model of the atom, which are influenced by a strong central force created by the Coulomb potential, the nucleons experience a potential that originates from the interaction with all the other nucleons. This can be described by a mean field, $V(\mathbf{r})$, which is commonly modeled with a Wood-Saxon or harmonic oscillator form. With this type of average potential, the nucleons are treated as being independent of each other. This approach is validated by the long mean free path of the nucleons caused in part by the Pauli Exclusion Principle. The

Hamiltonian for the nucleons in the single-particle shell model is given by

$$H\psi_i(\mathbf{r}) = \left[-\frac{\hbar^2}{2m} \nabla^2 + V(\mathbf{r}) \right] \psi_i(\mathbf{r}) = \epsilon_i \psi_i(\mathbf{r}) \quad (2.1)$$

This description still does not reproduce the observed shell closures at magic numbers of neutrons or protons. A spin-orbit ($\mathbf{L} \cdot \mathbf{S}$) term of the appropriate strength must be included in the potential $V(\mathbf{r})$ for the calculated energy levels to agree with experimental results. The projection of the angular momentum, l_z , and spin, s_z , are no longer good quantum numbers since they do not commute with single-particle Hamiltonian which includes the spin-orbit term. The levels are characterized by the radial quantum number n , the orbital angular momentum quantum number l , the spin quantum number s , the total angular momentum j , and its projection j_z . The terminology of the atomic shell model is frequently used in labeling orbitals with the quantum number $l=0,1,2,3,4,5\dots$ with the letters $s, p, d, f, g, h\dots$. This description assumes that the single particle orbitals are completely independent. The full spherical shell model includes a residual two-body interaction.

The spherical shell model is successful in predicting certain properties of nuclei in regions near closed shells. The spins, parities and transition rates of excited particle-hole and single particle states can be calculated with this model, and ground state spins and parities can also be explained. Nuclei further from the closed-shell regions show compelling evidence for deformed shapes. For these regions, a spherical potential is no longer convenient, and a deformed potential provides a more useful representation.

2.1.2 Deformed Shell Model

In the mid-shell regions there is considerable evidence for stable deformation of the nuclear shape, such as large quadrupole moments of the ground state of nuclei and the presence of rotational bands. These features are not conveniently reproduced with the spherical shell model, and a more effective approach is to assume that the nucleons are effected by a deformed average potential. The model of the nucleus described by a quadrupole-deformed harmonic oscillator potential was considered

first by Nilsson [12].

The dynamics of the nucleons is described by a three-dimensional anisotropic harmonic oscillator with a Hamiltonian

$$H_0 = -\frac{\hbar}{2M} \nabla^2 + \frac{M}{2}(\omega_x^2 x^2 + \omega_y^2 y^2 + \omega_z^2 z^2) \quad (2.2)$$

where the coordinates refer to a body-fixed frame. With the assumption of axial symmetry, the symmetric axis is taken, by convention, to be the z -axis. A deformation parameter, δ , can be introduced giving

$$\omega_{\perp}^2 = \omega_x^2 = \omega_y^2 = \omega_0^2(\delta) \left(1 + \frac{2}{3}\delta\right) \quad (2.3)$$

$$\omega_z^2 = \omega_0^2(\delta) \left(1 - \frac{4}{3}\delta\right) \quad (2.4)$$

and $\omega_0(\delta)$ is defined in a manner as to conserve volume. The eigenstates for the axial symmetric case solved in the cylindrical coordinate system are characterized by the quantum numbers n_z , n_ρ , m_l , where m_l is the projection of the particle angular momentum onto the symmetry axis. The energy of the eigenstates is given by

$$\epsilon_0 = \hbar\omega_0 \left[\left(N + \frac{3}{2}\right) + \delta \left(\frac{N}{3} - n_z\right) \right] \quad (2.5)$$

with $N = n_z + 2n_\rho + |m_l|$. This equation shows that the deformation causes splitting of levels with the same N and different n_z . The quantum numbers characterizing the Nilsson levels are $[Nn_zm_l]\Omega$, where $\Omega = m_l + m_s$ is the projection of the angular momentum onto the symmetry axis.

The full Nilsson Hamiltonian includes a spin-orbit term $\mathbf{L} \cdot \mathbf{S}$ and a \mathbf{L}^2 term to account for deficiencies in the assumption of a harmonic oscillator form of the potential. With the inclusion of these terms, n_z , n_ρ , and m_l are no longer good quantum numbers. For large deformations, however, the contributions of these terms are small compared to the effect of the deformation, and the levels can be characterized by the quantum numbers of the anisotropic harmonic oscillator.

2.2 Collective Rotations and Vibrations

Nuclei exhibit collective behavior that can be modeled neglecting the microscopic structure. The separation of macroscopic collective motion and microscopic single

particle degrees of freedom is justified in the adiabatic limit, where the collective motion is slow compared to the frequency of the single particle motion. The collective motion at low excitation energy largely is related to surface motion and, hence, collective models of the nucleus begin with a description of the nuclear shape.

The nucleus can be modeled as a body having a distinct surface with a radius R defined by

$$R(\theta, \phi) = R_0 \left(1 + \sum_{\lambda=0}^{\infty} \sum_{\mu=-\lambda}^{\lambda} \alpha_{\lambda\mu}^* Y_{\lambda\mu}(\theta, \phi) \right) \quad (2.6)$$

where R_0 is the radius of a sphere with the same volume. For this expansion, the α_{00} term ensures volume conservation and the $\alpha_{1\mu}$ terms fix the center of mass location. The lowest order of interest ($\lambda = 2$) describes a quadrupole deformation. Here the five space-fixed parameters $\alpha_{2\mu}$ can be reduced by an appropriate rotation to two real parameters, a_{20} and a_{22} , describing the nuclear shape in the intrinsic frame, and 3 Euler angles describing the orientation of the nucleus. A quadrupole deformed nuclear shape can be represented in the body-fixed frame using the Hill-Wheeler coordinates [13], β and γ , defined by

$$a_{20} \equiv \beta \cos(\gamma) \quad (2.7)$$

$$a_{22} \equiv \frac{1}{\sqrt{2}} \beta \sin(\gamma) \quad (2.8)$$

$$\beta^2 \equiv a_{20}^2 + 2a_{22}^2 \quad (2.9)$$

where β describes the magnitude of the quadrupole deformation and γ , in the region $0^\circ \leq \gamma < 60^\circ$, describes the amount of asymmetry with respect to the principle axis.

In its intrinsic frame, the collective motion of the nucleus can be described by the collective Hamiltonian [14]

$$H_c = V(\beta, \gamma) + \frac{1}{2} \sum_i \mathcal{J}_i(\beta, \gamma) \omega_i^2 + \frac{1}{2} B_{\beta\beta} \dot{\beta}^2 + B_{\beta\gamma} \dot{\beta} \dot{\gamma} + \frac{1}{2} B_{\gamma\gamma} \dot{\gamma}^2 \quad (2.10)$$

where \mathcal{J}_i are the moments of inertia, ω_i are the angular velocities, and $B_{\beta\beta}$, $B_{\beta\gamma}$, $B_{\gamma\gamma}$ are the mass parameters for the β , $\beta - \gamma$ coupled, and γ vibrations, respectively.

The wave function in the space-fixed coordinate system for a nucleus described by

the Bohr Hamiltonian can be separated into intrinsic and rotational components by

$$\Psi_{\alpha M}^I = \sum_K \phi_{\alpha IK}(\beta, \gamma) |IKM\rangle \quad (2.11)$$

where $\phi_{\alpha IK}$ are the solutions to the Bohr Hamiltonian with angular momentum I , with projection K onto the symmetry axis, and α are all the other quantum numbers of the intrinsic motion. The rotational component is defined by

$$|IKM\rangle = \sqrt{\frac{2I+1}{8\pi^2}} D_{MK}^{I*}(\Omega) \quad (2.12)$$

where $D_{MK}^{I*}(\Omega)$ are the Wigner functions, and Ω represent the Euler angles. The wave function $\Psi_{\alpha M}^I$, has angular momentum I and a projection, M , of the angular momentum onto the z -axis.

The most common collective degrees of freedom for a quadrupole-deformed nucleus are rotation, β -vibration, and γ -vibration. These modes of excitation are common to deformed nuclei and typically have energies less than the pairing gap, and, hence, are important in describing the low-lying spectral features of deformed nuclei. The features can be illustrated by solutions to a simplified expansion of the Bohr Hamiltonian, as in the Rotation-Vibration model [15], that assumes axial symmetry ($\gamma=0^\circ$) and neglects terms which explicitly couple the rotational, β - and γ -vibrational degrees of freedom. In this case K remains a good quantum number and the sum in equation 2.11 reduces to a single term. Also, the intrinsic part of the wave function $\phi_{\alpha K}^I$ separates in β and γ and the wave function in the space-fixed frame can be written as

$$\Psi_{\alpha MK}^I = |n_\beta\rangle |n_\gamma\rangle |IKM\rangle. \quad (2.13)$$

with the energies of the eigenstates given by

$$E_{Kn_\beta n_\gamma} = \hbar\omega_\beta \left(n_\beta + \frac{1}{2}\right) + \hbar\omega_\gamma \left(2n_\gamma + 1 + \frac{|K|}{2}\right) + \frac{\hbar^2}{2\mathcal{J}}(I(I+1) - K^2) \quad (2.14)$$

The level diagram suggested by equation 2.14 illustrates some general features of the spectra of deformed nuclei. States of different intrinsic structure, here described

by different number of vibrational quanta, n_β and n_γ , can be the basis of rotational bands with level spacing described by the $I(I+1)$ relation. In general other types of intrinsic states also can be the basis for rotational bands, such as single-particle and particle-hole states.

2.2.1 Coupling of Single Particle Motion and Rotations

In a simple macroscopic picture, the nucleus is treated as a rigid body subject to vibrational and rotational motion. A realistic microscopic model necessarily needs to include the effect a rotating nuclear potential has on the single particle orbitals. For example, the low-lying levels of rotational bands deviate from the predicted $I(I+1)$ level spacing. This can be understood as a reduction of the pairing energy and partial alignment of the angular momentum by the Coriolis interaction of nucleon pairs coupled to zero angular momentum. These effects cause a gradual increase in the moment of inertia as the rotational frequency increases and, hence, the observed deviation from the $I(I+1)$ spacing. At higher rotational frequencies the Coriolis force is strong enough to overcome the pairing energy and align the angular momentum of the nucleons along the rotational axis.

One method of taking into account the effect of rotation on single particle motion is the cranking model proposed by Inglis [16]. In this model the single-particle potential of the fixed nuclear shape of the form $V(\mathbf{r}, \mathbf{t}) = V(r, \theta, \phi - \omega t, t = 0)$ is rotated about a space-fixed axis. The explicit time dependence of the space-fixed Hamiltonian is removed by a unitary transformation $U = e^{i\omega \mathbf{J}_x t}$ into the body-fixed frame. The single-particle Hamiltonian, h_ω , in the body-fixed frame then is related to the Hamiltonian in the space-fixed frame, $h(t)$, by

$$h_\omega \tilde{\Psi} = (h(0) - \omega \mathbf{J}_x) \tilde{\Psi} \quad (2.15)$$

with $h(0) = U h(t) U^{-1}$ and $\tilde{\Psi} = U \Psi$, and the energies (ϵ_i) of the single-particle orbitals in the body-fixed frame are related to the energies ($\tilde{\epsilon}_i$) in the space-fixed frame by

$$\epsilon_i = \tilde{\epsilon}_i + \omega \langle \tilde{\Psi} | J_x | \tilde{\Psi} \rangle. \quad (2.16)$$

The rotation has the largest effect on orbitals having large j , the total angular momentum of the orbital, and small Ω , the projection of the single-particle angular momentum on the nuclear symmetry axis, values. The excitation energy of these levels are reduced in energy with increasing ω as they are aligned along the rotational axis.

2.3 Band Crossings

In deformed nuclei, excited rotational bands are built on microscopic structures different than the ground state configuration and therefore can have moments of inertia that differ from the ground band. The energy levels of the rotational bands follow the approximate relation $E(I) = E(0) + \frac{\hbar^2}{2\mathcal{J}}I(I+1)$, where $E(0)$ is the band head energy. Bands with larger moments of inertia eventually will cross bands with lower moments of inertia in the I versus E plane. This means that, at the crossing point, members of the crossing bands with the same spin will have approximately the same energy. The residual interaction repels the states at the band crossing and causes band mixing near the crossing point. The de-excitation proceeds along the yrast line, which is the sequence of spins with lowest energy for a given spin.

The de-excitation cascade of γ rays reflect the change of the structure of the nucleus at the crossing point. For weak interactions between the crossing bands, the properties of the observed rotational sequences can change dramatically over a small range of spin. This change can be demonstrated by plotting the moment of inertia against the rotational frequency. The increase in moment of inertia at the band crossing corresponds to a decrease in rotational frequency of the nucleus, and for weak interactions between the bands the moment of inertia has a characteristic “s” shape.

2.3.1 Phenomenological Classification of Rotational Bands

The low spin energy levels of rotational bands in deformed nuclei can be described to first order by the rigid rotor result

$$E = \frac{1}{2}\mathcal{J}\omega^2 = \frac{\mathbf{L}^2}{2\mathcal{J}}, \text{ with } \mathbf{L}^2 = \hbar^2 I(I+1) \quad (2.17)$$

The moment of inertia (\mathcal{J}) and frequency of rotation (ω) for a rotational band can be defined from the level energies in analogy with classical relations. The kinetic ($\mathcal{J}^{(1)}$) and dynamic ($\mathcal{J}^{(2)}$) moments of inertia are defined (Ref. [17], for example) as

$$\mathcal{J}^{(1)} = \frac{1}{2} \left(\frac{dE(I)}{d(I^2)} \right)^{-1} = \frac{(2I-1)\hbar^2}{E_\gamma} \quad (2.18)$$

$$\mathcal{J}^{(2)} = \left[\frac{d^2 E(I)}{(dI)^2} \right] = \frac{4\hbar^2}{\Delta E_\gamma} \quad (2.19)$$

for $I \rightarrow I-2$ transitions, with $E_\gamma = E(I) - E(I-2)$, where the differential quantities are approximated by discrete differences. The rotational frequency of the nuclei can be defined by [18]

$$\omega = \frac{\sqrt{I^2 - K^2}}{\mathcal{J}^{(1)}} = \sqrt{I^2 - I + 1 - K^2} \frac{E_\gamma}{(2I-1)\hbar} \quad (2.20)$$

The component of the angular momentum, K , directed along the symmetry axis is subtracted from the total angular momentum in the calculation of the rotational frequency, ω , since it does not contribute to the collective rotation perpendicular to the symmetry axis of the nuclear core. Plots of the rotational frequency, ω , versus the moments of inertia, $\mathcal{J}^{(1)}$ and $\mathcal{J}^{(2)}$, are very sensitive to deviations in the rotational sequence of levels.

The aligned angular momentum, $i_x(\omega)$, which is the amount of angular momentum perpendicular to the symmetry axis of the deformed nucleus beyond the contribution of the rotating core, also can be calculated from the level energies. The moment of inertia of the ground band can be expanded as a function of the rotational frequency ω as

$$\mathcal{J}_g = \mathcal{J}_0^{(1)} + \mathcal{J}_1^{(1)} \omega^2 \quad (2.21)$$

where $\mathcal{J}_0^{(1)}$ and $\mathcal{J}_1^{(1)}$ are obtained from a fit to the data, and are called the Harris parameters [19]. The contribution to the angular momentum of the rotating nuclear core is then

$$\hbar I_{ref}(\omega) = (\mathcal{J}_0^{(1)} + \mathcal{J}_1^{(1)} \omega^2) \omega \quad (2.22)$$

and the aligned angular momentum is given by

$$i_x(\omega) = I(\omega) - I_{ref}(\omega) \quad (2.23)$$

The aligned angular momentum, i_x , is useful for interpreting the behavior of the moment of inertia, $\mathcal{J}^{(1)}$.

Chapter 3

Experimental Techniques and Equipment

3.1 Introduction

Recent developments of large γ -ray detector arrays, such as GAMMASPHERE [20], have led to new advances in nuclear physics. The large gains in both the γ -ray detection efficiency and the resolving power achieved with these arrays has enabled the discovery and study of a variety of new physics (see, for example, [23, 24]).

The coupling of these γ -ray detector arrays with auxiliary detectors further expands their versatility. For example, the coincident detection of de-excitation γ rays with the detection of the scattered and recoiling nuclei from heavy-ion reactions performed using thin targets is a powerful method for studying the nucleus. Gamma ray spectra from thick target experiments can suffer from Doppler-broadened line shapes, occurring for transitions which have lifetimes comparable to the stopping time of the nuclei in the target. In thin target experiments the nuclei recoil into vacuum and the Doppler-broadened line shapes can be eliminated. Since the velocities of the nuclei are appreciable, on the order of 5% of the speed of light, the γ rays emitted from the nuclei in flight have associated Doppler shifts. By measuring the time-of-flight difference along with the scattering angles of the nuclei it is possible to reconstruct the kinematics of the reaction and to distinguish the target-like from the projectile-like

nuclei for two body reactions. Measurement of the scattering angles and velocities of the reaction products allows the γ -ray energies to be corrected for the Doppler effect on an event-by-event basis, resulting in spectra with sharp γ -ray peaks and the ability to assign the γ rays to the target-like or projectile like nucleus.

The particle- γ -ray coincidence technique has applications to the study of Coulomb excitation, nucleon transfer, and fission. With large solid angle particle detectors it is possible to concurrently measure scattering angles and γ -ray yields over a range of scattering angles. For Coulomb excitation experiments this is equivalent to measuring γ -ray yields for varying Coulomb excitation strength, giving information on the $B(E\lambda)$ values of the excited levels [21]. The scattering angle information also can be used to select reactions that occur near the grazing angle, selectively enhancing the transfer channels [22]. The coincident γ rays can be used to identify the correlated reaction products determining the number of nucleons transferred. The application of the particle- γ -ray coincidence technique to the study of neutron-rich nuclei resulting from spontaneous fission is discussed in detail in Chapter 4.

To fully utilize the particle- γ -ray coincidence technique with the new powerful γ -ray detector arrays, a large solid-angle particle detector, CHICO (Compact Hheavy Ion Counter), was developed at the University of Rochester as part of this thesis. This chapter describes the equipment used in these types of thin target experiments with a particle detector coupled to a large γ -ray detector array. A brief description of GAMMASPHERE is given, and a more extensive discussion of the design considerations, physical description, and performance of the CHICO detector also is presented.

3.2 GAMMASPHERE

GAMMASPHERE is a spherical array of 110 large volume (7.1 cm diameter x 8 cm length) high-purity Ge γ -ray detectors. The Ge detectors are mounted on two movable hemispheres, allowing access to the reaction region at the center of the array. A schematic diagram of part of the GAMMASPHERE array is shown in Figure 3.1. The distance from the center of the array to the Ge detector faces is 25

cm, constraining the size of any auxiliary detectors.

The factors contributing to the power of GAMMASPHERE are the gains achieved from the high granularity, Compton suppression, and large solid-angle coverage of the array, and the performance of the individual detectors. The key features of the individual detectors are their efficiency, energy resolution, and peak-to-total ratio. Each of the detectors is made of n-type Ge crystal with about a 20% detection efficiency for a γ ray entering the Ge crystal, and 2.5 keV energy resolution for a 1.33 MeV γ ray. The Ge crystals are surrounded by BGO (bismuth germanate) Compton suppressors which allow rejection of events where the full energy of the γ ray is not deposited in the Ge crystal due to Compton scattering. The peak-to-total ratio, the number of counts in the γ -ray peak divided by the total counts in the spectrum, is improved by the Compton suppression from 0.25 to 0.6 for a 1.33 MeV γ ray [23].

The peak efficiency, the probability of detecting the full energy of a γ ray in one of the detectors of the array, depends on the solid angle covered by the Ge detectors. The solid angle coverage by Ge of the array, with the full complement of 110 Ge detectors, is about 47% of 4π sr, resulting in a total peak efficiency of 9.9% for the detection of a 1.33 MeV γ ray by the whole GAMMASPHERE array. The individual detectors subtend an angle of about 15° viewed from the target location at the center of the array. The small solid angle of each detector reduces summing errors, where two γ rays hit the same detector, and reduces Doppler broadening of the γ -ray line shapes.

The high peak efficiency of GAMMASPHERE allows the collection of high-statistics high-fold γ -ray data, where many γ rays are detected in coincidence. The high-fold events can be “unpacked” to increase the statistics for events with lower fold, for example a 5-fold event contains 10 distinct 3-fold events. Multiple gates on γ -ray transitions can be set on high-fold events, allowing specific features of complex γ -ray spectra to be selected and enhanced.



Figure 3.1: Schematic view of part of the GAMMASPHERE array (from [24]).

3.3 The CHICO Detector

3.3.1 Design Requirements

There are several factors constraining the design of a heavy-ion detector to be used successfully in conjunction with GAMMASPHERE. The detector design and performance obviously should address the experimental requirements for the physics being studied. Furthermore, coupling of the heavy-ion detector with GAMMASPHERE constrains the physical size and symmetry of the detector, and requires that the detector is designed to have a minimal impact on the performance of GAMMASPHERE.

The primary purpose of the heavy-ion detector is to gather enough information from the involved nuclei to reconstruct the kinematics of the event. For beam experiments, the measurement of the scattering angles of both target-like and projectile-like nuclei define the momenta of the nuclei through the relation derived from conservation

of momentum, with the assumption of two-body kinematics:

$$P_{1,2} = \frac{P_0 \sin(\theta_{2,1})}{\sin(\theta_1 + \theta_2)} \quad (3.1)$$

where P_0 is the momentum of the beam, P_1 and P_2 are the momentum of the nuclei, and θ_1 and θ_2 are the scattering angles. Resolution of polar scattering angles to 1° is more than sufficient to calculate the momenta of the nuclei since other effects, such as the size of the beam spot, produce comparable errors in the angle measurement.

The scattering angles of the nuclei completely define the momenta for two-body reactions but, in practice, do not uniquely identify the target-like and projectile-like nuclei over the full range of scattering angles. The two scattering solutions can be resolved with inclusion of a measurement of the difference in time-of-flight of the nuclei from the target to the particle detectors. For the geometry of the CHICO detector, the minimum flight path from the target to the detectors is about 13 cm, and for experiments run near the Coulomb barrier the separation in time-of-flight difference for the two solutions is typically on the order of nanoseconds. Therefore to resolve the two solutions over all scattering angles it is critical to use detectors with sub-nanosecond time resolution.

Parallel plate avalanche counters (PPACs) [25] are ideally suited for a detector of this type. They can be designed with sufficient angular resolution and typically have time resolutions around 300 ps (FWHM). PPACs have other attractive features for this application. The individual detectors can handle particle detection rates around 100k/sec, leaving experimental detection rates limited only by the acquisition electronics. The PPACs are resistant to radiation damage, can run for months with good stability, and the detection threshold for heavy ions can be adjusted to the experiment. This last feature is especially important for ^{252}Cf fission studies since the α -decay rate is about 31 times the fission rate it is important to tune the PPACs to be insensitive to the α particles. The PPACs also have a relatively simple light-mass design and are constructed of low Z materials so they do not strongly scatter γ rays, and hence do not degrade the performance of GAMMASPHERE.

The symmetry chosen for the particle detector is dependent on the symmetry of GAMMASPHERE. For certain experimentally measurable quantities, such as the

excitation of the nuclei as a function of the scattering angle (or equivalently the impact parameter), or γ -ray angular distributions, it is useful to sum spectra that originate from sets of γ -ray detectors with similar angular position with respect to particle scattering angles. To maximize the number of spectra that can be summed, minimizing the total number of spectra to analyze, the particle detector should have the same symmetry as the Ge detectors of GAMMASPHERE. The γ -ray detectors of GAMMASPHERE are arranged with pentagonal symmetry, but since the particle detector needs to have an even number of detectors to effectively collect binary particle coincidences, CHICO was designed with the least common multiple of 10 azimuthal sections.

3.3.2 CHICO Description

The CHICO detector consists of 20 separate trapezoidal parallel plate avalanche counters (PPACs). There are two essentially identical assemblies, each of which houses 10 of the PPACs arranged in a truncated cone coaxial with the beam direction (Figures 3.2, 3.3). Figure 3.4 shows the half of the CHICO detector installed in one half of GAMMASPHERE. The PPACs, their segmented anodes, and their delay line cathodes are described in Section 3.3.3. The two assemblies are joined along the $\theta = 90^\circ$ plane (with respect to the beam direction). The forward assembly has an active θ range from 12° to 85° , and the back assembly has an active θ range from 95° to 168° . An individual PPAC covers an azimuthal width of 28° , and there is a dead region of 8° in ϕ between each of the PPACs, giving 280° of ϕ coverage for both the forward and back assemblies. The total angular coverage is $\sim 2.8\pi$ sr, or about 69% of the total solid angle. About 20% of the total solid-angle is lost to the dead space between the PPACs, another 9% is lost along the joint between the two halves, and 2% is lost at the beam entrance and exit ports. The PPACs are positioned with the normal at an angle of 49° with respect to the beam axis and the minimum flight path, from the center of the target to the midpoint between the anode and cathode in the PPACs, is 12.8 cm.

The housing for the PPACs is a 1.58 mm (0.0625 in) thick aluminum hemisphere

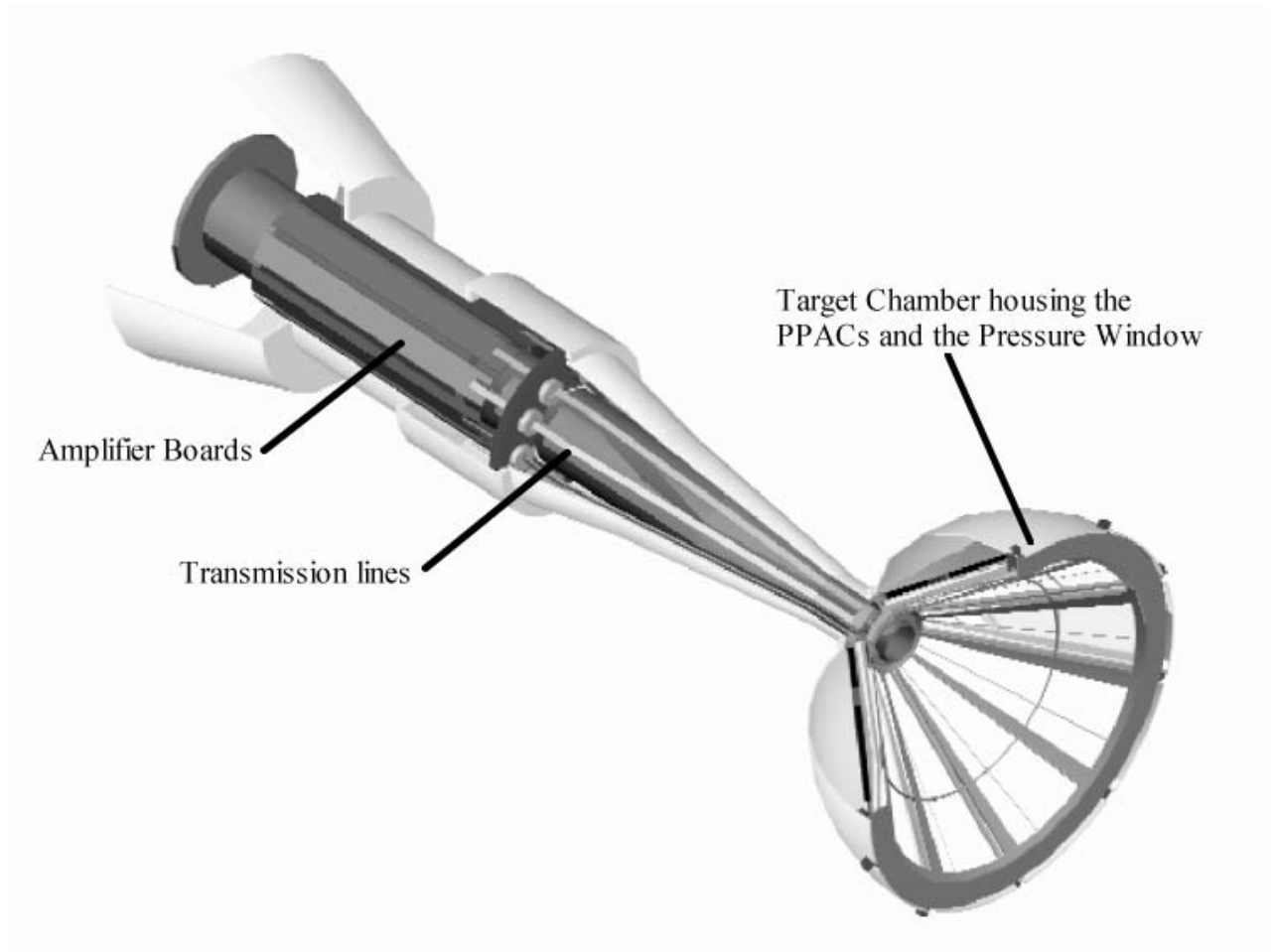


Figure 3.2: Sectional view of CHICO. The target chamber housing the PPACs and the pressure window is on the right. The transmission lines carrying the signals from the PPACs to the amplifier boards can also be seen. The length of the assembly is 91 cm.

shell with a 35.6 cm (14 in) diameter. The PPACs are mounted to fixtures epoxied to the inside of the hemisphere. The epoxy used was Hysol EA 9309.3NA, manufactured by Dexter Aerospace Materials Division, and was chosen for its high shear and peel strength with aluminum. The wide end of the PPACs are seated in a ring glued along the diameter of the hemisphere which also provides the O-ring seal with the pressure window. The pressure window consists of a conical frame covered with $0.9\text{ }\mu\text{m}$ thick Mylar ($120\mu\text{g}/\text{cm}^2$), and serves to contain the detector gas from the target chamber volume. All 10 PPACs for each half of the detector sit in a common gas volume. A

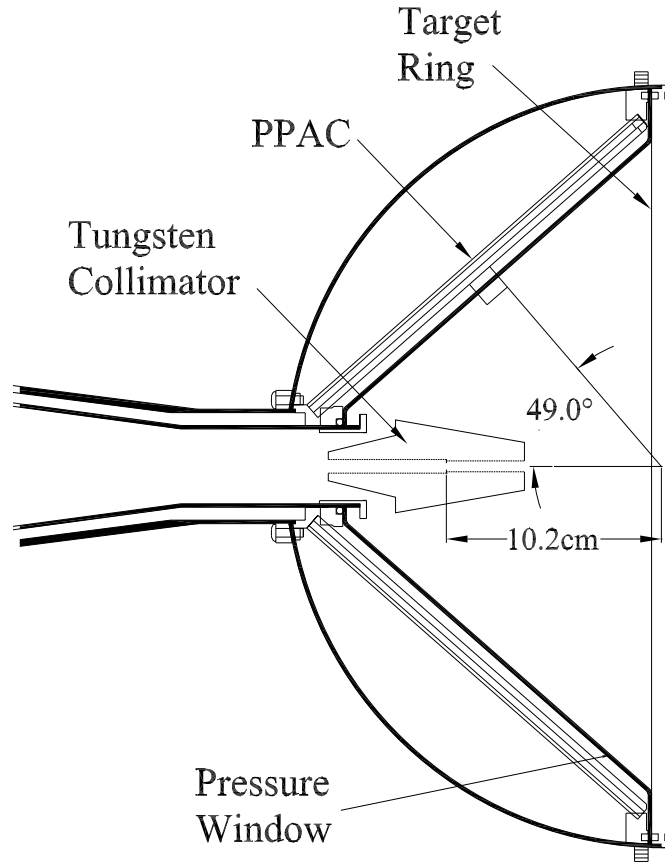


Figure 3.3: Cross-section view of the CHICO target chamber. The heavy lines show the vacuum envelope containing the gas volume.

collimator can also be mounted in the target chamber. The tungsten collimator has a 6.4 mm (0.25 in) diameter entrance hole and a 5.1 mm (0.2 in) exit hole and holds a gold foil with a 3.2 mm (0.125 in) diameter hole 10.2 cm (4 in) from the target. The collimator has no more than 12% transmission for a 600 keV γ ray which may arise from excitation of the gold foil by the beam.

The target ladder can hold four targets at one time and is designed so the targets can be switched without opening the detector. The ladder is mounted on a 9.5 mm (0.375 in) thick ring that has the same diameter as the hemisphere, with an O-ring on each side. This thin ring of the target ladder assembly completes the vacuum

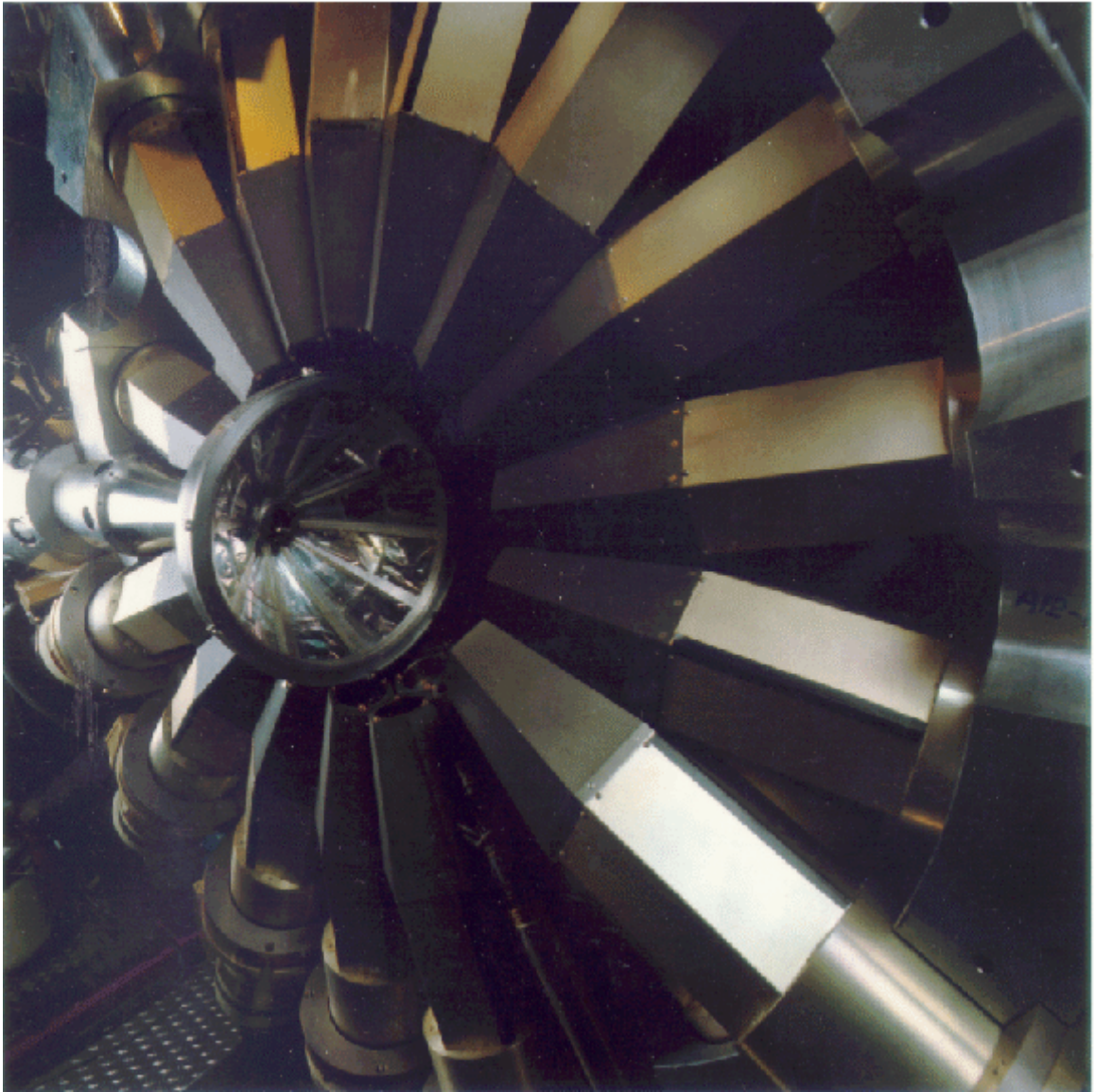


Figure 3.4: One half of CHICO coupled with one half of GAMMASPHERE.

seal between the two halves of the CHICO detector. Two separate target ladder assemblies have been constructed, one of which allows the targets to be retracted into a box to facilitate handling of radio-active targets. Both target ladders are insulated so a bias voltage up to ~ 5 kV can be applied to suppress the emission of secondary electrons.

3.3.3 PPACs

The essential elements of each PPAC comprise a thin film anode plus a cathode circuit board. A diagram of an individual PPAC assembly is shown in Figure 3.5. The anode, made of approximately $100 \mu\text{g}/\text{cm}^2$ thick stretched polypropylene with an approximately $20 \mu\text{g}/\text{cm}^2$ aluminum coating, is segmented into two electrically isolated sections and is glued to a 3.2 mm (0.125 in) thick G10 frame. The signals from the anode and cathode are carried to the amplifiers by a strip-line transmission line which has four 50 ohm impedance traces on a central plane shielded on either side by ground planes. The PPAC end of the transmission line is forked allowing two of the traces to connect to the cathode board and two of the traces to the segmented anode. The anode traces on the transmission line also carry the bias voltage (~ 400 V) to the PPAC anode.

A 3.2 mm (0.125 in) thick Lexan spacer separates the anode from the cathode. The spacer is slotted along the sides so the detector gas can circulate to the active region of the PPAC, preventing degradation of the detector performance over time due to radiation damage of the gas. The azimuthal width of the spacer is 28° , and 30° for the anode frame. The spacer has a smaller opening angle to prevent edge effects, where the aluminized polypropylene is glued to the anode frame, from causing an electrical discharge to the cathode. The azimuthal width of the active area of the PPACs (defined by the spacer) is constant, so the total geometric ϕ acceptance remains constant at 78% over the entire polar range of the full detector assembly.

The cathode board is a three layer circuit board, shown in Figure 3.6. The active side (front) of the cathode board, where the particles are detected, is segmented into 1° wide traces of constant polar angle θ . Each of the traces is connected to one tap of a delay line which is mounted on the back side of the cathode board. The delay line has a delay of 1 ns per tap and is made of passive delay chips manufactured by Rhombus Industries. The traces on the active side of the board are connected to the delay line on the back of the cathode board by plated-thru holes which are located near the edge of the board. The third (middle) layer is a ground plane located between the delay line side and the active side of the cathode. The ground plane acts

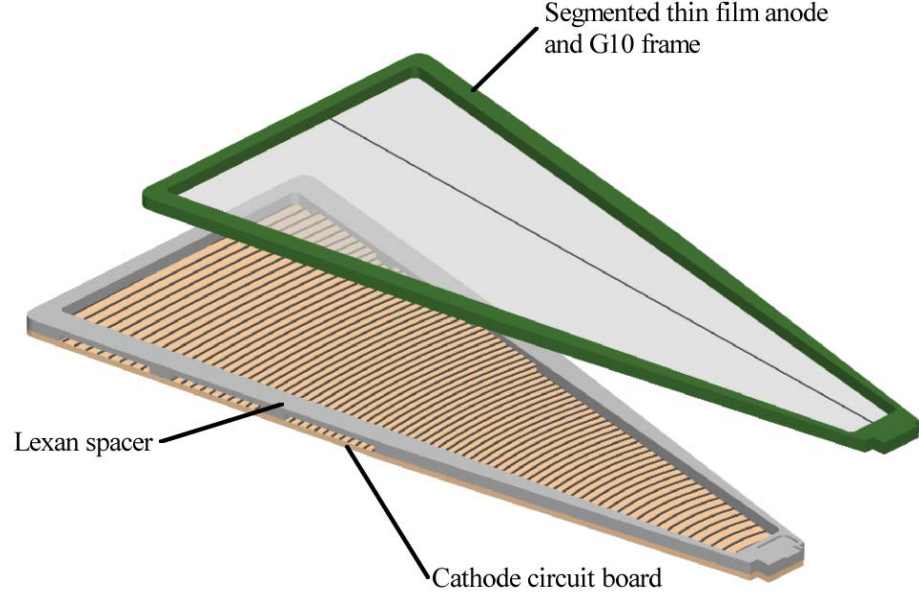


Figure 3.5: Assembly of an individual PPAC. The asymmetrically segmented anode and the cathode board with the attached Lexan spacer are shown.

to capacitively decouple the traces of the delay line on one side of the board from the sensing traces on the active side of the board. The addition of the ground plane considerably improves the performance of the delay line.

The delay line can be modeled with inductors and capacitors as shown in Figure 3.7. An ideal delay line, without any capacitive contribution from the cathode board, would have the values specified by the delay chips, which are $L1=50$ nH for the inductors and $C1=20$ pF for the capacitors, giving a delay of $t_{delay} = \sqrt{LC}=1$ ns per tap. The three-layer board can be modeled by the addition of the capacitance between the traces and the ground plane, calculated to be about 3 pF at each tap. These capacitances are in parallel with the delay line capacitances, changing the value of $C1$ to about 23 pF, and increasing the delay per tap to ~ 1.07 ns. The cathode boards from the previous generation of Rochester heavy-ion detectors [26, 27] were of a similar design, except they did not have a ground plane separating the delay line

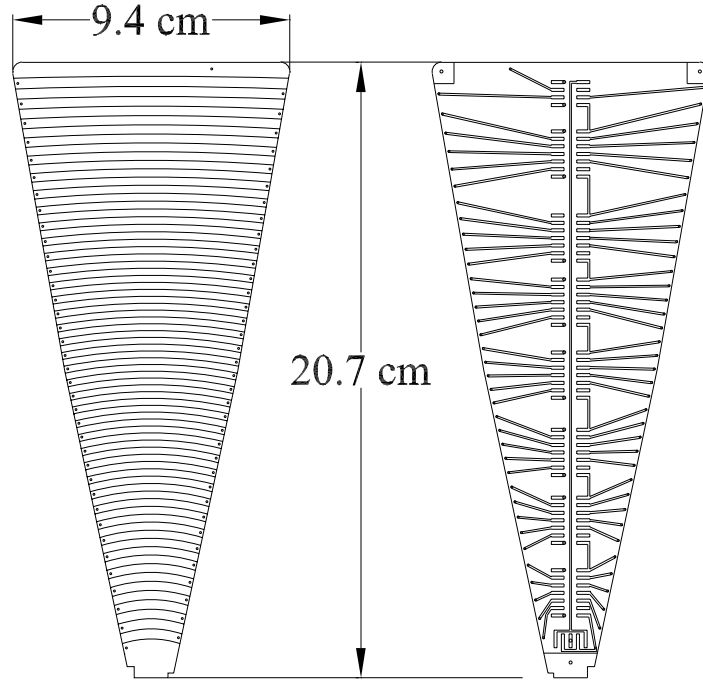


Figure 3.6: Front and back of a cathode board.

from the sensing traces. Since these older cathode boards have no ground plane, there is no additional capacitance between the traces and ground ($C_1=20$ pf). However, the traces connecting the plated-thru holes along the edge of the board to the delay chips capacitively couple, with a capacitance calculated to be 1 pF, to several of the nearest taps of the delay line via the sensing traces on the active side of the board. This old design of cathode boards can be modeled as shown in Figure 3.8.

The performance of these various configurations were simulated using the program SPICE [28]. The simulation modeled the application of a voltage impulse approximating an actual signal (a Gaussian shape with a FWHM of 2 ns) at one end of the delay line and calculated the pulse shape after propagating to the other end of the delay line. The results are shown in Figure 3.9. The only significant difference between the signals propagated down the ideal delay line and the three layer board delay line (not shown) is a small difference in overall delay caused by the additional

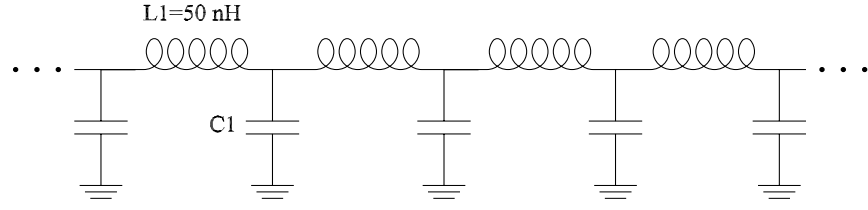


Figure 3.7: Schematic for ideal and current three-layer cathode board delay lines.

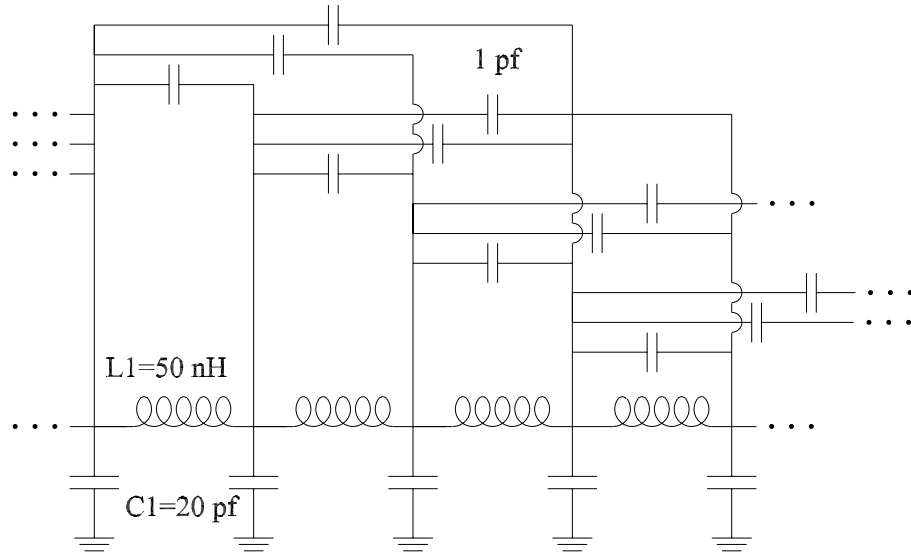


Figure 3.8: Schematic for two-layer cathode board delay lines.

capacitance present at each tap of the delay line for the three layer board. The difference between the two and three layer boards is more significant. The addition of the ground plane increases the output pulse height and decreases the output pulse rise time. This results in a better signal to noise ratio and a better time resolution for the cathode signals and, hence, a more accurate position measurement.

Simulated Response of 3-layer Cathode Board

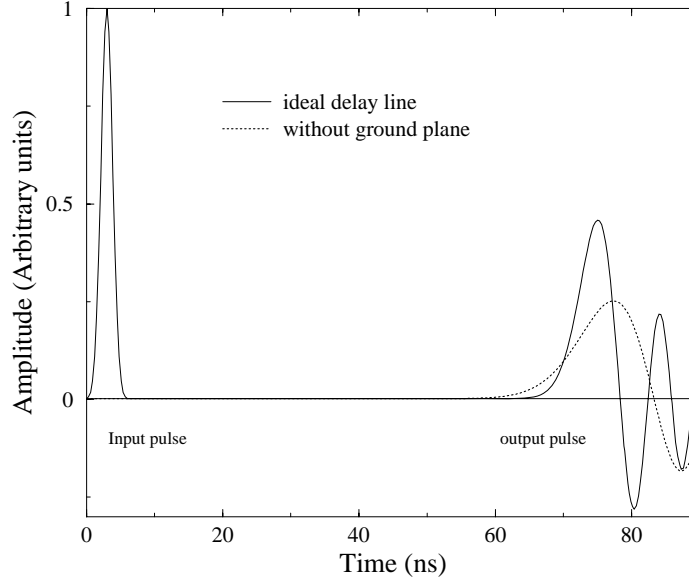


Figure 3.9: Simulation of the response of the two and three layer cathode-board delay lines.

3.3.4 Electronics

Amplifiers

Compact amplifier boards [29] were designed at the Nuclear Structure Research Laboratory specifically for use with the CHICO detector. Each PPAC has a dedicated amplifier board with two anode channels and two cathode channels. The physical size of the boards was kept small, 26.7 cm by 3.2 cm, allowing them to be housed in the detector assembly as close to the detectors as possible to reduce electronic noise pickup. The amplifiers are based on cascable microwave amplification chips, simplifying the design and construction. The circuit boards are three-layer boards, with the signal traces on the middle layer shielded by the ground planes. Since the acquisition electronics require negative inputs with pulse heights on the order of a Volt, the anode amplification chain is non-inverting with a total gain of 400, and the cathode amplification chain is inverting with a gain of 700. The 500 MHz bandwidth of the amplifiers ensures that the rise times of the pulses are not degraded during

amplification. Each of the amplifier channels also has an associated energy signal, created by inductive pick-off from the time signals, useful for performing diagnostics on the detectors during an experiment.

Acquisition Electronics

A schematic figure of the acquisition electronics is shown in Figure 3.10. Standard NIM and CAMAC modules are used to extract and digitize the time information from the amplified anode and cathode signals. The time pick-off signals from both the anodes and cathodes are converted to logic pulses by Tennelec Model 454 Constant Fraction Discriminators (CFDs). These units extract timing information from the input pulses by providing a NIM standard logic output pulse when the input signal reaches a fixed fraction of the maximum input pulse height. The logic timing signals then travel through 130 ns of delay cables and are regenerated and converted to ECL standard logic pulses by 3412 LeCroy discriminators. The 3412 discriminators have two outputs, one which passes the signal on to the time-to-digital converters (TDCs), and the other which can be used in conjunction with scalar units to monitor signal rates during an experiment. The TDCs are a combination of the LeCroy 4303 Fast Encoding and Readout TQCs (FERETs) and the LeCroy model 4300B Fast Encoding Readout ADCs (FERAs). The charge outputs from the FERETs are further delayed by 265 ns and fed into the FERAs, where the signals are digitized and stored until read into the data stream. The FERETs are run in a common stop mode. The FERETs are fast modules with little dead time and are gated at the first level trigger rate. The charge outputs are started in the individual channels of the FERETs upon receipt of the timing signal from the 3412 LeCroy discriminators and are stopped at the end of the gate signal. The FERAs also require a gate signal, but since these are relatively slow devices they are gated at the final trigger rate.

The gates for the FERETs are provided by a LeCroy model 4508 Programmable Logic Unit (PLU). This unit provides a flexible method of generating a valid event (or gate) signal and can be programmed to accommodate various experimental conditions. The anode signals of the full PPAC array are summed by quadrant (front

Figure 3.10: Schematic of the acquisition and trigger electronics.

	Front Right	Front Left	Back Right	Back Left
Forward only	1	1	0	0
Forward and Backward	1	1	0	0
	1	0	0	1
	0	1	1	0
	0	0	0	1
Fission	0	0	1	0
	1	0	0	1
	0	1	1	0

Table 3.1: Logic tables programmed into the Programmable Logic Unit (PLU) used to define the first level trigger. The “Forward only” section refers to experiments with inverse kinematics. “Forward and Backward” would be used for experiments with a projectile with less mass than the target. A valid particle signal is given only if one of the conditions is met.

right, front left, back right, back left) after the CFDs, and these summed signals are the inputs to the PLU. The PLU checks if a valid event occurred according to the appropriate tables (see Table 3.1) and provides the first level trigger signal if the conditions are met. The second level trigger is built by requiring a coincidence between the first level trigger and a valid γ -ray event, which is provided by the GAMMASPHERE electronics. The final level trigger is the sum of the second level trigger and a scaled down first level trigger. The scaled down first level trigger represents a fraction of all the particle events, regardless of any γ -ray requirement, and provides a means of normalizing the γ -rays yields to the total cross section of a reaction. This final trigger is used to gate the FERAs and to inform the GAMMASPHERE data acquisition that the event should be read and entered into the data stream.

3.3.5 Position Measurement and Calibration

The detector was designed to measure both the polar (θ) and azimuthal (ϕ) angles (with respect to the beam direction) of the scattered nuclei. The ϕ measurement is

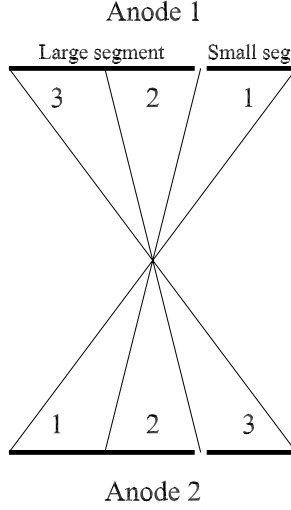


Figure 3.11: Segmentation of Anode Pairs. Co-planar anode pairs (front-front and front-back) are segmented in a way to uniquely define the ϕ of the reaction plane. For example, if the large section of both anodes trigger, then the reaction plane is in ϕ slice 2.

provided by the segmentation of the anodes. A “binary” scheme was implemented, similar to previous generations of Rochester heavy-ion detectors [26, 27], to reduce the number of electronic channels necessary for the given resolution. The anodes are segmented into two sections covering $\frac{1}{3}$ and $\frac{2}{3}$ of the ϕ -angle subtended by the individual PPACs. Two-body kinematics demand that the scattered beam-like and recoiling target-like nuclei are co-planar, so the combination of large and small segment in which the reaction products are detected define the ϕ -slice in which the reaction plane lies (Figure 3.11). The ϕ -resolution is $\sim \pm 4.7^\circ$ and is limited by the angular width of the smaller of the two anode segments, which is 9.3° . The ϕ -measurement is defined by the geometry of the detector and combination of the anodes in which the nuclei are detected.

The θ angle measurement is obtained from the signals read out of the delay line on the cathode board. The signal generated in the cathode by the incident heavy ion travels both directions down the delay line. The time difference between the two ends of the delay line determines the location of the event along the delay line.

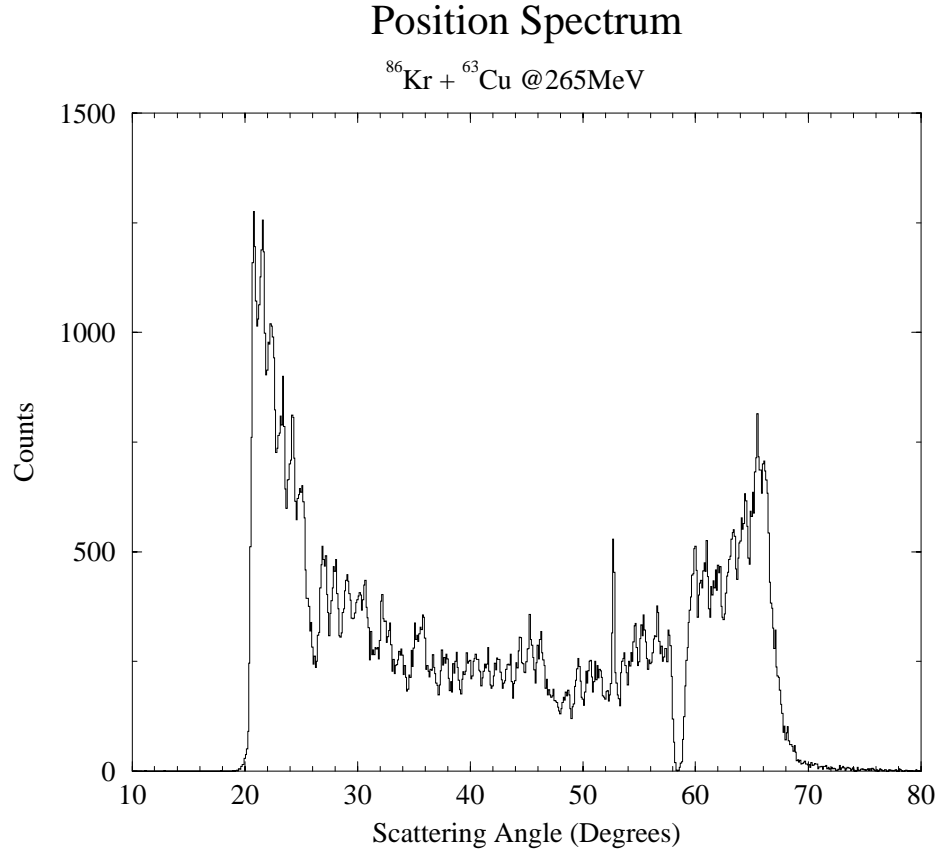


Figure 3.12: Scattering angle position spectrum. The various features of the position spectrum are discussed in the text of Section 3.3.5.

An example of the position measurement is shown in Figure 3.12. This spectrum contains events in which the target and projectile nuclei were detected in coincidence in the reaction ^{86}Kr on ^{63}Cu at a lab energy of 265 MeV. The peaks in the spectra correspond to theta slices of the cathode board indicating that the position resolution is about 1° . The dip in the position spectrum near 60° is the shadow of a support rib in the pressure window, which subtends 1° . The dip in the spectrum at 25° results from the coincidence particle-detection requirement since this is the scattering angle for Kr when the Cu is blocked by the support rib in the opposite PPAC. Also present in the position spectrum is the maximum scattering angle of 47° for the Kr nuclei. The sharp cutoff at 20° is from a mask to eliminate small angle scattering events. The cutoff beyond 67° is also a result of coincidence requirement, reflecting that the

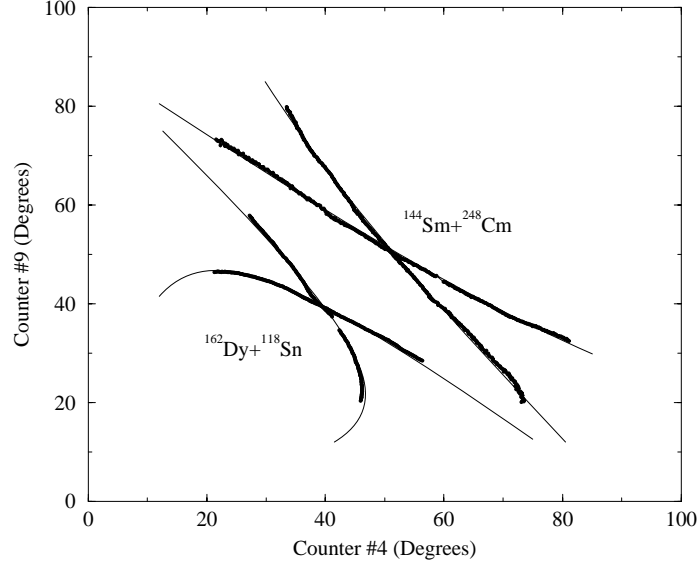


Figure 3.13: Calibration of the front counter theta positions. The heavy lines (experimental data) are fit to the calculated angular correlations (light lines) for a given reaction to obtain the θ calibration coefficients for the front counter.

Kr is masked below 20° .

The position measurement for an individual PPAC can be calibrated using the physical limits and the shadow of the support rib as reference points. A more precise calibration can be performed by relying on the angular correlation of the scattered reaction products in beam experiments. The position measured in one PPAC is plotted against the position measured in the opposing PPAC, and these curves are then fit to the calculated angular correlations. There are two curves in these types of plots corresponding to either the projectile-like or target-like nucleus arriving in one of the PPACs. There is one unique angle where the curves cross, defined in the lab frame by:

$$\theta_{cross} = \cos^{-1} \left(\frac{1}{2} \sqrt{1 + \frac{m_{proj}}{m_{targ}}} \right) \quad (3.2)$$

where m_{proj} and m_{targ} are the mass of the projectile and target, respectively. Matching this point in the data to the calculated value defines a family of possible calibration coefficients. Since the angular correlations can be relatively featureless (as can be seen for the $^{144}\text{Sm} + ^{248}\text{Cm}$ reaction in Figure 3.13), it may not be possible to pick

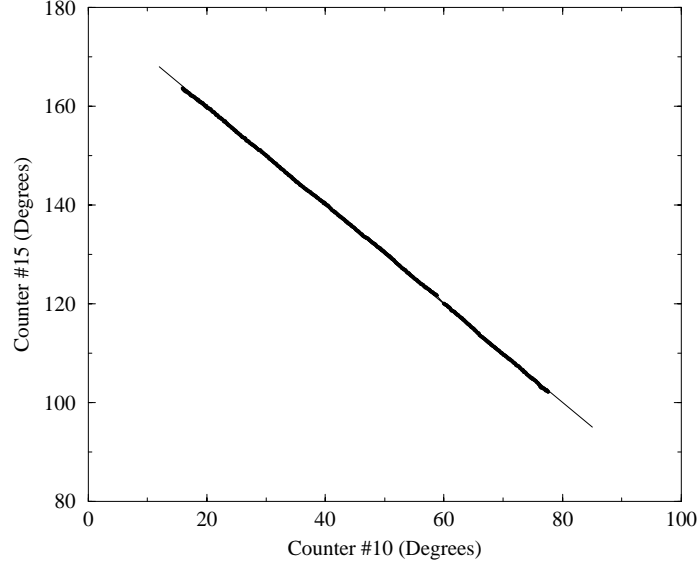


Figure 3.14: Calibration of the back counter theta positions using the $^{252}\text{Cf}(\text{SF})$ data. The heavy line is the position measurement and the light line is the fit to the data.

the calibration coefficients unambiguously. Adding a second data set with m_{proj} and m_{targ} chosen so that θ_{cross} is significantly different provides a method of choosing the correct values for the calibration. For this experiment the position calibration was performed using the reactions $^{144}\text{Sm} + ^{248}\text{Cm}$ and $^{162}\text{Dy} + ^{118}\text{Sn}$. A least-squares fit including both data sets then was performed to extract the calibration for each of the 5 pairs of PPACs in the front array.

The back array of PPACs ($\theta > 90^\circ$) were calibrated in a similar manner, except instead of using beam on target data, the thin source fission data was used. The fission fragments leave the source co-linearly, so the sum of the polar angles of their flight direction must add to 180° . The calibrations for the back PPAC positions can then be fit referenced to the front PPAC positions. An example of this is shown in Figure 3.14. Again, a least-squares fit was performed for each of the 10 front-back pairs of PPACs, but with the coefficients for the front PPACs fixed by the beam on target calibration.

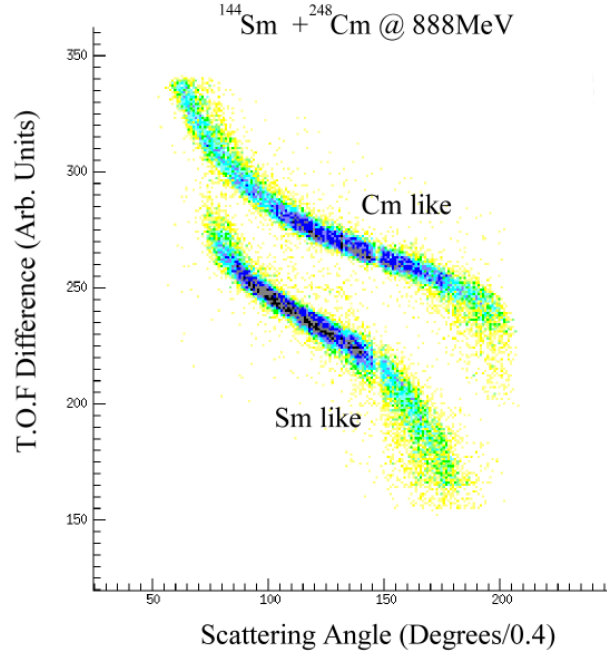


Figure 3.15: Particle identification. Measurement of the time-of-flight difference and scattering angles allows the two scattering solutions to be cleanly separated. The time difference for the two solutions is 6.6 ns at 45° (channel 112)

3.3.6 Time Measurement and Particle Identification

The target-like and projectile-like nuclei can be identified if they are detected in coincidence by plotting the scattering angle against the time-of-flight difference (Δ_{TOF}). An example of this is shown in Figure 3.15. The mass of each nucleus can also be calculated with the assumption of two-body kinematics by

$$m_1 = \frac{\Delta_{TOF_{1,2}} + (d_2/P_2)M_{tot}}{(d_1/P_1) + (d_2/P_2)} \quad (3.3)$$

where $\Delta_{TOF_{1,2}}$ is the time-of-flight difference for the left and right nucleus, and d_1 and d_2 are the length of the flight path for the left and right nucleus, respectively. The momenta of the left and right nuclei ($P_{1,2}$) are given by Equation 3.1. A calculated mass spectrum is shown in Figure 3.16 for the reaction $^{144}\text{Sm} + ^{248}\text{Cm}$ at a lab energy of 888 MeV.

The resolution of the time-of-flight difference measurement is about 0.7 ns. The various experimental factors contributing to the time resolution for a typical beam

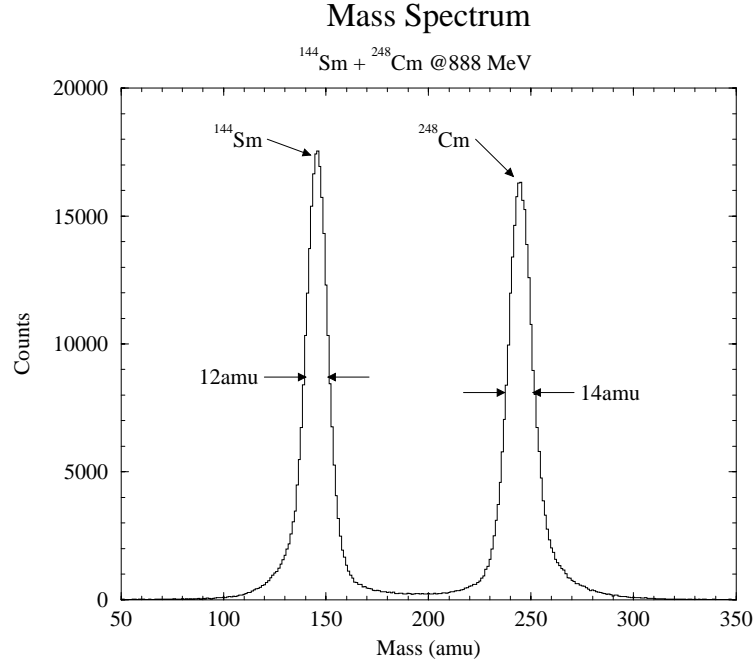


Figure 3.16: Measured mass spectrum from the reaction $^{114}\text{Sm} + ^{248}\text{Cm}$ at 888 MeV.

experiment, in this case a beam of 780 MeV (lab energy) ^{162}Dy on a $250\mu\text{g}/\text{cm}^2$ ^{118}Sn target, can be calculated and are shown in Table 3.2. Typical values for the energy (E_{strag}) and angle (θ_{strag}) straggle of the beam and ejectile nuclei as they pass through the target material are shown, along with their contribution to the time resolution. The location of the reaction within the target material also effects the time of flight, since the beam and scattered nuclei lose energy as they pass through the target material. This contribution to the time resolution is listed in Table 3.2 under “Target Thickness”. The largest contribution to the time resolution uncertainty is the beam spot size. Because of the short flight path (~ 13 cm) to the detectors, the 3 mm beam spot subtends about 1° with respect to a given point on the detectors. The energy of the scattered nuclei varies rapidly enough with scattering angle for this to be the major contribution to the time resolution. The resolution of the electronics can be measured from the “self-gated” time, which should yield a narrow peak. The time measurement is “self gated” for the particle which fulfills the valid event requirement, for instance the second particle to reach the counter when looking for coincidences. The average

Time Resolution (ns)	
Measured Width	~ 0.7
E_{strag}	
Dy (0.8MeV)	~ 0.01
Sn (0.6MeV)	~ 0.04
θ_{strag}	
Dy (0.3°)	~ 0.05
Sn (0.1°)	~ 0.02
Target thickness	~ 0.1
Beam spot (3mm)	~ 0.4
Electronic Resolution	~ 0.2
Intrinsic Resolution	~ 0.52

Table 3.2: Contributions to the time resolution for 780 MeV ^{162}Dy on a $250\mu\text{g}/\text{cm}^2$ ^{118}Sn target.

width for the “self-gated” time peak is 0.2 ns. The intrinsic time-difference resolution, after unfolding all of these contributions, is about 500ps, or 350ps for a single PPAC.

3.3.7 Performance of GAMMASPHERE with CHICO

The impact of CHICO on the response characteristics of GAMMASPHERE is an important consideration when coupling these two detectors. The CHICO detector was designed to have as little mass as possible within the scattering chamber of GAMMASPHERE to minimize scattering and absorption of γ rays. Simulations modeling the influence of CHICO on the response of GAMMASPHERE were performed [30] using the Monte Carlo code GEANT [31]. The peak efficiency (Figure 3.17) and the peak-to-total ratio (Figure 3.18) for GAMMASPHERE were modeled with and without

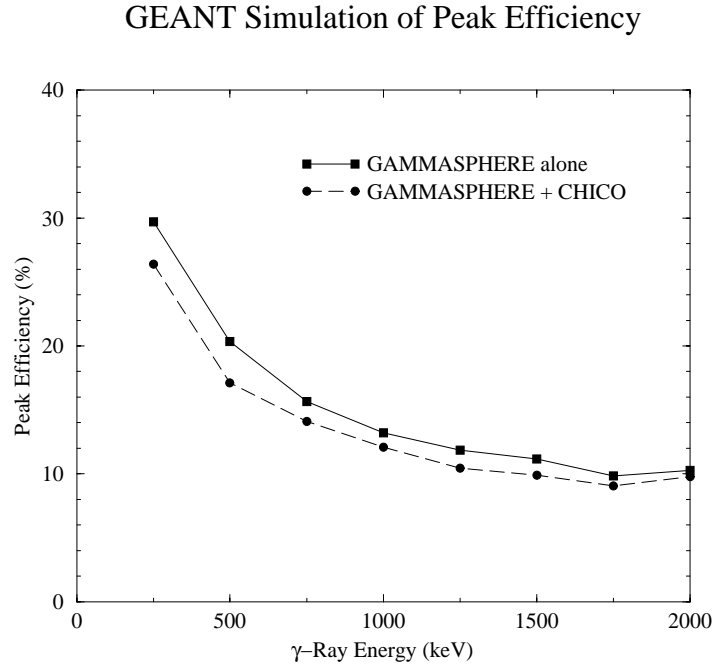


Figure 3.17: GEANT simulation of the effect of CHICO on the peak efficiency of GAMMASPHERE for γ -rays emitted at the target location.

the presence of CHICO. The peak efficiency simulation over predicts the performance of GAMMASPHERE, giving a value of 11.8% compared to the measured value of 9.9%. The simulation shows that the presence of CHICO decreases the peak efficiency of GAMMASPHERE by about 12%, from 11.8% to 10.4% for a 1.25 MeV γ ray. The simulations reproduce the measured peak-to-total ratio of 0.6 quite accurately for a 1.25 MeV γ ray and indicate that the influence of CHICO reduces the peak-to-total ratio from 58.3% to 51.3%, that is 12%.

3.4 Summary

A heavy-ion detector was constructed which can be used with GAMMASPHERE. The detector measures scattering angles of the reaction products over a solid angle of 2.8π sr with 1° resolution and time-of-flight difference with 500 ps resolution. This information can be used to identify the target-like and projectile-like nuclei, reconstruct the kinematics of each event, and perform the Doppler correction on the γ rays on an

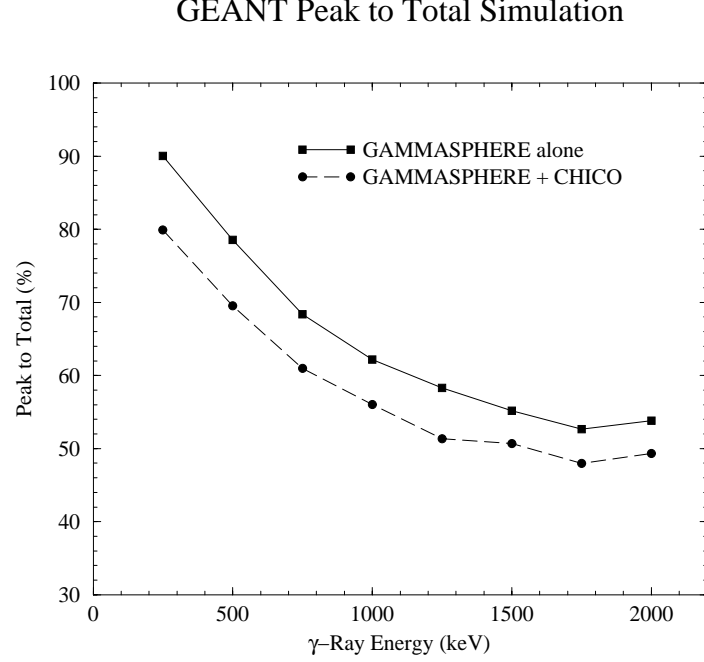


Figure 3.18: GEANT simulation of the effect of CHICO on the peak-to-total ratio of GAMMASPHERE for γ -rays emitted at the target location.

event-by-event basis. The masses of the nuclei can be resolved to $\Delta m/m = 5\%$. The detector has a minimum amount of mass within the GAMMASPHERE scattering chamber, and hence minimally degrades the response characteristics of GAMMASPHERE. The design of the detector included development of compact high-gain amplifiers and a strip line transmission line, allowing the amplifiers to be placed within the detector housing, reducing problems with electronic noise. The development of three-layer cathode boards yielded improved position resolution.

The detector has become an important part of the GAMMASPHERE program and has been used to study a variety of physics by various reactions including the Coulomb excitation and production of neutron-rich nuclei in the mass ≥ 160 region via transfer reactions [3, 32], searches for double-octupole phonon strength in ^{208}Pb [33, 34] and ^{96}Zr [35], a feasibility study of populating trans-uranic nuclei via heavy-ion transfer [36], population of the neutron-rich nuclei in the $50 < A < 90$ region using a fusion-fission reaction [37], a study of K -forbidden transitions in ^{178}Hf by Coulomb excitation [38], and spontaneous fission of $^{252}\text{Cf}(\text{SF})$, described in the present work.

Chapter 4

^{252}Cf Spontaneous Fission Experiment Description

4.1 Introduction

As mentioned in the introduction, spontaneous fission provides a method for the study of neutron-rich nuclei. The technique of using the latest generation of large γ -ray detector arrays in conjunction with a fission-fragment detector expands the research opportunities for the study of properties of neutron-rich nuclei produced in spontaneous fission. In previous experiments using these large γ -ray detector arrays, thick fission sources were used which stopped the recoiling fission fragments within the source ([10, 39, 40, 41], for example). The stopping times of the recoiling fission products in the source are on the order of $\sim 10^{-12}$ seconds. Transitions with lifetimes on the order of the stopping times suffer Doppler broadening, limiting the observation of high-spin transitions. The data collected in these experiments comprise high-statistics high-fold γ ray-events. By using a fission-fragment detector with these large γ -ray detector arrays additional information and selectivity can be achieved. In the present experiment the heavy-ion detector CHICO was coupled to the γ -ray detector array GAMMASPHERE and a thin fission source was used, allowing the fission fragments to recoil into vacuum and be detected in coincidence with the de-excitation γ rays of the fission products. The additional information gained from

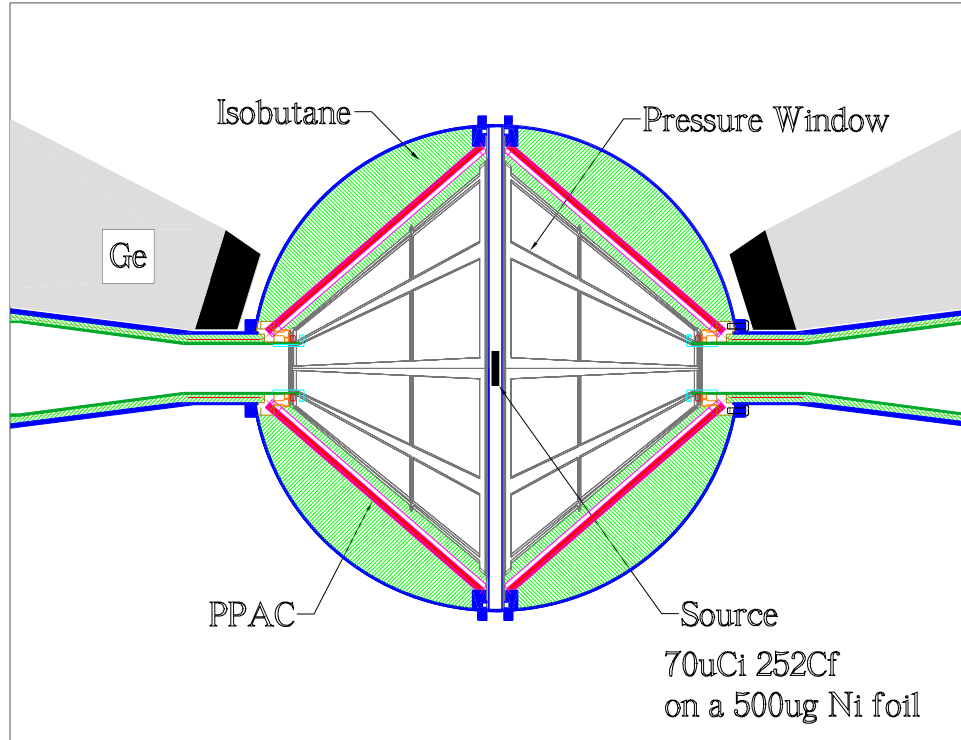


Figure 4.1: Schematic of the fission experiment setup. The PPAC array (CHICO), is shown with two representative GAMMASPHERE Ge detectors and the fission source.

the coincident detection of the fission fragments with their de-excitation γ rays results in greater selectivity and provides a means of extracting more information from each fission event. The mass division can be measured, allowing the sorting of the copious γ rays by mass region, and provides a means of assigning the γ rays to either the heavy or light fission partner. Since the fission partners recoil into vacuum, the problem of Doppler broadened line shapes is eliminated, allowing the observation of levels at higher spin and excitation energies. The experimental method, analysis, and selectivity achievable with this technique are described in this chapter.

4.2 The Experiment

The experiment was conducted using GAMMASPHERE at Lawrence Berkeley National Laboratory. The experimental setup (Figure 4.1) comprises the CHICO

detector, GAMMASPHERE (both described in Chapter 3), and a “thin” 70 μCi ^{252}Cf spontaneous fission source that allows the fission fragments to leave the source. Details of the source and choice of spontaneously fissioning isotope are discussed in section 4.2.1.

The CHICO detector detects the recoiling fission fragments, measuring the time-of-flight difference and direction of the fragment’s flight. GAMMASPHERE coincidentally measures the energy and direction of the de-excitation γ rays emitted by the fission fragments. The experiment was conducted with 86 Ge detectors installed in GAMMASPHERE. Graded absorbers made of 0.127 mm (0.005 in.) Cu and Ta foil were placed over the γ -ray detectors and 0.508 mm (0.020 in.) Pb absorbers were placed over the BGO detectors to attenuate x-rays. Events with two particles and at least 3 γ rays were collected at a rate of ~ 4000 events/second. The experiment ran for about 80 hours in which total of $\sim 9 \times 10^8$ events were recorded.

4.2.1 The Fission Source

Selection of the proper spontaneous fission source material is critical to the success of this type of thin source experiment. The choice of a suitable spontaneously fissioning isotope is limited by availability and isotopic properties such as the half-life and strength of the spontaneous fission decay branch. Previously, thick source experiments with large γ -ray detector arrays have been performed with ^{248}Cm ([39, 40] for example), ^{242}Pu [10] and ^{252}Cf [10, 41]. A primary consideration in the selection of isotope for thin source is the amount of source material needed since the fission fragments need to be able to leave the source material without appreciable energy loss. The amount of fissioning isotope needed is proportional to the half-life and inversely proportional to the fission branching-ratio. These quantities, along with the mass of material needed for a source with the strength as used in the present experiment, are shown in Table 4.1.

Of these, ^{252}Cf is the most suitable for a thin source. A ^{252}Cf source of sufficient strength is essentially massless, with about 90 nanograms of isotope needed. A source of the same strength made from ^{248}Cm would require about 4 milligrams of material,

isotope	$\tau_{\frac{1}{2}}$	$BR_{SF}(\%)$ [43]	mass (g) for a 80k/sec source
^{242}Pu	$3.73 \cdot 10^5 \text{ y}$	$2.13 \cdot 10^{18}$	6.86
^{248}Cm	$3.4 \cdot 10^5 \text{ y}$	$1.30 \cdot 10^{14}$	$4.28 \cdot 10^{-3}$
^{252}Cf	2.645 y	$2.71 \cdot 10^9$	$9.08 \cdot 10^{-8}$

Table 4.1: Selection criteria for a thin fission source isotope.

making it marginal since too much energy would be lost by the fission fragments passing through the source material. A ^{242}Pu source of the same strength would be unusable since the fission fragments would not make it out of the $\sim 7 \text{ g}$ of required source material.

The fission source used in this experiment consisted of $70 \mu\text{Ci}$ of ^{252}Cf electroplated to a region about 1 cm in diameter on a $500 \mu\text{g}/\text{cm}^2$ Ni foil. The source was mounted in CHICO with a $20 \mu\text{g}/\text{cm}^2$ carbon foil covering the fission material to prevent self-transport of the ^{252}Cf . The nickel and carbon foils are thin enough to allow the fission fragments to leave the source. The source was produced by Mark Stoyer at Lawrence Livermore National Laboratory.

4.3 Thick Source Data

Some of the data presented in this thesis, the Rh level diagrams and Pd spectra in Chapter 5 and the ^{135}I spectrum in Section 6.3, is from a thick source $^{252}\text{Cf}(\text{SF})$ experiment [41, 42]. This experiment was performed with a $25 \mu\text{Ci}$ ^{252}Cf source sandwiched between two 0.5 mil Ni foils and two 2 mil thick Al foils. The experiment was performed with GAMMASPHERE with 72 Compton suppressed Ge detectors and a total of 9.8×10^9 triple or higher fold γ -ray coincidence events were collected.

4.4 Analysis

The measured quantities in the thin source experiment are the time-of-flight difference of the fission partners and the Doppler shifted energies of the γ rays. This

section describes how the relevant quantities, the mass division between the fission partners and the transition energies are extracted from the experimental data.

4.4.1 Mass Measurement

The average value of the total kinetic energy released for a given mass division ($TKE(M_H, M_L)$), and its standard deviation ($\sigma_{TKE(M_H, M_L)}$), in spontaneous fission of ^{252}Cf are well measured quantities [44, 45, 46, 47]. The $TKE(M_H, M_L)$ can be used to calculate the initial recoil velocities of the emitted fission fragment pairs. With the inclusion of experimental considerations, such as energy loss of the recoiling fission fragments in the target material and geometric variation of the flight path length, the experimentally measured time-of-flight difference can be used to deduce the mass division and final velocities of the fission fragments on an event-by-event basis. Rather than using an iterative algorithm analyzing each event separately, where the initial mass division is guessed, then corrected for energy loss effects, and repeated until convergence, which would be computationally time consuming, the time-of-flight-difference as a function of mass division and fission axis orientation was calculated (as described below) and stored in a look-up table. The quantities important to the subsequent analysis, the final velocities of the fission fragments, mass division, and the time of the fission, t_0 with respect to the detected coincidence, can then be retrieved based on the measured time-of-flight-difference and fission axis orientation.

For binary fission events, the initial velocities of the two fission fragments can be calculated. Conservation of momentum constrains the two fragments to have equal and opposite momenta. The kinetic energies ($KE_{H,L}$), velocities ($v_{H,L}$), and time-of-flight difference (Δ_{TOF}) of the complimentary heavy and light fragments with masses M_H and M_L , respectively, are given by:

$$KE_{H,L} = \frac{M_{L,H}}{M_L + M_H} TKE(M_H, M_L) \quad (4.1)$$

$$v_{H,L} = \sqrt{\frac{2M_{L,H} TKE(M_H, M_L)}{(M_{H,L})(M_L + M_H)}} \quad (4.2)$$

$$\Delta_{TOF} = \frac{d_L(\theta_L, \phi_L)}{v_L} - \frac{d_H(\theta_H, \phi_H)}{v_H} \quad (4.3)$$

where $d(\theta, \phi)$ is the flight path length which is dependent, due to the geometry of the detector, on the orientation of the fission axis.

The recoiling fission fragments travel either through the $500\mu\text{g}/\text{cm}^2$ Ni backing foil, or the $20\mu\text{g}/\text{cm}^2$ carbon cover foil during their flight to the particle detectors. The fragments will loose some of their kinetic energy as they travel through the material, effecting their final recoil velocities. The amount of energy lost depends on both the nuclear charge and velocity of the fission fragments and the amount of material through which they pass. For a given mass division the nuclear charge $Z_{H,L}$ of the heavy and light fragments were assumed to be proportional to the masses, $Z_{H,L} = \frac{M_{H,L}}{M_H + M_L} Z_{tot}$ where $M_H + M_L$ sums to 252 amu, the nuclear mass of ^{252}Cf , and Z_{tot} is the total nuclear charge of $98e$. The amount of backing foil or cover foil material that the fission fragments travel through is inversely proportional to the cosine of the angle of fission axis. The energy loss was calculated using the program ENELOSS [48]. The final velocities of the fission fragments were then calculated by subtracting the energy lost in the nickel backing foil or carbon cover foil from the initial kinetic energies $KE_{H,L}$ given in Equation 4.1.

The Δ_{TOF} depends on the flight path distance $d(\theta, \phi)$ of the fragments, which in turn depends on the geometry of the detector and the θ and ϕ angle of the fission axis. For the geometry of CHICO the distance from the target to the PPAC is given by

$$d(\theta, \phi) = \frac{d_{\perp}}{\cos(\theta)\sin(41^\circ) + \sin(\theta)\cos(41^\circ)\cos(\phi')} \quad (4.4)$$

where d_{\perp} is the distance from the target to the PPACs along the normal (12.8 cm) and ϕ' is with respect to the centerline of a given PPAC.

Figure 4.2 shows the dependence of the calculated masses on the time-of-flight difference and angular orientation of the fission axis. The time-of-flight difference maps into a unique mass division for a given θ, ϕ orientation of the fission axis. At large angles, above about 70° , there is significant energy loss in the target material and the coincidence particle detection efficiency drops (see Figure 4.3).

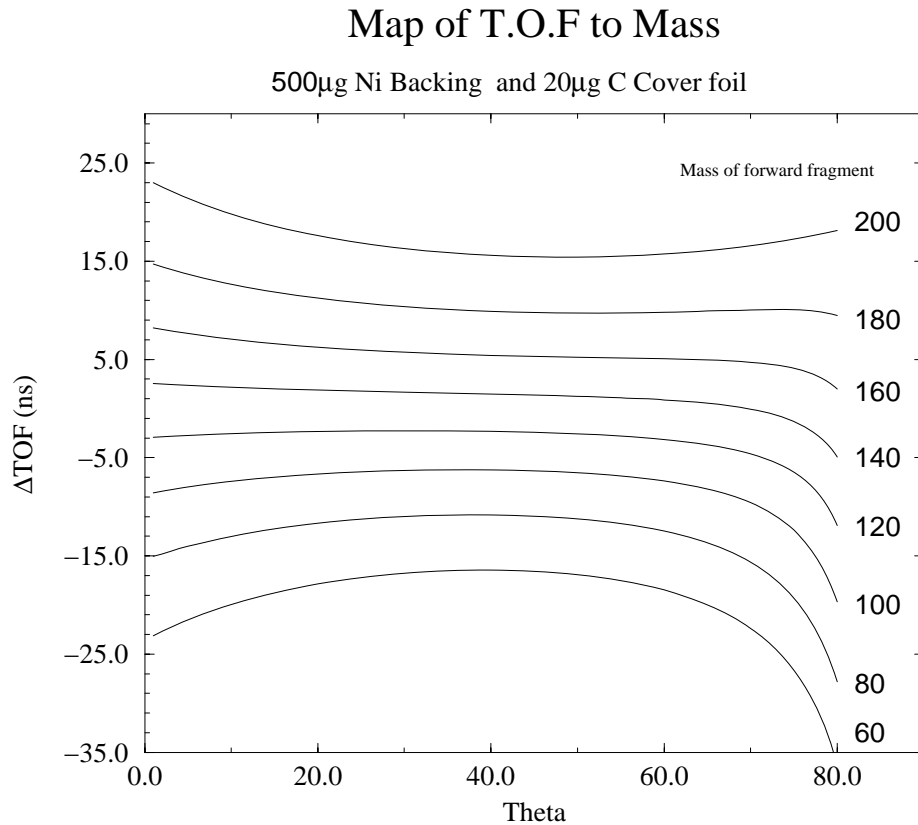


Figure 4.2: The mass division between the fission partners can be uniquely mapped from the time-of-flight difference of the recoiling nuclei and angular position of the fission axis.

The resolution of the mass measurement based on the time-of-flight is about 8 mass units (FWHM). The resolution was measured by gating the γ -ray spectra on transitions in specific nuclei and projecting the measured mass for these events. An example of the mass measurement based on the time-of-flight difference is shown in Figure 4.4.

4.4.2 Gamma-ray Analysis

Doppler Correction

The fission fragments leave the source with velocities on the order of a few percent of the speed of light. The measured energies of the γ rays emitted during the flight

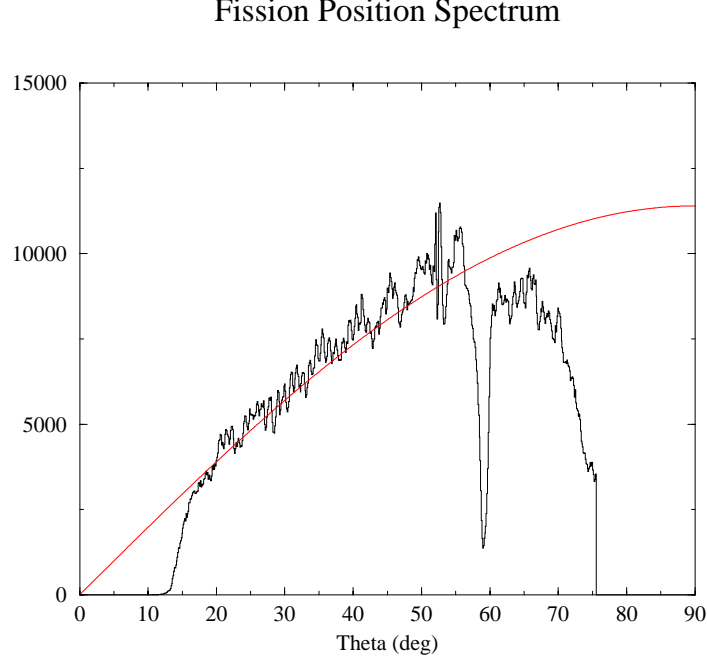


Figure 4.3: Position spectrum from the $^{252}\text{Cf}(\text{SF})$ experiment. The solid line shows the expected solid-angle dependence of the yield. Above 60° the yield drops due to target effects.

of the fission fragments are appreciably Doppler shifted and need to be transformed back to their rest frame to extract the transition energies. The transformation of the γ energies to their rest frame is given by

$$E = E' \frac{1 - \beta \cos(\theta'_{p\gamma})}{\sqrt{1 - \beta^2}} \quad (4.5)$$

where E is the true transition energy in the de-exciting nuclei's rest frame, E' is the energy measured in the lab frame, $\theta'_{p\gamma}$ is the angle between the fission fragment velocity vector and the direction of the emitted γ ray in the lab frame, and $\beta = \frac{v}{c}$. The time-of-flight-difference measurement provides the velocities of the fragments, as discussed in section 4.4.1. The angle between the emitted γ ray and the direction of travel of the nuclei, $\theta'_{p\gamma}$, is known since the orientation of the fission axis (θ_p , ϕ_p) is measured by CHICO, and the direction of the γ ray (θ_γ , ϕ_γ) is measured by GAMMASPHERE. The angle $\theta'_{p\gamma}$ is given by

$$\cos(\theta'_{p\gamma}) = \sin(\theta_p)\sin(\theta_\gamma)\cos(\phi_\gamma - \phi_p) + \cos(\theta_p)\cos(\theta_\gamma) \quad (4.6)$$

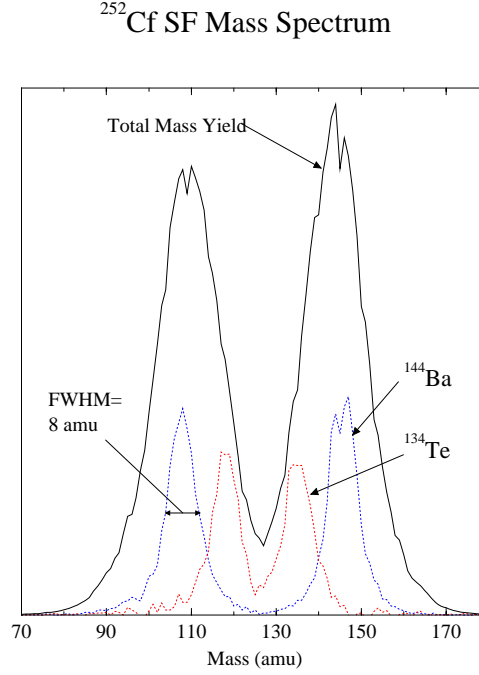


Figure 4.4: Measured Mass Resolution. The measured mass for individual nuclei are projected by setting double gates on γ ray transitions. The relative intensities of the mass distributions are not to scale.

where θ_p , ϕ_p and θ_γ , ϕ_γ are the direction of travel of the nuclei and γ ray, respectively.

The γ -ray line shapes in the raw spectra are broad and flat due to the Doppler shift. Sharp γ -ray line shapes are recovered by performing the Doppler correction on an event-by-event basis. It is not known a priori whether a detected γ ray was emitted from the heavy or light fission partner and, hence, it is not determined whether the Doppler correction should be performed for the heavy or light nucleus. In the application of the heavy (light) Doppler correction to the data set, the sharp γ ray line shapes are recovered for the heavy (light) nuclei's γ rays, and the light (heavy) nuclei's γ -ray line shapes are broadened further. A simulation of the effect of the correct and incorrect Doppler correction is shown in Figure 4.5.

γ Ray Resolution

The γ -ray resolution is an important quantity for experiments of this type. The analysis relies heavily on examining the γ -ray coincidence relationships both from

Light fragment γ -ray

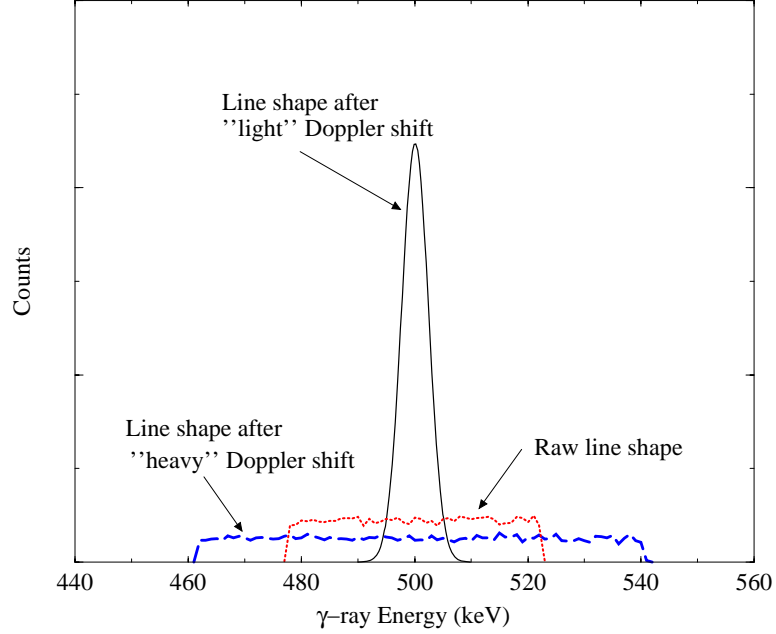


Figure 4.5: Effect of heavy/light Doppler correction on raw γ data. This figure shows the results of a simulation of the raw line shape and the line shapes after the complimentary Doppler corrections are applied.

individual nuclei and correlated fission pairs by setting gates on specific γ -rays. Since there are over one hundred daughter nuclei populated in the spontaneous fission of ^{252}Cf , each of which may have ~ 10 distinct transitions, there will be transitions in different nuclei which have nearly the same energy. Gates on γ rays which overlap with “spurious” nuclei will introduce false correlations. It is necessary to check that the energy resolution is optimized to reduce this problem.

The full-width-half-maximum (FWHM) of the γ -ray peaks can be described with the function

$$FWHM = (A_1^2 + A_2^2(\sqrt{E})^2 + A_3^2(E)^2)^{\frac{1}{2}} \quad (4.7)$$

where A_1 is related to the noise in the detector and amplifier, A_2 is related to the counting statistics of the charge collection within the γ -ray detectors, and A_3 is related to the Doppler broadening of the γ -ray peaks [49]. For situations where the

de-exciting nuclei have no recoil velocity, such as in thick target experiments or the use of γ -ray calibration sources, the term $A_3=0$. The measured resolution along with the contributions from each of the terms in Equation 4.7 for the fission experiment is shown in Figure 4.6 and the intrinsic resolution for GAMMASPHERE is shown in Figure B.2. The noise and counting statistics terms for the fission experiment and calibration sources show good agreement. The γ -ray energy resolution for the fission experiment is dominated by the Doppler broadening term.

Primary contributions to the Doppler term A_3 of Eqn. 4.7 in the fission experiment are the angle uncertainty in the direction of the γ ray due to the opening angle of the γ -ray detector and the variation in the total kinetic energy, σ_{TKE} , for a given mass division. The statistical variation in total kinetic energy of the fission products in spontaneous fission of ^{252}Cf is on the order of 10 MeV out of 180 MeV, leading to a variation of about 3% in fragment velocity, or about 0.1% variation in the Doppler corrected energy of the γ rays. The Doppler corrected energy also is dependent on the angle between the direction of travel of the γ ray and the fission fragment and is described by the relation

$$\frac{dE}{E} \approx \beta \sin(\theta_{p\gamma}) d\theta_{p\gamma} \quad (4.8)$$

The γ -ray detectors have an opening half-angle of $\sim 7^\circ$ (0.12 rad). For typical recoil velocities of $\beta \simeq 0.04$, the error in the Doppler corrected energy due to the angle uncertainty is about 0.5% for γ -ray detectors located at 90° to the fission axis, where the solid-angle is a maximum. These contributions account for nearly all of the degradation of resolution, and for the current experiment cannot be improved upon.

4.5 Gamma-ray Spectrum Analysis

The development of large γ -ray detector arrays allows high-fold detection of high multiplicity γ -ray events. The coincidence relationships between γ rays in these high-fold events carry the information used in construction of level diagram and identification of correlated nuclei. Examination of the coincidence relationships of γ rays from the same nucleus determines the decay sequences of that nucleus, from which

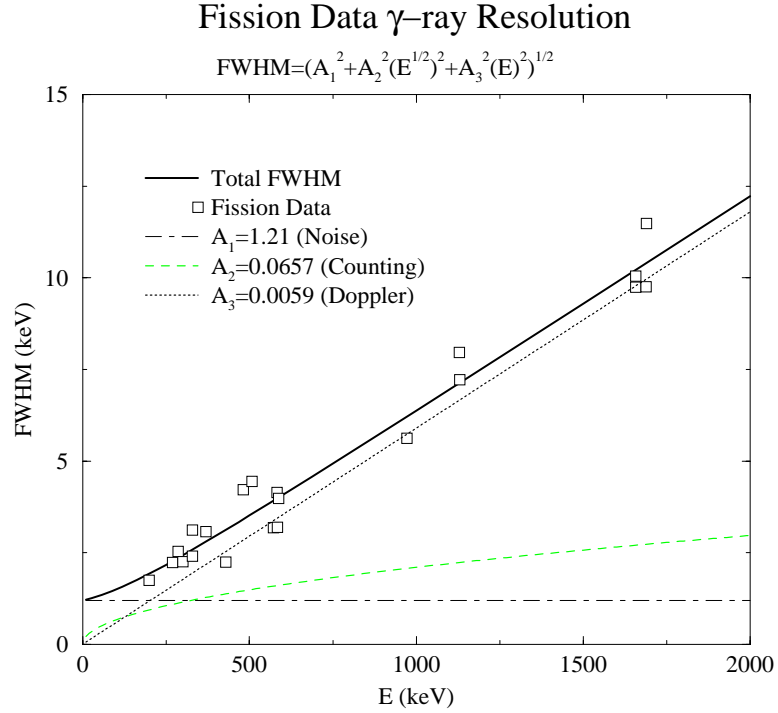


Figure 4.6: Measured γ -ray energy resolution in the thin source $^{252}\text{Cf}(\text{SF})$ experiment. The effect of detector noise, counting statistics and Doppler broadening are included.

the level diagram can be deduced. The coincidence relationships among γ rays from partner nuclei can identify which reaction products are correlated. In the case of this thin source fission experiment, the γ rays for either the heavy or light fission partner can be selected by means of the Doppler correction, as shown in section 4.4.2. The level diagrams for the fission products can be constructed by examination of coincident γ rays with the same applied Doppler correction. The identification of correlated fission partners is performed by using the correlations between γ rays with complimentary applied Doppler corrections.

The analysis of γ ray coincidence relationships is performed by sorting events with three or more γ rays into three-dimensional histograms, or cubes, where the axis of the cube represent the energy of the γ rays. For events with more than three γ rays, all sub-combinations of γ - γ - γ -triples are “unpacked” from the higher order n-tuples and histogrammed. The γ -ray correlations can then be studied by setting gates on two axis of the cube and projecting onto the third axis. The multiplicity distribution

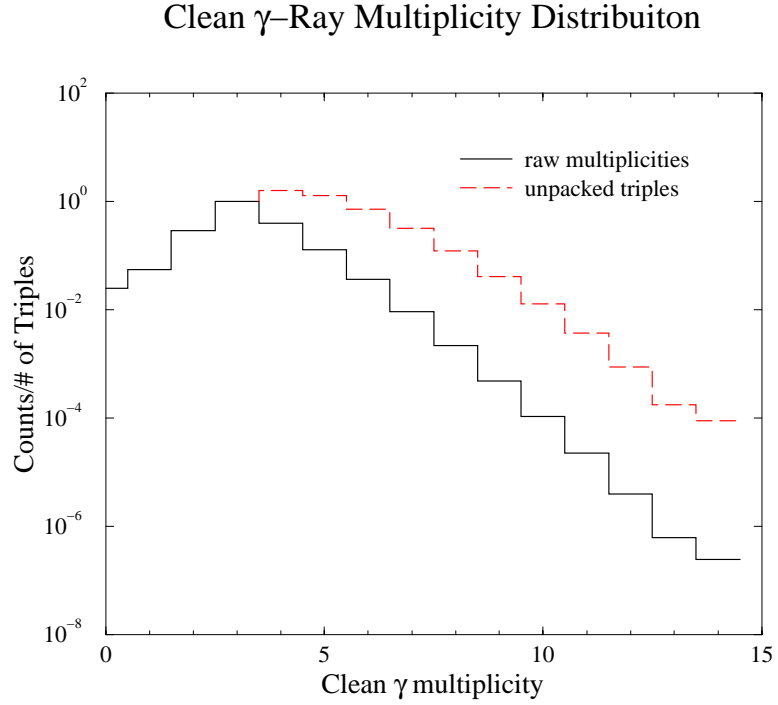


Figure 4.7: The multiplicity distribution (normalized to the number of triple events) and number of unpacked triples from clean γ rays events from the thin source $^{252}\text{Cf}(\text{SF})$ experiment.

of clean γ rays and number of unpacked triples for the thin source fission experiment is shown in Figure 4.7. The largest contribution of triples to the histogram is from unpacked four-fold γ -ray coincidences.

Symmetric Cubes

The symmetric cubes are created by histogramming the unpacked γ - γ - γ events with the same type of Doppler correction, either heavy or light, applied to each of the γ rays. In practice, the γ -ray triples are ordered in energy before histogramming ($E_{\gamma_1} > E_{\gamma_2} > E_{\gamma_3}$) and each γ -ray triple is only histogrammed once. This requires only one sixth of the storage space needed compared to a cube where all permutations are histogrammed, and still carries the same information. The gating and display software LEVIT8R [49] used in the analysis of the symmetric cubes performs the necessary unfolding of the one sixth cube when gates are applied to the cube.

The symmetric cubes were used for developing the level diagrams for the nuclei populated in the present thin source $^{252}\text{Cf}(\text{SF})$ experiment. The events that are useful for developing the level diagrams are those with which three or more γ -rays originate from the same nucleus. Gating the cubes on known transitions in a specific nucleus projects out coincident transitions of the possible decay sequences which include the gated transitions. The γ -ray triples can have one, two, or three of the γ rays emitted by the partner of the nucleus of interest, but these events are not observed in the projected spectra since the application of the Doppler correction broadens the line shapes of the γ rays from the partner nuclei to a level near the background.

Asymmetric Cubes

Asymmetric cubes are data structures which have two axis that are symmetric, where the γ rays have the same type of applied Doppler correction, and the third axis where the γ ray has the complimentary Doppler correction applied. A given γ -ray triple is histogrammed three times, once with each γ ray of the triple histogrammed along the asymmetric axis and the other two along the symmetric axes. The pair of γ rays histogrammed along the symmetric axes are again ordered by energy ($E_{\gamma_1} > E_{\gamma_2}$) before histogramming to save storage space.

Analysis of the γ -ray coincidence relationships from the thin source data between two correlated nuclei was performed with asymmetric cubes. Setting gates on transitions in a nucleus along the symmetric axes projects out transitions from the partner nuclei. This procedure can be used to identify the nucleus of origin for unknown decay sequences. If the partner nuclei can be identified, then, since the nuclear charge is conserved in the fission process, at least the charge of the nucleus from which the gated transitions originated can be identified.

Background subtraction

There are several sources of background in the γ -ray spectra. The Compton suppression in the GAMMASPHERE Ge detectors does not remove all of the Compton scattering events, reflected in the peak-to-total ratio of 0.6. There are also statistical

γ rays from decay of nuclei populated in the quasi-continuum region which do not give discrete γ -ray peaks. For the thin source fission experiment, γ rays which are histogrammed with the wrong Doppler correction also contribute to the background. In the analysis of the symmetric cubes the software package LEVIT8R subtracts a background built from the cross-products of lower-dimensional projections of the three-dimensional histograms. The three-dimensional background is defined as

$$B_{ijk} = \frac{1}{T} [M_{ij}b_k + M_{ik}b_j + M_{jk}b_i] + \frac{1}{T^2} [-P_i b_j b_k - b_i P_j b_k - b_i b_j P_k + b_i b_j b_k] \quad (4.9)$$

where T is the total number of counts in the histogram, M is the total two-dimensional projection of the cube, P is the total one-dimensional projection of the cube onto one axis, and b is the background drawn under the total projection P [50]. For the symmetric cubes, the three two-dimensional projections, M , and the total projections, P , and the 1 dimensional total background, b , are the same regardless of which direction the projections are taken.

A background subtraction was implemented based on Equation 4.9 for the analysis of asymmetric cubes. The background for spectra projected from the asymmetric cubes use the same method, except the two dimensional projections, total projections, and backgrounds are different depending on which direction the projections are taken. Performing a background subtraction in the analysis of asymmetric cubes is important since the background from events histogrammed with the wrong combination of Doppler corrections is three times as large as for the symmetric cubes.

4.6 Selectivity

4.6.1 Mass Gating

The measurement of the mass division of the fission partners provides additional selectivity and enhances the ability to study nuclei produced with low yield. The γ -ray data can be histogrammed with gates set on the measured masses of the fission fragments. Selecting γ rays from specific mass regions reduces the γ -ray “back-

ground” of the nuclei which are not of current interest which allows observation of weak transitions which might otherwise be obscured.

As an example, the prompt γ rays from ^{166}Dy were observed in a mass-gated spectra of the thin source $^{252}\text{Cf}(\text{SF})$ (Figure 4.8). ^{166}Dy is produced in $^{252}\text{Cf}(\text{SF})$ at a level of $4.9 \cdot 10^{-5}$ of the total mass yield [51]. The yrast band was observed by summing multiple double-gates on the yrast transitions. The yrast band of ^{166}Dy has been previously identified to a spin of $16\hbar$ in the $2n$ transfer reaction $^{118}\text{Sn}(^{164}\text{Dy}, ^{166}\text{Dy})^{116}\text{Sn}$ performed using CHICO in conjunction with GAMMASPHERE [3]. The same gates used to produce the top spectrum in Figure 4.8 with a symmetric cube were applied to an asymmetric cube to project out the fission partner γ rays. Two γ rays from the Dy fission partner Ge were observed to be in coincidence, confirming that the observed rotational band belongs to Dy.

4.6.2 Selectivity Provided by the Doppler Correction

The application of the Doppler correction allow the γ rays to be assigned unambiguously to either the heavy or light fission partner, and, with the application of appropriate γ -ray gates, spectra which include sharp γ -ray peaks from only one nucleus can be generated. In the thick source experiments, since the γ -rays are emitted after both the fission partners come to rest in the source material, it is not possible to identify from which nucleus the γ ray originates without relying on the systematics of the γ ray coincidence relationships. The thick source spectra gated on γ rays of one particular nucleus brings back not only coincident γ rays from that nucleus, but also γ rays from the several partner nuclei. Setting gates on symmetric cubes from the thin source data, where the applied Doppler correction broadens the γ -ray line shapes from the partner nuclei, provide spectra which have γ rays only from the nucleus of interest. The resultant spectra are more straight forward to interpret. Spectra with the same gates on transitions in ^{104}Mo from the thick source and thin source data are shown in Figure 4.9.

The Doppler correction in conjunction with the geometry of CHICO provides a method of separating γ rays from prompt decays from γ rays emitted after decays of

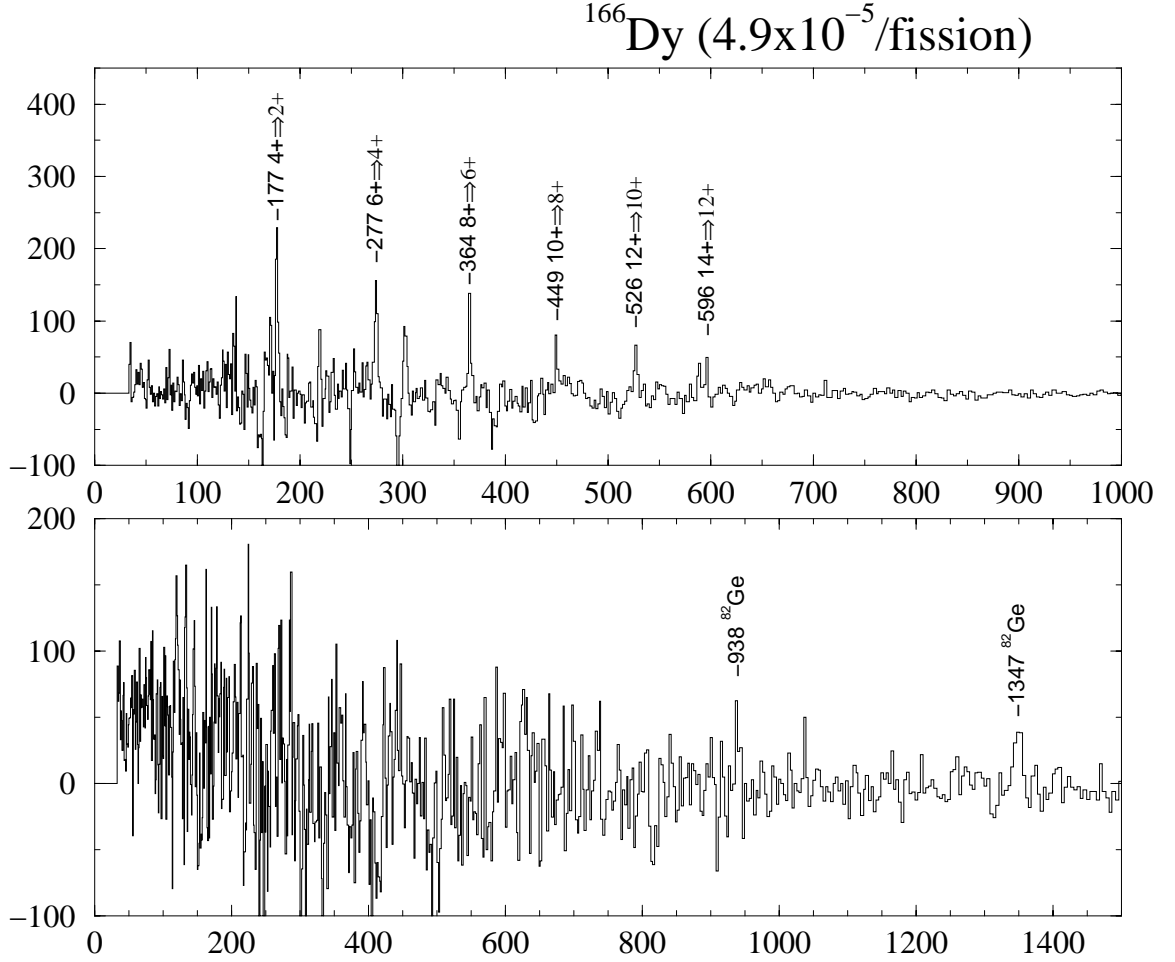


Figure 4.8: Observation of ^{166}Dy in $^{252}\text{Cf}(\text{SF})$. The top figure shows the ground rotational band of ^{166}Dy . The bottom figure shows the coincident transitions in ^{82}Ge .

isomeric levels. The prompt γ rays which are emitted during the ~ 15 ns flight of the fission partners are seen as sharp peaks in the γ -ray spectra only after the Doppler correction is applied. After the nuclei implant in the PPACS, the emitted γ rays are observed as sharp peaks in the spectra only if no Doppler correction is applied since the nuclei no longer have a recoil velocity. Figure 4.10 shows a γ -ray spectrum with no Doppler correction applied.

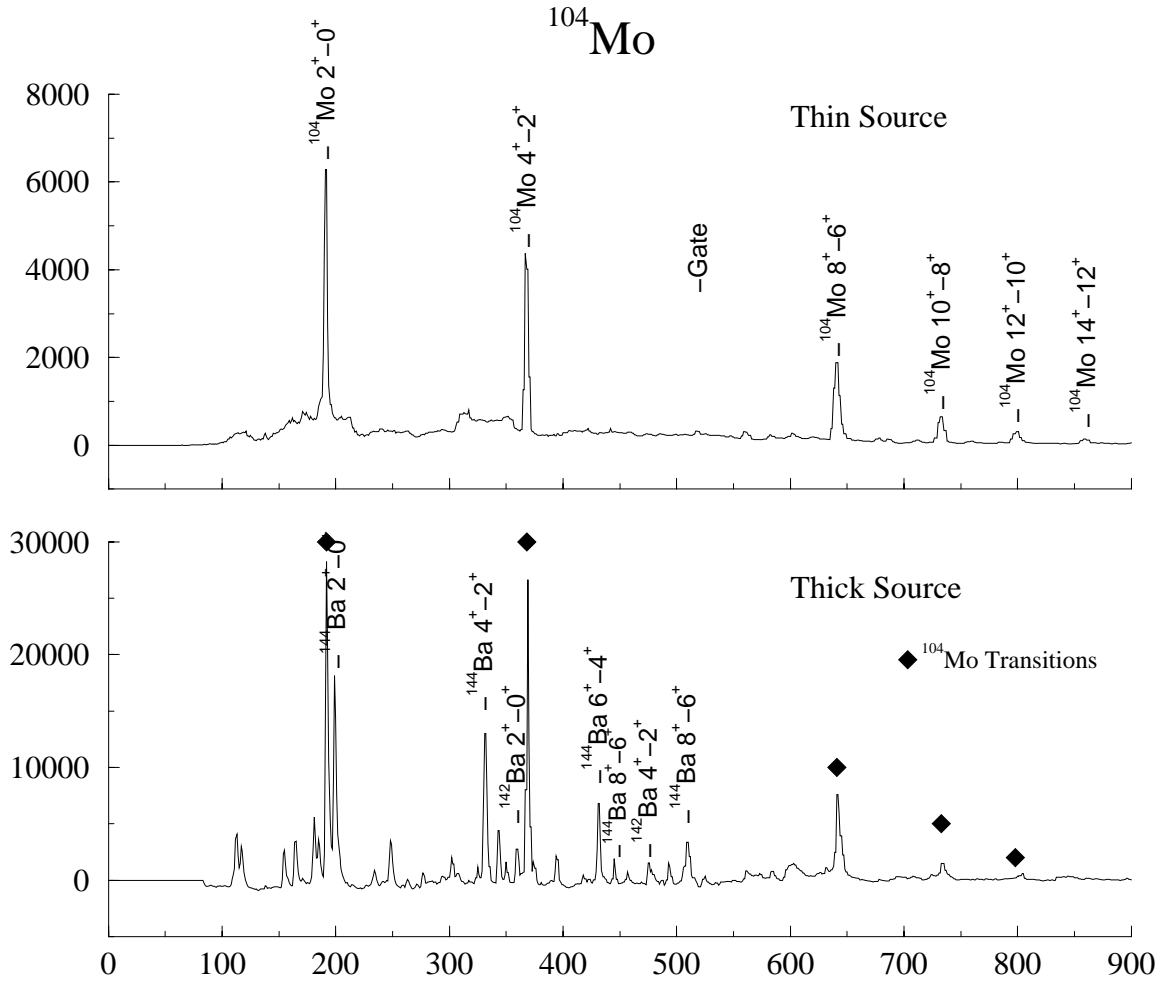


Figure 4.9: The top figure shows a gated spectrum from the thin source data. The bottom spectra is with the same applied gates in the thick source data.

4.6.3 H-K Measurement

GAMMASPHERE can perform as a high efficiency sum spectrometer. The BGO crystals in the Ge detectors used for the Compton suppression can also be used as high-efficiency low-resolution γ -ray detectors. The BGO crystals were calibrated (see Section B) and the total energy and multiplicity of the fission events were recorded. The total energy included “clean” γ rays, Compton scattered events, and BGO only events. The total energy and multiplicity (H-K) and the projections are shown in Figure 4.11.

Isomeric Transitions

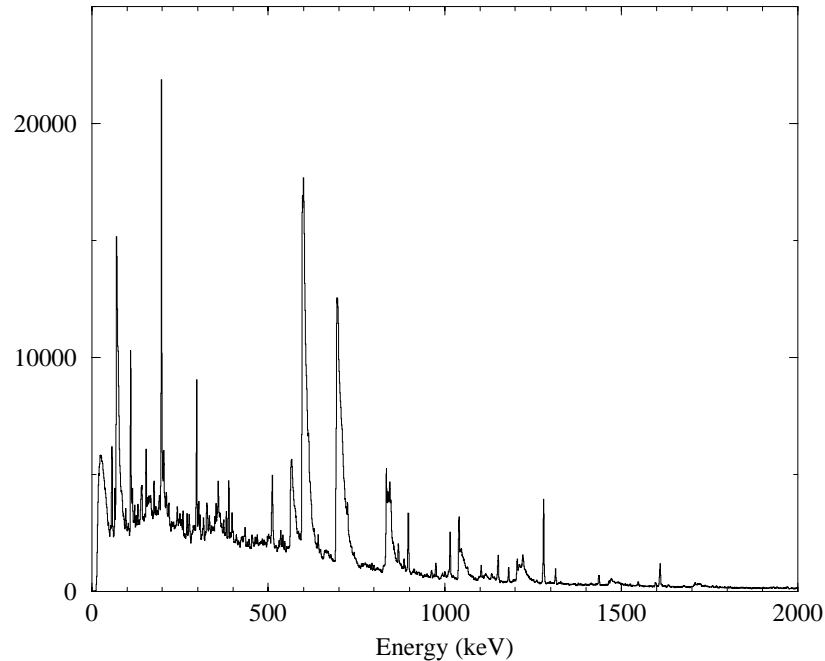


Figure 4.10: Delayed γ ray “isomer” spectrum.

The H-K information can be used to gate the γ -ray spectra. A difference in relative intensities of peaks in spectra gated on different H-K regions would indicate that the total γ -ray energy and multiplicity is dependent on the mass division between the fission partners. Two spectra gated on the regions shown in Figure 4.11c are shown in Figure 4.12 and there are differences between these spectra. This selectivity can be used to study the dynamics of the fission process, but lies beyond the scope of this thesis.

4.6.4 Observation of Levels at Higher Spins and Excitation Energy

The use of a thin source makes it possible to observe transitions at higher spins and excitation energies than with the thick source experiments. In the thick source

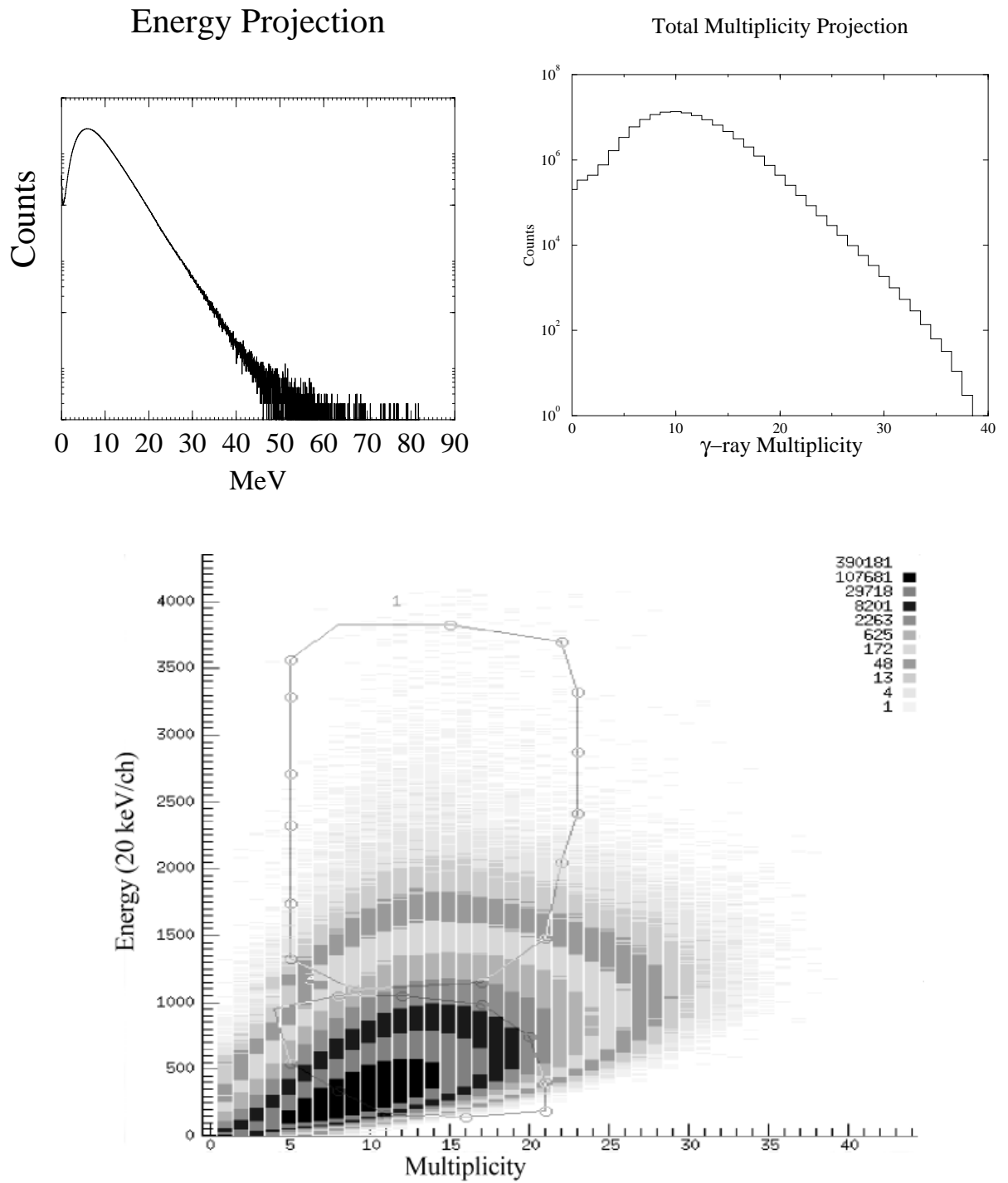


Figure 4.11: Total energy and multiplicity in $^{252}\text{Cf}(\text{SF})$.

H-K Gated γ -ray Spectra

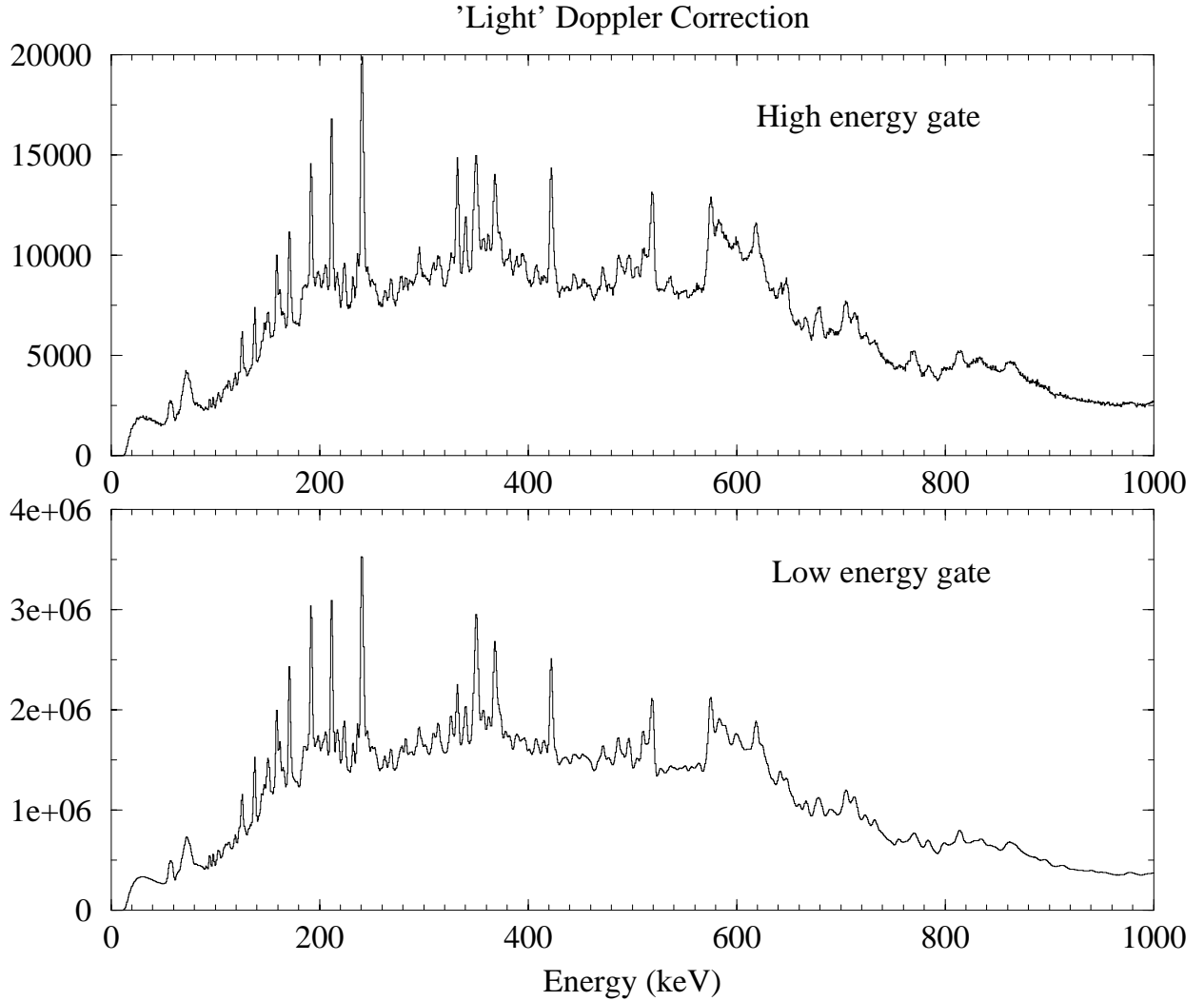


Figure 4.12: γ ray spectra with the 'light' applied Doppler correction gated on the total energy and multiplicity regions shown in Figure 4.11. The top figure is from the higher total energy region and the lower figure is from the lower total energy region.

experiments, the recoiling fission fragments slow down and stop in the source in ~ 1 ps. Gamma rays emitted during the slowing down process are Doppler shifted and, hence, the line shapes of γ rays from transitions with lifetimes comparable to the stopping times are Doppler broadened. In the thin source experiment most of the γ -rays are emitted while the fission partners are recoiling at their full Coulomb-accelerated velocities. After the Doppler correction is applied, there is no line-shape broadening

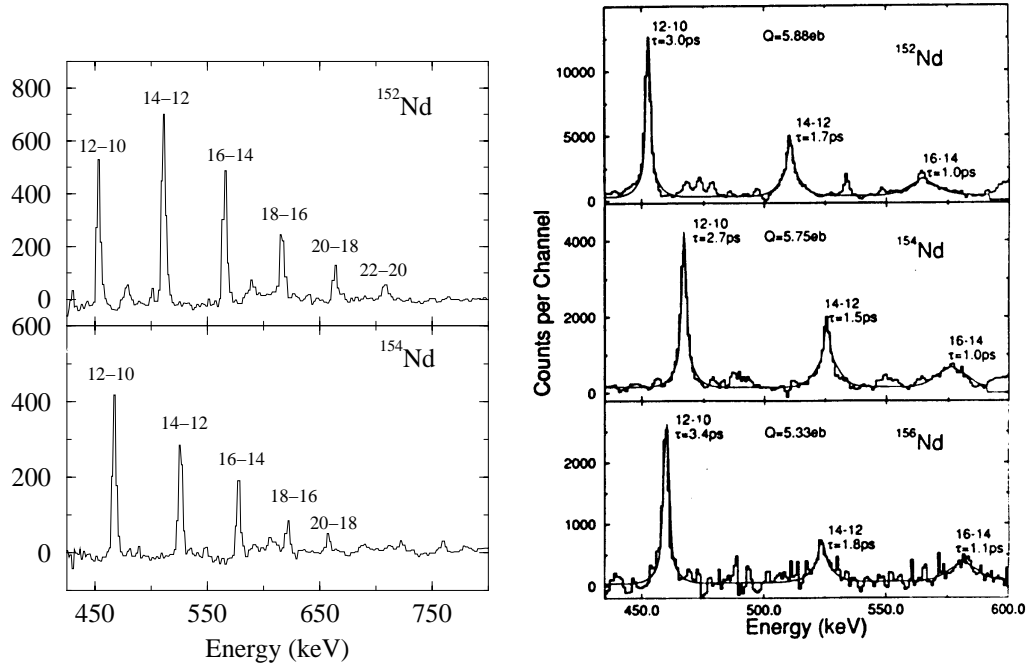


Figure 4.13: Using a thin source eliminates Doppler-broadened line shape problems and allows observation of levels with shorter lifetimes and high spin. The spectrum on the right [40] is from ^{248}Cm in a KCl crystal and shows the effect Doppler-broadening has for higher lying transitions.

as for recoiling fragments in a thick source. Sharp line-shapes for transitions with lifetimes on the order of the ~ 1 ps stopping time are recovered. Spectra showing transitions from the same isotopes observed in the thick and thin source experiments are shown in Figure 4.13, and the effect of the Doppler broadening can be seen in the thick source spectra. Typically in the thin source data the level spectrum can be extended by two or more levels, allowing observation of levels with spin up to $20\hbar$ and excitation energies of ~ 7 MeV. The extension of rotational band structures is seen not only for the yrast bands, but also for the more weakly populated side bands. Level diagrams that have been extended are shown in Chapter 7.

4.7 Summary

A technique of studying fission products of $^{252}\text{Cf}(\text{SF})$ using a large solid-angle particle detector array (CHICO) with the latest generation of γ -ray detector arrays (GAMMASPHERE) was developed. In this experiment, high-statistics data consisting of high-fold γ -ray events along with the time-of-flight of the fission partners were collected. The additional information provided by the coincident detection of the fission products provides selectivity and sensitivity beyond what is possible with thick fission source experiments. The time-of-flight-difference provides a means of measuring the masses of the fission products with a resolution of ~ 8 amu. The mass information can be used to gate the γ -ray spectra allowing the study of nuclei produced with low yield. A detection sensitivity to a yield of $\sim 10^{-5}$ /fission was achieved.

Since the fission products recoil freely into vacuum, the de-excitation γ rays emitted during the flight of the fission products need to be Doppler corrected. This allows the γ rays to be unambiguously assigned to either the heavy or light fission product. The resultant spectra are cleaner, since they contain γ rays from only one species, either heavy or light, of fission product. Levels at higher spins and excitation energies are observable in this experiment than in the thick source experiments since the γ -ray line-shapes are not Doppler broadened due to the stopping times of fission products in the source. Rotational bands can typically be extended by a few levels.

Chapter 5

Neutron $h\frac{11}{2}$ band structures in the neutron-rich Pd

5.1 Introduction

The neutron-rich nuclei Pd are in a region of the nuclear landscape where interesting shape-related properties occur. For example, the low-lying energy level structure and measured γ -ray branching ratios of neutron-rich Ru are consistent with stable tri-axial quadrupole deformations [52, 53]. Also, the even mass neutron-rich Pd and Mo nuclei have a low-lying 2^+ bands indicating the importance of the γ -shape parameter. Theoretical calculations of the ground state shapes for the neutron rich Pd predict a shape change from prolate to oblate with increasing neutron number. Calculations of the quadrupole potential energy landscape using the Nilsson-Strutinsky method, with the cranked Woods-Saxon average potential and a monopole pairing residual interaction, show that these nuclei could have shallow minima making them susceptible to γ -vibrations or even stable triaxial deformation, and that minima at both prolate and oblate shapes might exist [54]. This calculation predicts a shift in the ground state shape from prolate to oblate with increasing neutron number for the even mass Pd beyond ^{114}Pd . Calculations using the finite range liquid drop model predict the shift from prolate to oblate shapes to occur at mass 111 for the Pd [55, 56]. Experimentally observed properties of the neutron-rich nuclei provide a

means of testing the predictive power of the various models.

Since the neutron-rich Pd isotopes are unstable to β decay, direct measurements of the shape-related properties, such as the $E2$ matrix elements along with their relative phase, are currently not experimentally feasible. The high-spin behavior of the yrast rotational bands, however, can be used to deduce the shape properties of the ground state configurations. The high-spin behavior of the palladium nuclei in this region has been studied recently by a variety of reactions. Heavy-ion fusion-evaporation reactions were used to populate $^{107,108}\text{Pd}$ and the neighboring ^{109}Ag [57], deep-inelastic reactions were used to investigate ^{108}Pd [58], and $^{109,111}\text{Pd}$ were studied via a fusion-fission reaction [59]. While the above reaction mechanisms allow some selectivity of the resultant nuclei, there is a limit to how far from stability toward the neutron rich side that these reactions can reach. Population of the neutron-rich Pd currently relies on either spontaneous or induced fission of a heavy nucleus. The levels of neutron-rich Pd observed via induced fission have been observed through the β decay of Rh [60, 61, 62] and hence have yielded little information on the high spin behavior. High spin states in neutron rich $^{112,114,116}\text{Pd}$ have been observed in previous $^{252}\text{Cf}(\text{SF})$ experiments using the high efficiency of large γ -ray arrays [64, 42]. The high-spin properties of these nuclei are of interest since the band crossings can be observed, giving evidence of the nuclear shape.

As noted in Ref. [64], the yrast band structures of $^{112,114,116}\text{Pd}$ are similar, having band crossings of nearly identical moments of inertia. The authors of Ref. [64] attribute the first band crossings in these nuclei to the alignment of a $\pi(g_{\frac{9}{2}})^2$ pair based primarily on comparison to cranked shell model calculations performed with the assumption of oblate shapes predicted by the finite range droplet model [55]. This conclusion was made without the benefit of either the observation of the completion of the back bend, from which the total aligned angular momentum can be measured, or knowledge of rotational bands in neighboring odd A nuclei, both of which can be used to deduce the type of orbital involved in the alignment. In subsequent work, the properties of the rotational bands based on $\nu h_{\frac{11}{2}}$ levels observed in the odd neighboring nuclei $^{109,111}\text{Pd}$ have confirmed the $\nu(h_{\frac{11}{2}})^2$ nature of the band crossings observed in the even $^{110,112}\text{Pd}$ ground state bands [59], implying prolate shapes for these nu-

clei. Since the moments of inertia are so similar for $^{112,114,116}\text{Pd}$, the discrepancy in the identification of the orbitals responsible for the band crossing in ^{112}Pd calls into question the proposed [64] $\pi(g_{\frac{9}{2}})^2$ nature of the band crossings in $^{114,116}\text{Pd}$.

In the present work rotational bands in the odd neutron $^{113,115}\text{Pd}$ and odd proton $^{111,113}\text{Rh}$ [72] have been identified, as well as additional levels in the even-even $^{112,114,116}\text{Pd}$. The band crossings in these rotational bands give evidence that the aligning nucleons occupy $\nu(h_{\frac{11}{2}})^2$ orbitals. Comparison with cranked shell model calculations suggest that $^{114,116}\text{Pd}$ nuclear shapes are prolate for the ground state configurations.

5.2 $^{113,115}\text{Pd}$ Ground Bands

The low-lying levels ($\lesssim 1$ MeV) of ^{113}Pd have been identified previously in β -decay of ^{113}Rh [61]. The ground state of ^{113}Pd was assigned a spin and parity of $\frac{5}{2}^+$ based on the properties of its β -decay to ^{113}Ag [70], with a configuration based on a mixture of the spherical shell model neutron states $2d_{\frac{5}{2}}$ and $1g_{\frac{7}{2}}$ [71]. Other levels and spin assignments observed in Ref. [61] and relevant to this work, are at 455 and 190 keV. The level at 455 keV (with no previous spin or parity assignment) decays directly to the ground state and also by a 265 keV γ ray to the level at 190 keV. The 190 keV level has been assigned a spin and parity of $\frac{7}{2}^+$ and its decay to the ground state is by an M1 transition [61]. The 190, 265, and 455 keV transitions are also observed in both the thick and thin fission source data sets. Gates on these transitions in the thick source data clearly show the coincidence of these lines with several of the Te fission partners (Figure 5.1). The coupled bands shown in the level diagram (Figure 5.2) were constructed by relying on the γ -ray coincidence relationships elucidated by setting various combinations of double gates in the thin source data cubes. The spin assignments for these levels are tentative and are based on the probable spin of $\frac{7}{2}^+$ assigned to the 190 keV level in Ref. [61] and on the decay pattern of the band. The highest spin and excitation energy observed for this band is $\frac{23}{2}$ at 2705 MeV.

The construction of the ground band of ^{115}Pd from transitions seen in $^{252}\text{Cf}(\text{SF})$ is similar to the method described for ^{113}Pd . The low lying levels are known from β

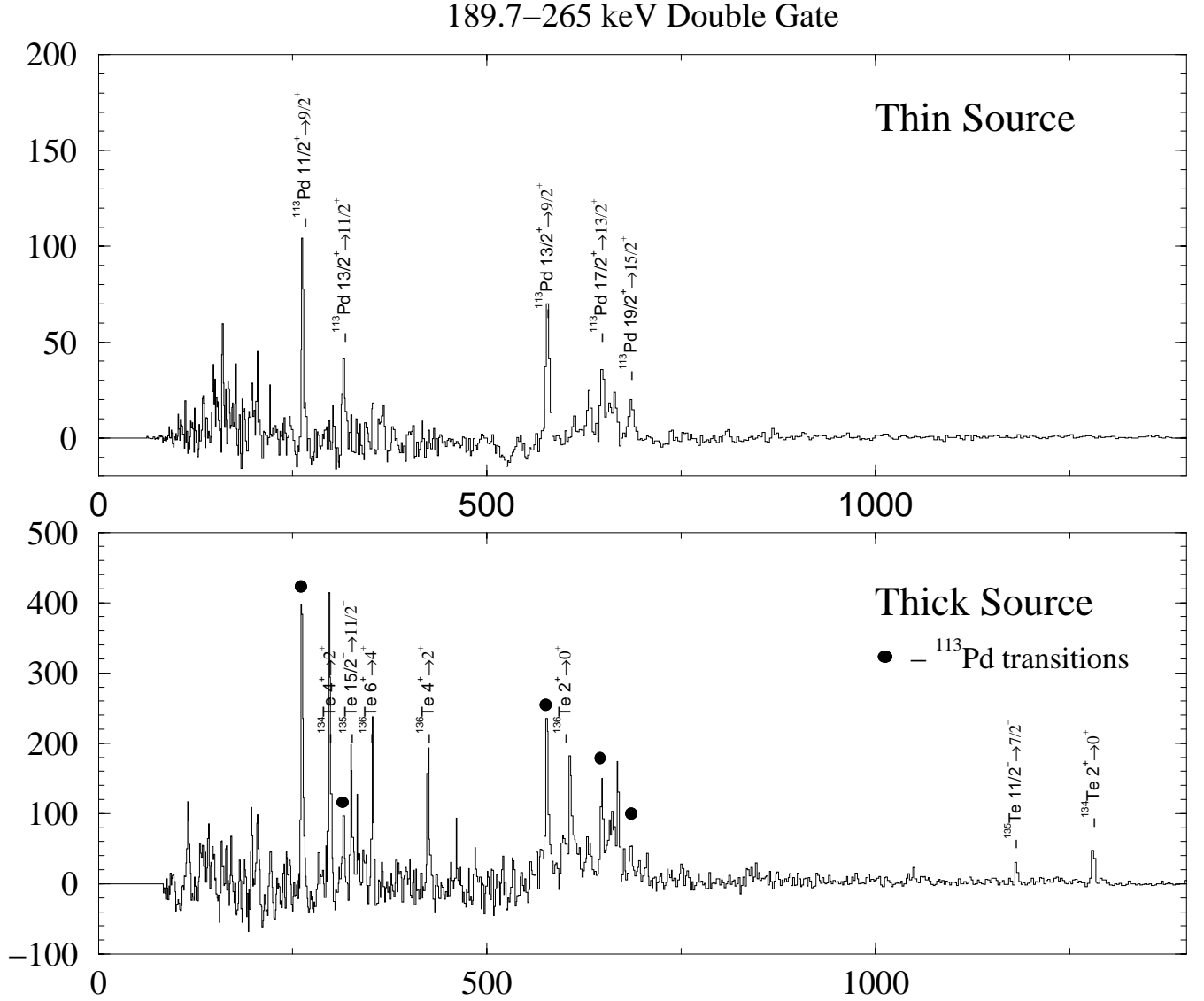
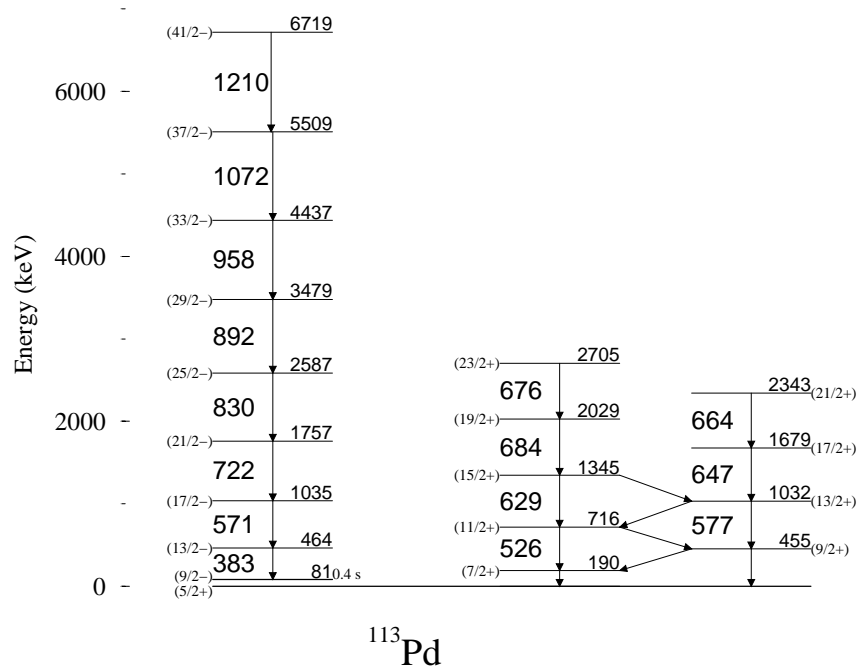


Figure 5.1: Spectra double gated on the 189.7 and 265 γ -rays in the thin (upper) and thick (lower) source data

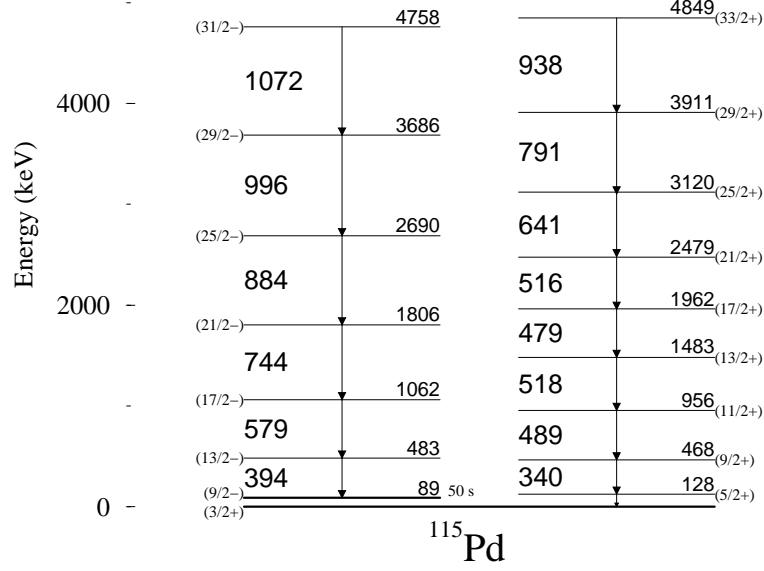
decay of ^{115}Rh [70, 62]. The adopted ground state spin of ^{115}Pd was assigned to be $\frac{5}{2}$ with positive parity in Ref. [65] based on odd Pd systematics, but Ref. [66] assigns a spin of $\frac{3}{2}$. In the present work we will assume the more recent value of $\frac{3}{2}$ for this level. Levels decaying to the ground state which are observed both in β -decay and fission are at 468 keV and 128 keV. The 468 keV level decays to the 128 keV level with the emission of a 340 keV γ -ray. By setting gates in the fission data on the 340,

Figure 5.2: ^{113}Pd level diagram

128 keV γ -cascade de-populating the 468 keV level, other coincident transitions are observed. Again, the coincidence relationships used to identify members of the band, and the observed intensities were used to order the transitions within the band. Only one signature of this band was seen, and the band was observed to a presumed spin of $\frac{37}{2}$ and an excitation energy of 4894 MeV.

5.3 Isomeric bands in $^{113,115}\text{Pd}$

The odd palladium nuclei beyond ^{101}Pd are known to have a negative parity band built on a decoupled $\nu h_{11/2}$ orbital (see Figure 5.4). As the neutron Fermi level rises with increasing neutron number, the band head energy drops, reaching a minimum at ^{113}Pd , just past the middle of the neutron shell. These negative parity band heads become isomeric for ^{107}Pd and beyond. The spins for the band heads are $\frac{11}{2}^-$ through ^{111}Pd , whereas the most probable spin for the band head changes to $\frac{9}{2}^-$ for ^{113}Pd and ^{115}Pd [61]. The decay of these isomeric levels is strongly hindered with respect

Figure 5.3: ^{115}Pd level diagram

to Weisskopf single-particle estimates, for example the hindrance factor for the M2 decay of the $\frac{9}{2}^-$ isomeric level in ^{113}Pd to the ground state is 7600[61]. The authors of [61] suggest that large shape differences between the ground state and isomeric state could be the cause of these large hindrance factors, possibly providing evidence to the predicted minima for prolate and oblate shapes in this region.

The decay of these isomeric levels in $^{113,115}\text{Pd}$ have been observed in isotopes separated after induced fission [70, 61]. The separation process in these experiments requires time on the order of tenths of milliseconds, so the prompt γ rays feeding the isomers were not observed. Experiments observing the prompt γ rays can be used to identify the bands feeding these isomeric levels. For example, heavy-ion induced fission in conjunction with prompt γ -ray spectroscopy has been used to observe the rotational bands based on the isomers in $^{109,111}\text{Pd}$ [59]. In the present work the rotational bands based on the ground state and the isomeric state in $^{113,115}\text{Pd}$ have been identified by prompt spectroscopy of ^{252}Cf spontaneous fission products.

The rotational band built on the isomeric configurations in $^{113,115}\text{Pd}$ were observed

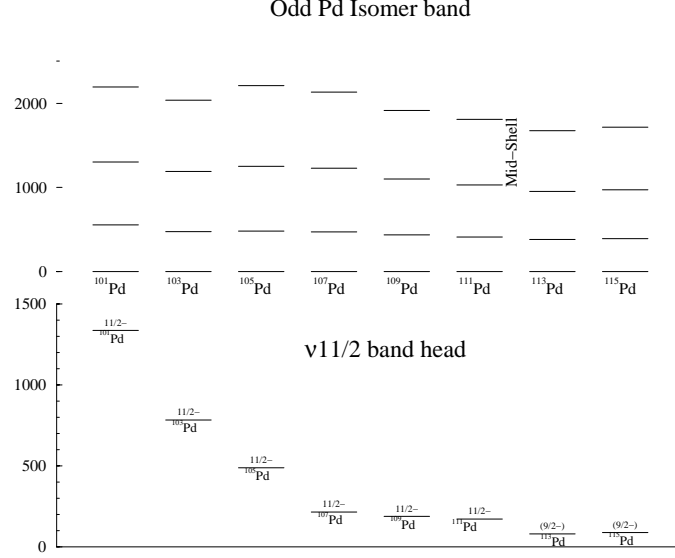


Figure 5.4: Systematics of $\nu h \frac{11}{2}$ band heads in the odd Pd isotopes.

in both the thick source and thin source data sets in the present work. Because of the long half life of the band heads, their decay to the ground state is not observed in the spontaneous fission experiments, and no transitions were observed linking these bands to the ground band. Assignment of these bands to Pd isotopes are based on the coincidence with γ -decays from Te, the partner nuclei in $^{252}\text{Cf}(\text{SF})$, and assignment to either ^{113}Pd or ^{115}Pd is based on the average mass of the Te partners.

Spectra resulting from gates on the transitions in the isomer band in ^{113}Pd in the thick source data show the coincidence of the fission partner Te γ rays (Figure 5.5c). The spectrum resulting from the same gates in the thin source data, where the Pd-like Doppler shift has been applied, is shown in Figure 5.5a. In thin source data the ^{113}Pd band is observed to a spin of $\frac{41}{2}$. Higher spins are observed in the thin source data since the Doppler broadening of the line shapes due to the stopping times of the fission fragments, as happens in the thick source experiment data, is eliminated. Because of the Doppler correction, the Te gamma ray peaks are broadened and difficult to observe in this spectrum. The coincident partner γ rays can be recovered from the thin source data by using “asymmetric cubes”, where events with three or more γ rays are sorted with a “light” (Pd-like) Doppler shift on two of the axis and a “heavy”

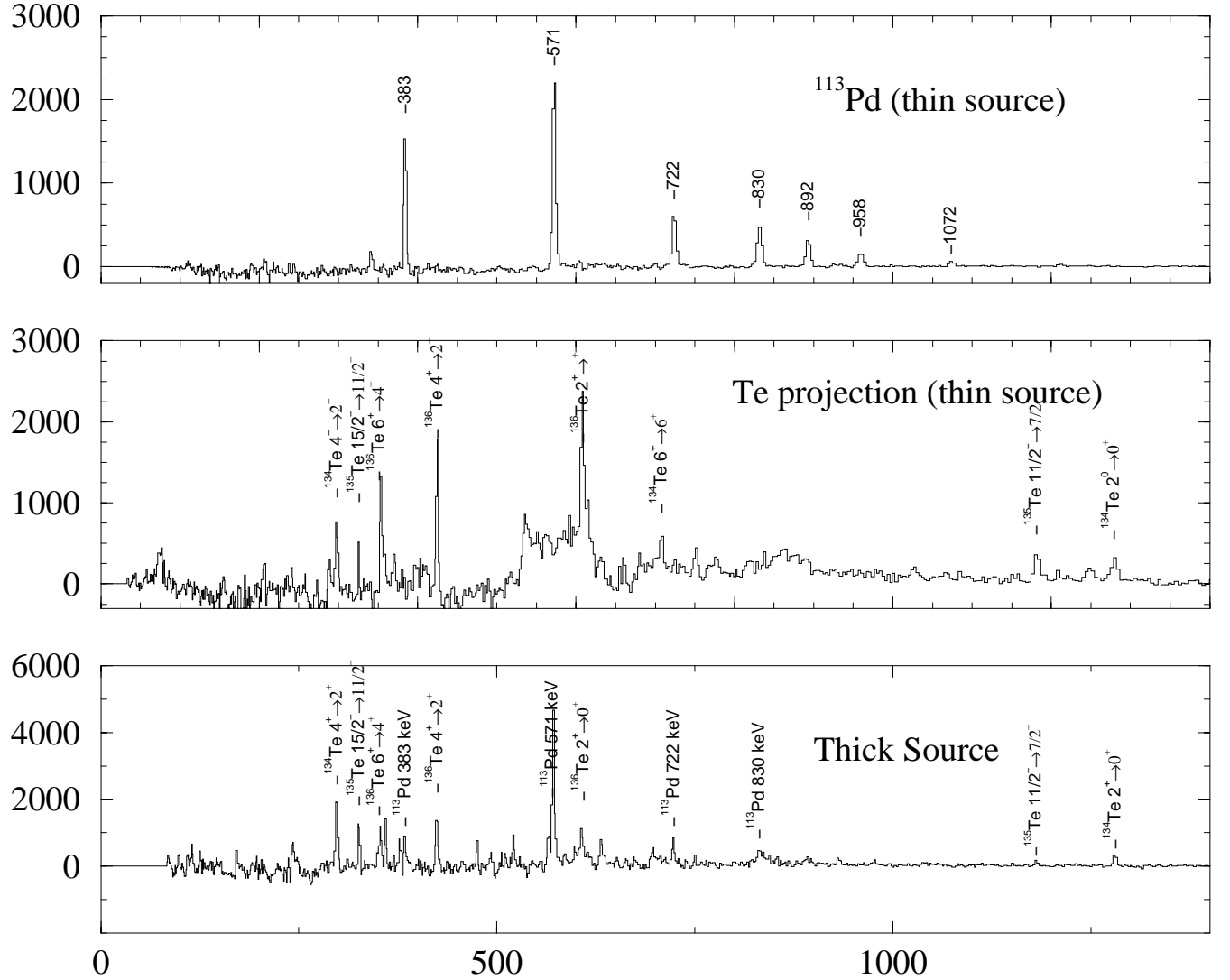


Figure 5.5: Identification of ^{113}Pd isomer band. The top spectra (a) is from the light Doppler shifted thin source $^{252}\text{Cf}(\text{SF})$ data. The middle spectra (b) is from an asymmetric cube from the thin source $^{252}\text{Cf}(\text{SF})$ data with the Te coincident transitions projected out. The bottom (c) spectra is from a thick source experiment [10, 41]

(Te-like) Doppler shift on the third axis. Setting gates on the two symmetric axis then projects out the γ rays of the heavy (Te-like) partner. The spectrum shown in Figure 5.5b shows such a projection of the fission partner Te γ rays in coincidence with the ^{113}Pd $\frac{9}{2}^-$ band transitions from the thin source experiment data.

The assignment of the isomer bands to either ^{113}Pd or ^{115}Pd is accomplished by

taking a mass weighted average of the $2^+ \rightarrow 0^+$ transition intensities of the even Te partner nuclei. Since the Te isotopes have isomers up to ~ 200 ns, this was done with the thick source data. The time window for collecting γ rays for the thick source experiment was $1 \mu\text{s}$, long enough so that the $2^+ \rightarrow 0^+$ yield represents the true mass yield since decays of levels populated below the isomeric level, decays that bypass the isomeric levels, and decay chains that are trapped in the isomeric levels and subsequently decay all are collected within this time. The Doppler corrected thin source data do not provide yields representing the mass production when there are levels with long lifetimes in the decay chain since only the γ rays emitted during flight are recovered. The average masses of the Te partner nuclei for $^{112-116}\text{Pd}$ are shown in Figure 5.6, and the isomeric bands were assigned to $^{113,115}\text{Pd}$ based on the relatively smooth dependence of Te mass with increasing Pd mass. The spins were assigned assuming that the transitions are $\Delta J=2$ as for a decoupled band, following the systematics in the lighter odd Pd isotopes. These isomer bands are actually yrast, so they are expected to be strongly populated in fission. The isomer band in ^{113}Pd was observed up to a spin of $\frac{41}{2}$ at 6719 MeV and the band in ^{115}Pd up to a spin of $\frac{35}{2}$ at 4758 MeV. The ordering of the γ rays within the bands were based on the observed intensities of the γ -ray peaks.

5.4 $^{112,114,116}\text{Pd}$

The yrast bands of $^{112,114,116}\text{Pd}$ were previously identified to spins of $10\hbar$, $12\hbar$, and $12\hbar$, respectively, in thick source experiments observing γ rays from spontaneous fission of ^{252}Cf [64]. The level diagrams were extended to ground band spins of $14\hbar$, $16\hbar$, and $16\hbar$, with the addition of γ vibrational-like bands up to spins $8\hbar$, $11\hbar$, $11\hbar$, respectively, and negative parity bands were observed in ^{114}Pd up to spin $15\hbar$ and up to spin $13\hbar$ in ^{116}Pd [42].

The level diagrams for $^{112,114,116}\text{Pd}$ based on this work agree with those of [64, 42] with one exception and a few additions. In ^{112}Pd the $14^+ \rightarrow 12^+$ transition is assigned an energy of 724 instead of 606.7 keV, and the yrast bands are extended to spin $20\hbar$ in these three nuclei. A probable negative parity band for ^{112}Pd also is reported.

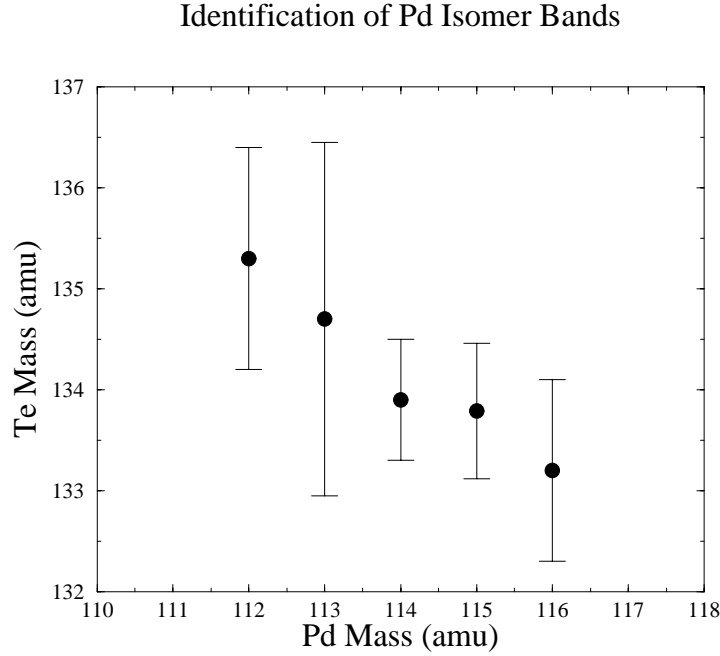


Figure 5.6: The average masses of the Te fission partners calculated from the $2^+ \rightarrow 0^+$ Te transitions in coincidence with the Pd. This was used to identify the mass number of the isomeric Pd bands.

The moments of inertia calculated from the transition energies for $^{112,114,116}\text{Pd}$ are shown in Fig. 5.7. The most notable features of these moments of inertia are the nearly identical nature and also a second band crossing observed in ^{116}Pd .

5.5 $^{111,113}\text{Rh}$

The level diagrams (Figures 5.11, 5.12) for $^{111,113}\text{Rh}$ were developed using the thick source data and extended to higher spins with the thin source data [72]. The transitions in the Rh were identified based on their coincidence with transitions in their fission partners, the isotopes of iodine, and with levels seen in β decay of ^{112}Ru [43]. The levels are ordered from γ -ray intensity and coincidence considerations. The adopted ground state spins of $^{111,113}\text{Rh}$ are $\frac{7}{2}^+$, based on the systematics of the odd Rh nuclei [66, 65], and the ground state band spins and parities were assigned assuming the systematics of coupled $\Delta I=2$ bands. The ground band of ^{111}Rh was observed

Even Pd Backbends

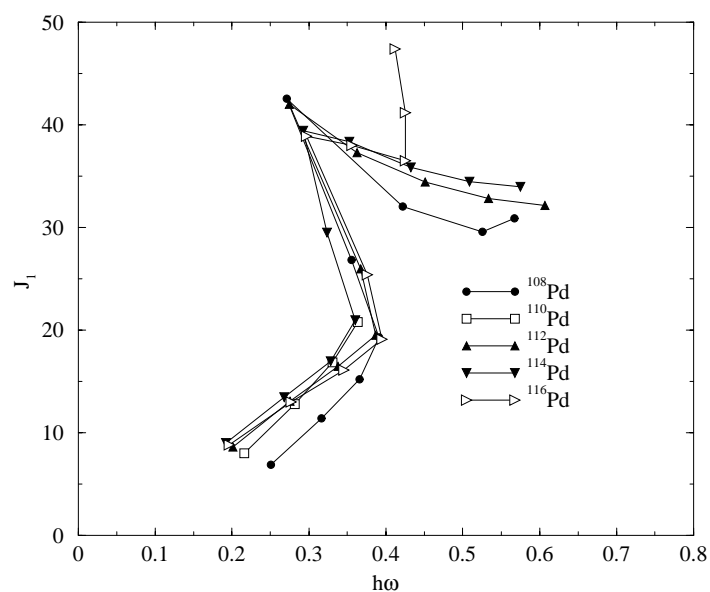
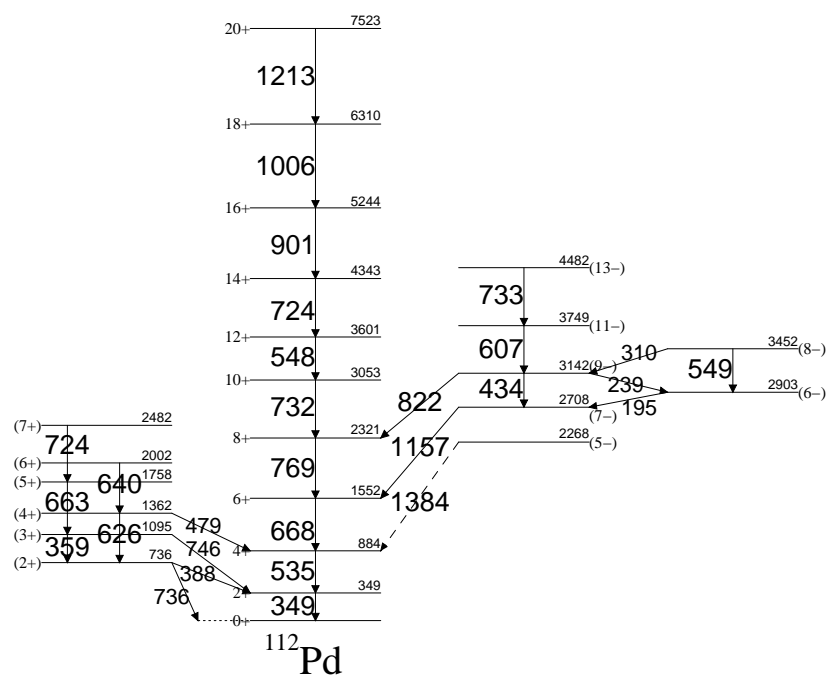
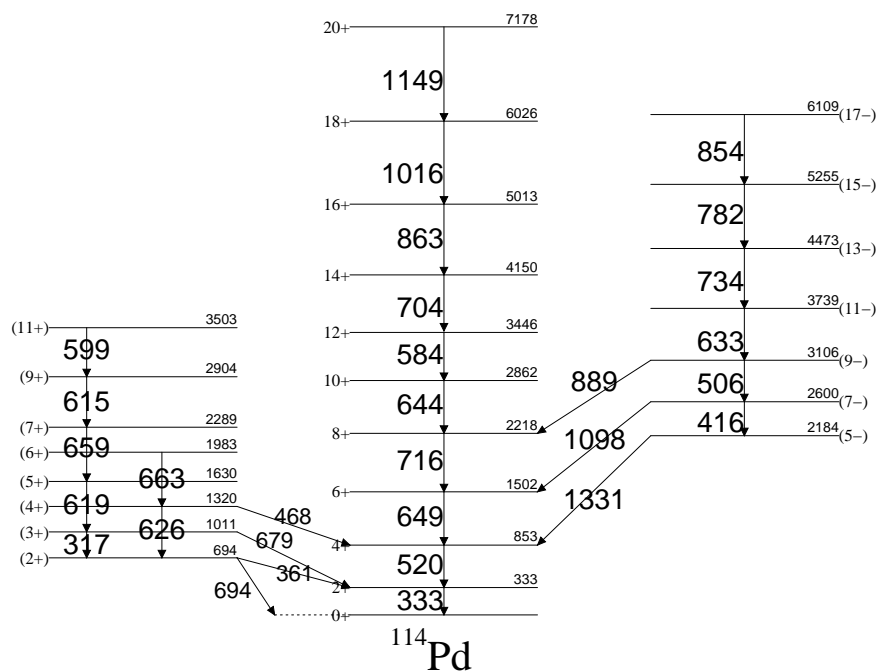
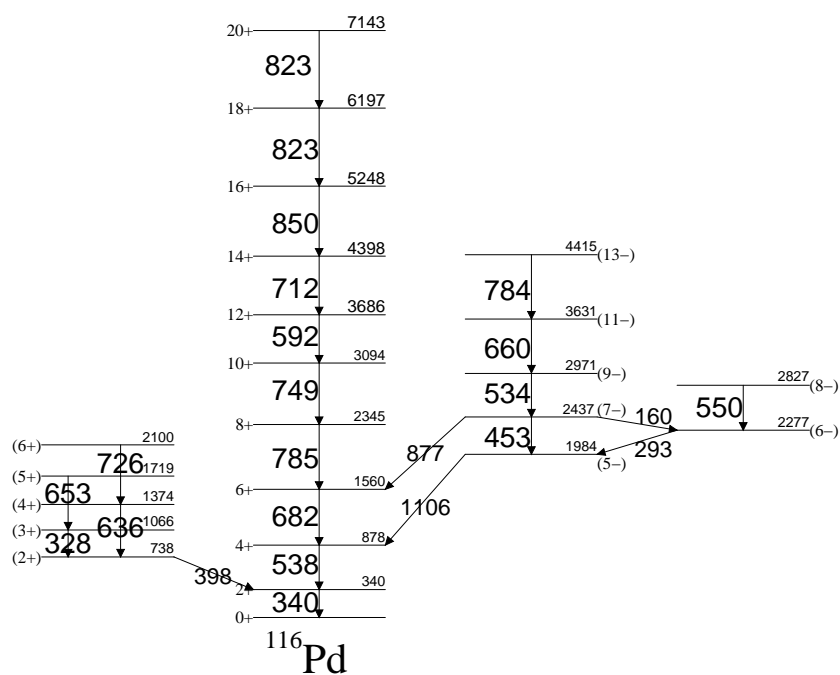


Figure 5.7: Even Pd band crossings

Figure 5.8: ^{112}Pd level diagram

Figure 5.9: ^{114}Pd level diagramFigure 5.10: ^{116}Pd level diagram

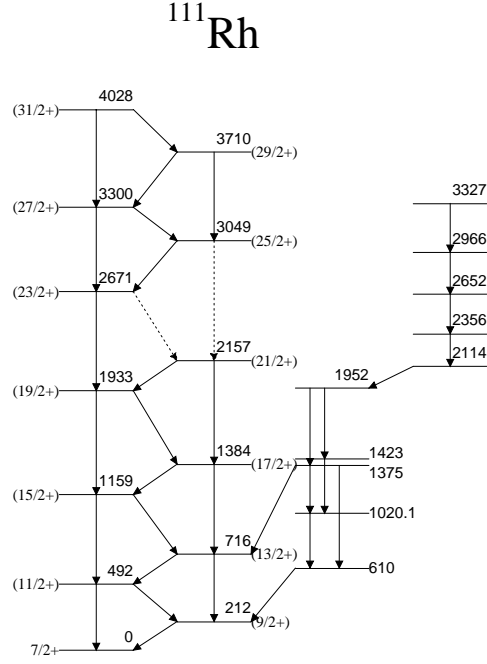


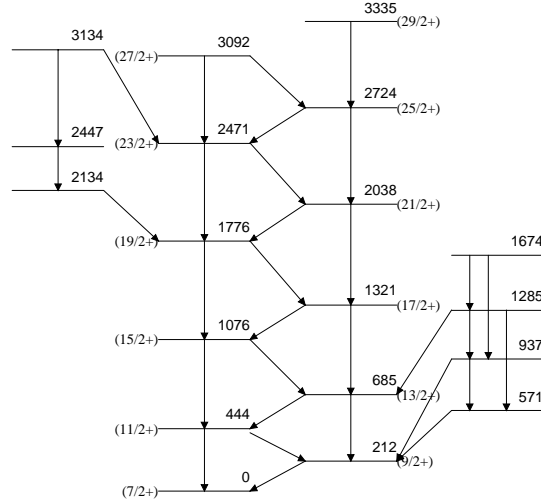
Figure 5.11: ^{111}Rh level diagram [72]

up to a spin of $\frac{31}{2}^+$ and an energy of 4028 keV, and the ground band of ^{113}Rh was observed up to a spin of $\frac{29}{2}^+$ and an energy of 3335 keV.

The odd A nuclei $^{111,113}\text{Rh}$, with a nuclear charge of 45, have one proton less than the neighboring even-even $^{112,114}\text{Pd}$.

5.6 Discussion

Model independent information about nuclear shapes can be obtained from the electric and magnetic transition matrix elements, which can be measured, for instance by Coulomb excitation. However, in the regions of nuclides where the half lives are too short to produce suitable targets, and where radioactive beams of sufficient intensity have not yet been developed to perform such experiments, less direct evidence can be used to provide information on the nuclear shape. The ordering and behavior of the Nilsson orbitals of the nuclear core at high spins is sensitive to the nuclear deformation, especially for the contrast between prolate or oblate shapes. Hence

¹¹³RhFigure 5.12: ¹¹³Rh level diagram [72]

identification of the orbitals which are occupied by the valence protons and neutrons can provide model dependent information about the nuclear shape.

Identification of the orbitals responsible for the observed band crossings in ^{112,114,116}Pd, whether the $\pi(g_{\frac{9}{2}}^2)$ or $\nu(h_{\frac{11}{2}}^2)$ -pair are aligned, can answer the question of whether these nuclei are still prolate or have changed to oblate deformation as predicted by theoretical models [56, 54]. Preliminary HFB cranked shell model calculations for proton and neutrons levels in ¹¹⁶Pd for both prolate and oblate shapes are shown in Figures 5.13, 5.14, 5.15, 5.16. The deformations used in these calculations are from the calculated oblate and prolate minima for ¹¹⁶Pd in Ref. [54]. The predicted frequency for the $\nu(h_{\frac{11}{2}}^2)$ alignment is about 0.4 MeV/ \hbar for both prolate and oblate shapes. The calculated proton alignments, however, are significantly different for oblate or prolate shapes, with the alignments occurring at frequencies of about 0.28 MeV/ \hbar or 0.48 MeV/ \hbar respectively. These frequencies are either below or above the expected neutron alignments, so if the nature of the first observed band crossings can be deduced from the experimental data, this would suggest either oblate or prolate

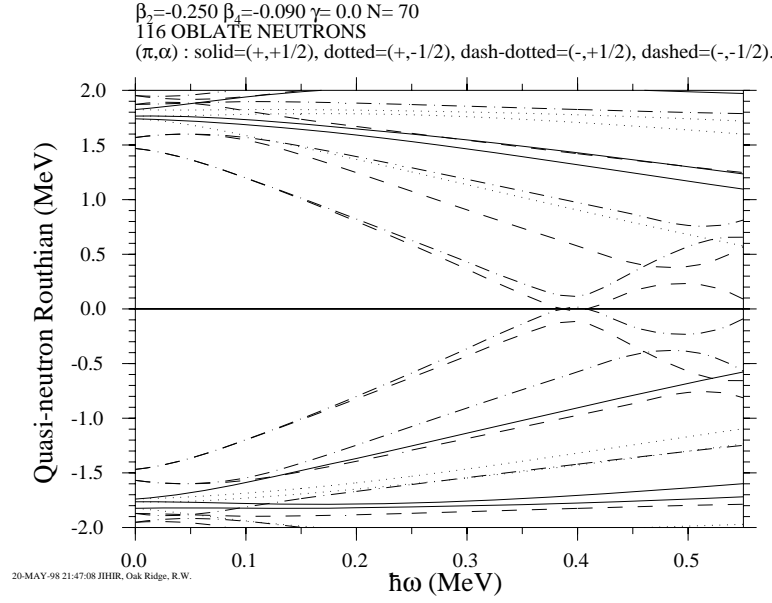


Figure 5.13: ^{116}Pd single particle routhians for neutrons in an oblate shape.

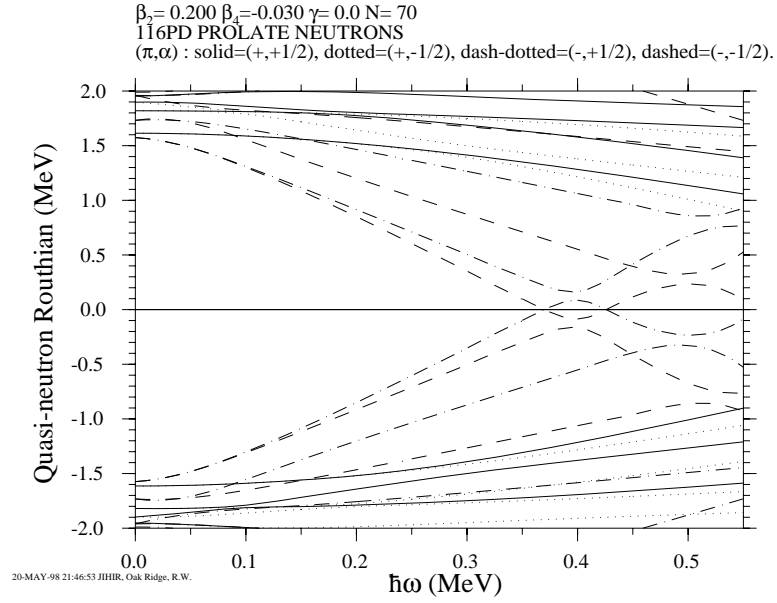


Figure 5.14: ^{116}Pd single particle routhians for neutrons in an prolate shape.

shapes for $^{112,114,116}\text{Pd}$.

Information about the orbitals responsible for the observed band crossings can be derived from aligned angular momentum. The adopted g -reference [63], with Harris parameters of $\mathcal{J}_0 = 18.9\hbar/\text{MeV}$ and $\mathcal{J}_1 = 12.3\hbar^2/\text{MeV}^2$, giving a constant alignment for

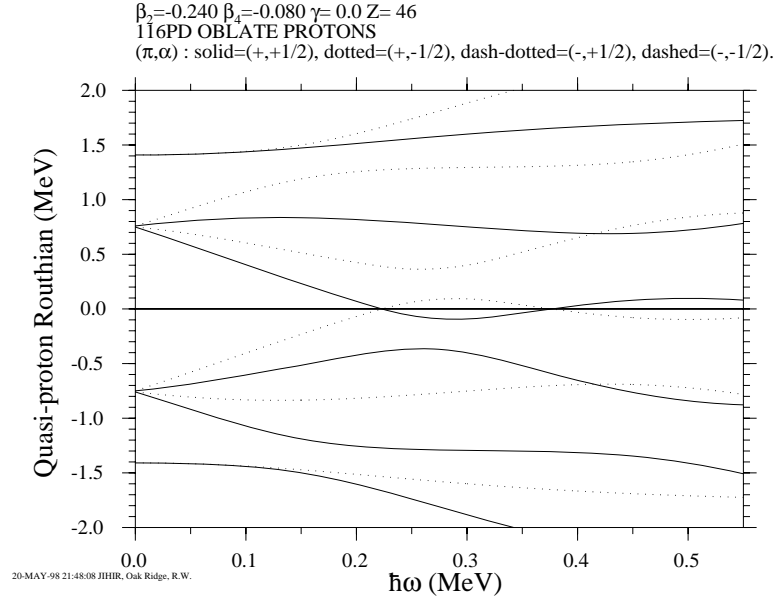


Figure 5.15: ^{116}Pd single particle routhians for protons in an oblate shape.

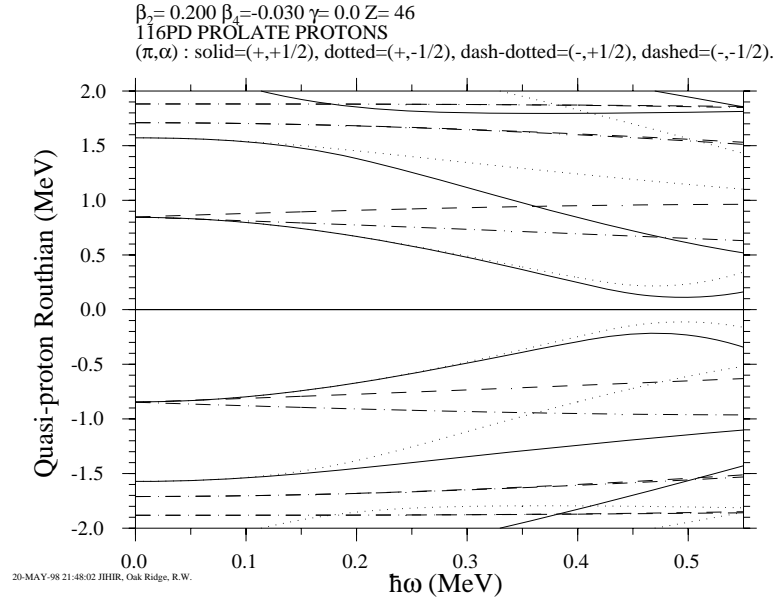


Figure 5.16: ^{116}Pd single particle routhians for protons in a prolate shape.

the S band of ^{114}Pd , was used in the calculation of the aligned angular momentum, i_x , in Figures 5.17, 5.18, 5.19. The similarity of the band crossings through this region (see Figure 5.7) justify the use of the same parameters for all these nuclei. The highest j orbitals for the valence neutrons and protons, $\nu h \frac{11}{2}$ and $\pi g \frac{9}{2}$ respectively, are the

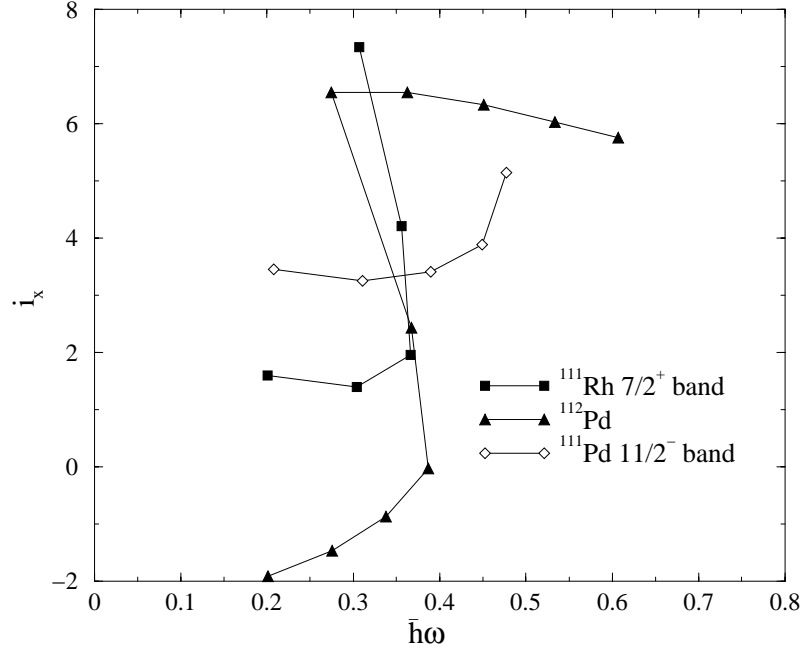


Figure 5.17: The aligned angular momentum of the ground bands of ^{111}Rh and ^{112}Pd and the $\frac{11}{2}^-$ isomer band in ^{111}Pd [59].

likely candidates for causing the observed alignments since these are the most sensitive to the Coriolis interaction. The maximal aligned angular momentum a $\nu(h\frac{11}{2})^2$ -pair can contribute is $10\hbar$ and the maximum alignment a $\pi(g\frac{9}{2})^2$ -pair can contribute is $8\hbar$. The amount of angular momentum aligned in $^{112,114,116}\text{Pd}$ (see Figs. 5.17, 5.18, 5.19) is close to $8\hbar$, which does not conclusively rule out this being a $\pi(g\frac{9}{2})^2$ alignment. Thus blocking arguments must be used to identify the aligning orbital.

The band crossing in ^{112}Pd was identified to originate from a $\nu(h\frac{11}{2})^2$ -pair based on the observation that frequency at which the alignment of the $\nu h\frac{11}{2}$ isomer band in ^{111}Pd is delayed with respect to ^{112}Pd [59]. This observation is confirmed by the behavior of the rotational band in ^{111}Rh , shown in Figure 5.17. A band crossing is observed occurring at the same rotational frequency as the band crossing in ^{112}Pd , implying that the unpaired valence proton occupying the $g\frac{9}{2}$ orbital in the ground state of ^{111}Rh acts as a spectator and does not block the alignment, hence the possibility of the alignment in ^{112}Pd being caused by a $\pi(g\frac{9}{2})^2$ -pair is excluded.

The behavior of the rotational bands in ^{113}Pd and ^{113}Rh confirm that the band

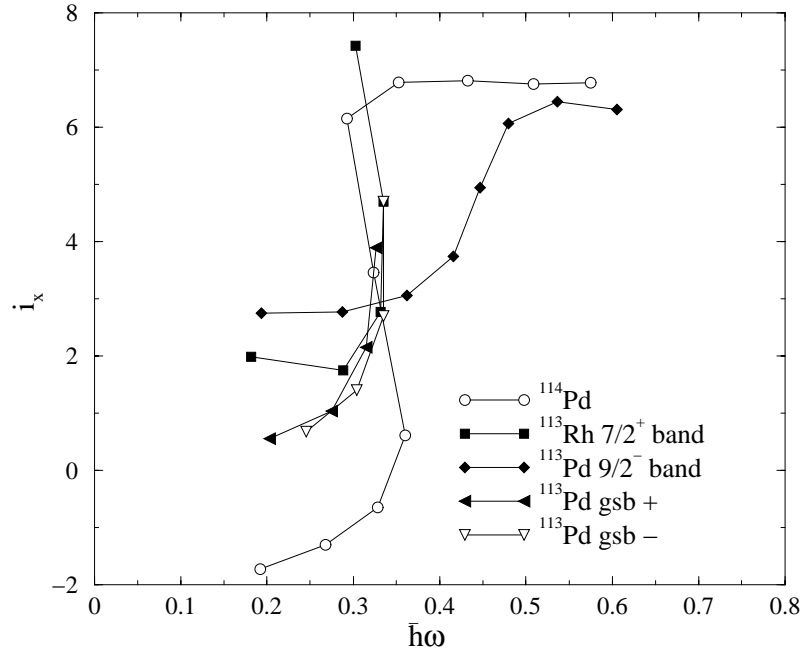


Figure 5.18: The aligned angular momentum of the ground bands in ^{113}Rh , ^{113}Pd , and ^{114}Pd , and the $\frac{9}{2}^-$ isomer band in ^{113}Pd .

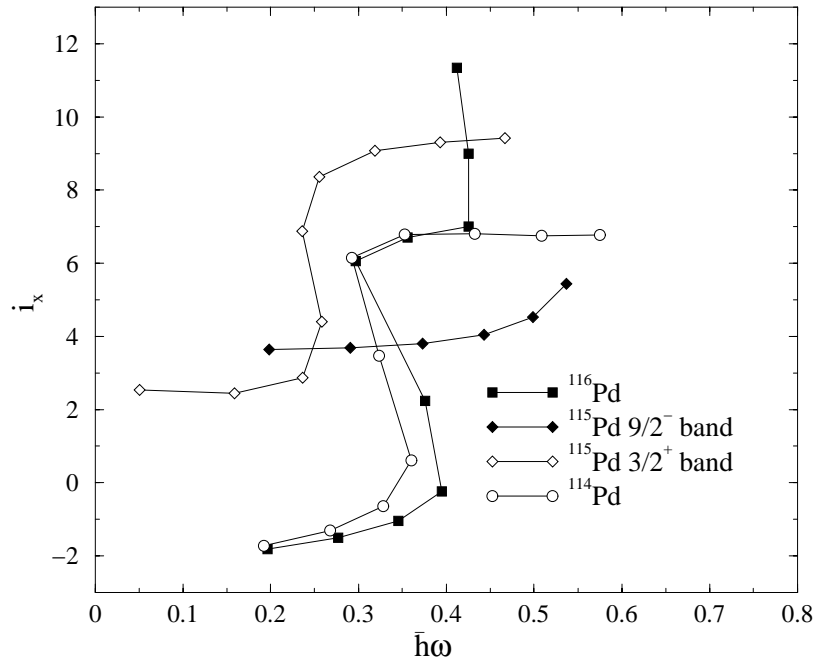


Figure 5.19: The aligned angular momentum of the ground bands of $^{114,115,116}\text{Pd}$ and the $\frac{9}{2}^-$ isomer band in ^{115}Pd .

crossing observed in ^{114}Pd also is caused by the alignment of a $\nu(h\frac{11}{2})^2$ -pair. The aligned angular momentum for $^{113,114}\text{Pd}$ and ^{113}Rh are shown in Figure 5.18. In ^{113}Pd the frequency of the band crossing in the isomer band built on the $\nu h\frac{11}{2}$ orbital is delayed by the unpaired valence neutron from about $0.3 \text{ MeV}/\hbar$ to $0.45 \text{ MeV}/\hbar$. For the rotational structures built on the ground state (which is a mixture of $\nu d\frac{5}{2}$ and $\nu g\frac{7}{2}$), the crossing frequency $0.3 \text{ MeV}/\hbar$ is not delayed. Here the unpaired neutron is in an orbital which does not effect the $\nu(h\frac{11}{2})^2$ -pair alignment. In ^{113}Rh the presence of the unpaired valence proton in the $g\frac{9}{2}$ orbital does not block the band crossing from occurring either, which is consistent with the conclusion that the band crossing in ^{114}Pd is from a $\nu(h\frac{11}{2})^2$ pair.

The suggestion posed that the isomeric levels in the odd-A Pd have prolate shapes while the ground band shapes are oblate, based on the large hindrances of the isomeric decays [61], makes blocking arguments based only on the odd-A Pd bands inconclusive. If the ground state shapes of $^{112,114,116}\text{Pd}$ and $^{113,115}\text{Pd}$ were oblate, the observed alignment in the ground state bands of these nuclei would be caused by a $\pi(g\frac{9}{2})^2$ -pair, and comparison with the isomeric $\nu h\frac{11}{2}$ bands would be incorrect. The blocking arguments presented here are supported by the observation that the unpaired $g\frac{9}{2}$ proton in $^{111,113}\text{Rh}$ do not delay the alignments of their ground bands.

The aligned angular momentum for the ground band of ^{116}Pd and the ground and isomer band of ^{115}Pd is shown in Fig. 5.19. The same arguments used for the identification of the orbits responsible for the band crossing in ^{114}Pd , based on the behavior of the bands in ^{113}Pd , can be used for ^{116}Pd and ^{115}Pd . The $\nu h\frac{11}{2}$ isomer band in ^{115}Pd blocks the band crossing while the ground band configuration does not. The crossing frequencies in ^{115}Pd of both the ground band and isomer band are different than the lighter Pd and Rh. The isomer band delays the neutron pair alignment to a rotational frequency of about $0.55 \text{ MeV}/\hbar$, compared to $0.45 \text{ MeV}/\hbar$ in $^{111,113}\text{Pd}$. The alignment of the ground band alignment in ^{115}Pd occurs at about $0.22 \text{ MeV}/\hbar$, well below the crossing frequency observed in the ground bands of $^{111,113}\text{Rh}$, $^{112,113,114,116}\text{Pd}$.

5.7 Summary

New levels in the neutron-rich Pd and Rh were observed in the prompt spectroscopy of fission products of $^{252}\text{Cf}(\text{SF})$. Rotational bands based on the ground state configuration and on the $\frac{9}{2}^-$ or $\frac{11}{2}^-$ isomeric levels were identified in $^{113,115}\text{Pd}$. The ground state bands of $^{112,114,116}\text{Pd}$ each were extended to spins of $20\hbar$. A second band crossing in ^{116}Pd and a negative parity band in ^{112}Pd , similar to bands in $^{114,116}\text{Pd}$, were observed. Rotational bands built on the ground state configurations of $^{111,113}\text{Rh}$ also also identified.

The behavior of the moment of inertia of these rotational bands identify the orbitals responsible for the alignments observed in the yrast bands of $^{112,114,116}\text{Pd}$. The band crossings in the isomeric bands of $^{113,115}\text{Pd}$ based on the $\nu h\frac{11}{2}$ orbital are delayed compared to the band crossings of the neighboring ^{114}Pd and ^{116}Pd , suggesting a $\nu(h\frac{11}{2})^2$ character for these even Pd band crossings. The ground bands of $^{113,115}\text{Pd}$, built on different ν configurations, and the odd-proton configuration of $^{111,113}\text{Rh}$ exhibit band crossings at the same frequency as the even Pd. The Rh results confirm that the band crossings are not caused by the alignment of a $\pi(g\frac{9}{2})^2$ -pair. Comparison to cranked shell model calculations suggest that since the aligning nuclei are $\nu(h\frac{11}{2})^2$ the nuclear shapes for the even Pd are prolate, and the predicted shape transition from prolate to oblate has not yet occurred up to ^{116}Pd .

Chapter 6

Lifetime measurement of ^{135}I

The study of the nuclei near double shell closures is of fundamental interest since the single particle structures in these regions are expected to be relatively pure configurations. The experimentally measured properties of the single particle structures of the valence nuclei, where a few particles or holes are coupled to a double closed shell core, give information on the basic single particle matrix elements and interaction between the pairs of nucleons in valence orbitals [74]. There are few double shell closures for heavy nuclei with $A > 56$. The region around ^{208}Pb is the most accessible experimentally, since it lies within the valley of β -stability, and has been well studied. The other double closed shell regions, around ^{78}Ni , ^{100}Sn , and ^{132}Sn , are more difficult to study since they lie away from β -stability. The nuclei in the ^{132}Sn region are populated in fission of actinide nuclei and have been studied via β -decay and by prompt spectroscopy of fission fragments.

With the development of new experimental techniques for producing and studying neutron-rich nuclei, the double closed shell region around ^{132}Sn is being opened for study. The application of the technique using powerful γ -ray arrays for the prompt spectroscopy of spontaneous-fission (SF) products extends the possibilities for the study of the single particle structures in this interesting region, beyond what is possible from the study of β -decay products. Recent work analyzing ^{248}Cm fission includes a study of the $N=83$ isotones [75], the identification of the $\nu(f_{7/2})^2$ multiplet in ^{134}Sn [76], and identification of single particle structure of ^{134}Te and ^{135}I with

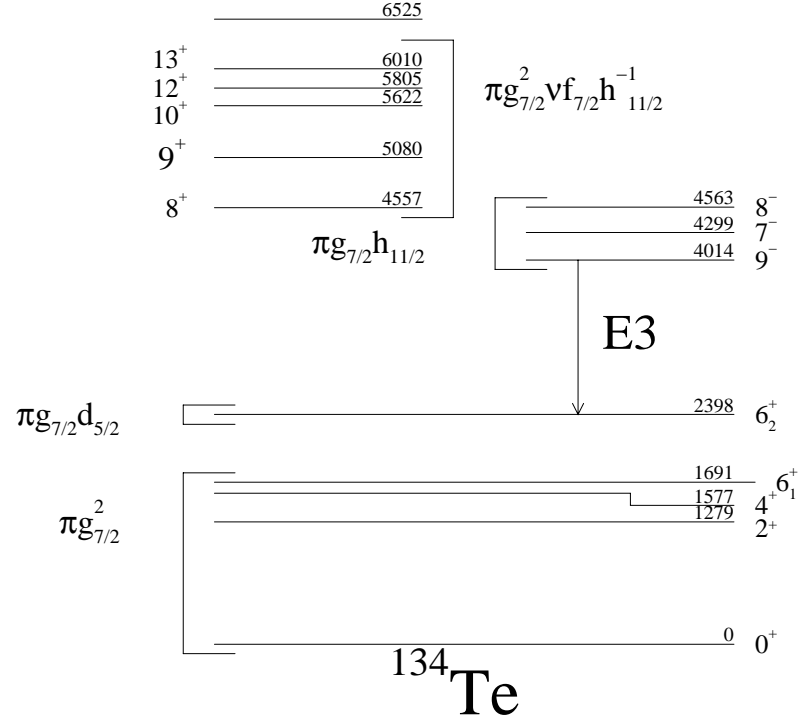
supporting shell model calculations.

As more is learned about spectroscopy of the nuclei in the ^{132}Sn region [77], and as experimental techniques are refined to measure more lifetimes in this region [78], it is possible to extract single shell and transition matrix elements. Predictions based on these matrix elements can be made for lifetimes of transitions which have not yet been measured. In this chapter the lifetime of the $\frac{23}{2}^-$ level in ^{135}I is estimated based on the single-particle matrix elements extracted from previous measurements in ^{134}Te , and is compared to a lifetime measurement from the thin source fission data.

6.1 Matrix Elements from ^{134}Te

The nucleus ^{134}Te has two valence protons outside a ^{132}Sn core. The yrast excited states of ^{134}Te , shown in the level diagram in Figure 6.1, have been interpreted to be single particle structures [77]. Levels based on proton configurations include 2^+ , 4^+ , 6^+ levels belonging to a $\pi(g_{\frac{7}{2}})^2$ multiplet, a 6_2^+ level belonging to a $[g_{\frac{7}{2}} \times d_{\frac{5}{2}}]$ multiplet, and 7^- , 8^- , and 9^- levels belonging to a $[g_{\frac{7}{2}} \times h_{\frac{11}{2}}]$ multiplet. Higher lying single particle structures involve excitation of the ^{132}Sn core.

The lifetimes of the 6_1^+ and 4^+ members of the $g_{\frac{7}{2}}^2$ multiplet, and the 9^- level have been measured in the β -decay of ^{134}Sb [78]. Assuming a pure $(g_{\frac{7}{2}}^2)^2$ configuration, the $B(E2)$ values extracted from the 6_1^+ and 4^+ lifetimes can be used to determine the one-body matrix element $\langle g_{\frac{7}{2}} || E2 || g_{\frac{7}{2}} \rangle$. The 9^- level decays via an $E3$ to the 6_1^+ member of the $g_{\frac{7}{2}}^2$ multiplet and the 6_2^+ member of the $[g_{\frac{7}{2}} \times d_{\frac{5}{2}}]$ multiplet. The $B(E3)$ values for these transitions can be used to extract the $\langle g_{\frac{7}{2}} || E3 || h_{\frac{11}{2}} \rangle$ and $\langle d_{\frac{5}{2}} || E3 || h_{\frac{11}{2}} \rangle$ one-body matrix elements. The calculation of the matrix elements below is carried out assuming that all the wave functions are a pure configurations, which may not be entirely true. For example, in calculations by the authors of Ref. [80], yielding results which reproduce the experimental data well, impure wave functions were used, and the contributions from configurations other than $g_{\frac{7}{2}}^2$ for the ground state were 17% and less than 4% for the other members of the $\pi g_{\frac{7}{2}}^2$ multiplet. The measured $B(E\lambda)$ from Ref. [78] are:

Figure 6.1: ^{134}Te level diagram

$I_i^\pi \rightarrow I_f^\pi$	$B(E2)$ (W.u.) ($e^2\text{fm}^4$)	
$4_1^+ \rightarrow 2_1^+$	4.3	176.8
$6_1^+ \rightarrow 4_1^+$	2.05	84.3

$I_i^\pi \rightarrow I_f^\pi$	$B(E3)$ (W.u.) ($e^2\text{fm}^6$)	
$9_1^- \rightarrow 6_2^+$	8.0	8660.5
$9_1^- \rightarrow 6_1^+$	3.8	4113.7

The γ -ray transition rates between two-particle states can be calculated using the wave functions for a mixed configuration [79]:

$$\psi_{I_i M_i} = \alpha(j^2)_{I_i M_i} + \beta[j \times j_1]_{I_i M_i} + \gamma(j_1^2)_{I_i M_i} \quad (6.1)$$

$$\psi_{I_f M_f} = \tilde{\alpha}(j^2)_{I_f M_f} + \tilde{\beta}[j \times j_1]_{I_f M_f} + \tilde{\gamma}(j_1^2)_{I_f M_f} \quad (6.2)$$

In the case of the $E2$ transitions from the $(g_{\frac{7}{2}})^2$ multiplet, assuming these levels are pure configurations, the coefficients $\beta = \tilde{\beta} = \gamma = \tilde{\gamma} = 0$ and the matrix element

reduces to

$$\langle \psi_{I_f} || T_{\lambda}^{(\xi)} || \psi_{I_i} \rangle = \sqrt{(2I_i + 1)} \sqrt{(2j + 1)} 2 \langle \phi_j || T_{\lambda} || \phi_j \rangle W(jjI_f \lambda; I_i j) \quad (6.3)$$

The transition rate is then given by

$$B(E\lambda; I_i \rightarrow I_f) = \frac{2I_f + 1}{2I_i + 1} \langle \psi_{I_f} || T_{\lambda}^{(\xi)} || \psi_{I_i} \rangle^2 \quad (6.4)$$

$$= 4(2I_f + 1)(2j + 1) \langle \phi_j || T_{\lambda} || \phi_j \rangle^2 W^2(jjI_f \lambda; I_i j) \quad (6.5)$$

and from this the single shell matrix element $\langle g_{\frac{7}{2}} || E2 || g_{\frac{7}{2}} \rangle$ can be calculated giving

$I_i^{\pi} \rightarrow I_f^{\pi}$	$\langle g_{\frac{7}{2}} E2 g_{\frac{7}{2}} \rangle (efm^2)$
$4_1^+ \rightarrow 2_1^+$	14.88
$6_1^+ \rightarrow 4_1^+$	15.23

The same procedure can now be applied to extract the shell model matrix element $\langle g_{\frac{7}{2}} || E3 || h_{\frac{11}{2}} \rangle$ from the $9_1^- \rightarrow 6_1^+$ transition. In this case the disappearing coefficients in (6.1) are $\alpha = \gamma = 0$ for ψ_{I_i} and $\tilde{\beta} = \tilde{\gamma} = 0$ for ψ_{I_f} and the transition matrix element is given by

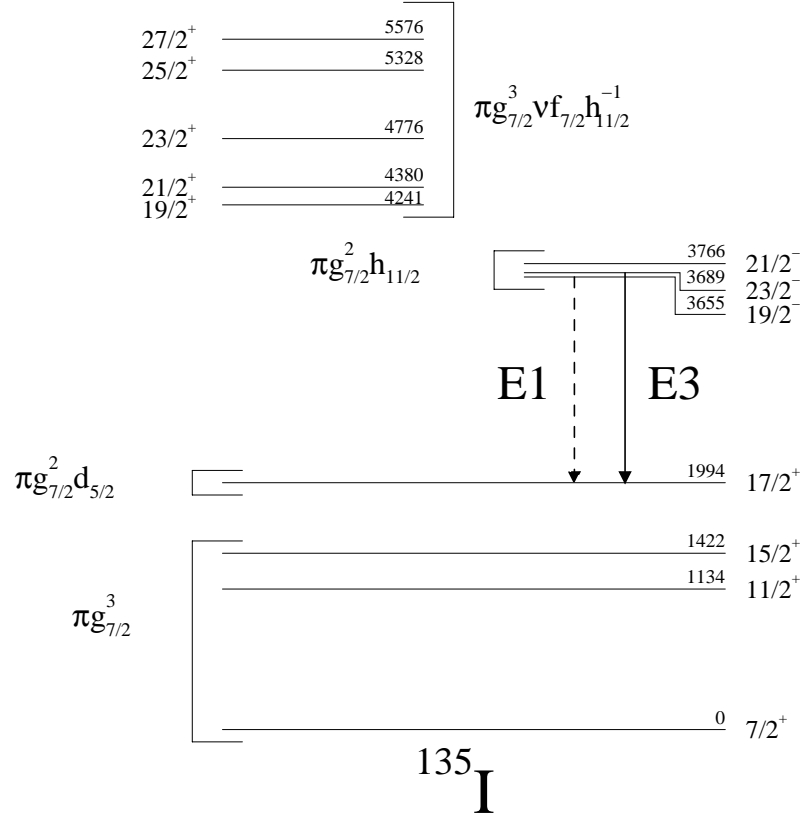
$$\begin{aligned} \langle \psi_{I_f} || T_{\lambda}^{(\xi)} || \psi_{I_i} \rangle &= \sqrt{(2I_i + 1)} \sqrt{2} \sqrt{(2j + 1)} \langle \phi_j || E3 || \phi_{j_1} \rangle \\ &\quad * W(jj_1 I_f \lambda; I_i j) \end{aligned} \quad (6.6)$$

$$\begin{aligned} \langle \psi_{9_1^-} || E3 || \psi_{6_1^+} \rangle &= \sqrt{19 \cdot 2 \cdot 8} \langle g_{\frac{7}{2}} || E3 || h_{\frac{11}{2}} \rangle (.03846154) \\ &= .6706 \langle g_{\frac{7}{2}} || E3 || h_{\frac{11}{2}} \rangle \end{aligned} \quad (6.7)$$

$$\boxed{\langle g_{\frac{7}{2}} || E3 || h_{\frac{11}{2}} \rangle = 127.7 \text{ efm}^3} \quad (6.8)$$

The matrix element governing the $E3$ transition $9_1^- \rightarrow 6_2^+$ transition is $\langle [g_{\frac{7}{2}} \times d_{\frac{5}{2}}]_{6^+} || E3 || [g_{\frac{7}{2}} \times h_{\frac{11}{2}}]_{9^-} \rangle$. The transition occurring is a proton moving from the $h_{\frac{11}{2}}$ to the $d_{\frac{5}{2}}$ orbital. The $\langle d_{\frac{5}{2}} || E3 || h_{\frac{11}{2}} \rangle$ matrix element can be extracted by re-coupling the components of the initial and final wave functions.

$$\left[E3 \left[g_{\frac{7}{2}} \times h_{\frac{11}{2}} \right]_9 \right]_6 = g \begin{array}{|c|} \hline \begin{array}{c} h \\ 9 \end{array} \\ \hline \lambda \\ \hline 6 \end{array} = 3$$

Figure 6.2: ^{135}I level diagram

$$\begin{aligned}
 &= \sum_{\epsilon} \sqrt{(2 \cdot \frac{23}{2} + 1)} \sqrt{(2 \cdot \epsilon + 1)} W(6 \frac{11}{2} \frac{17}{2} 3 : \frac{23}{2} \epsilon) \begin{array}{c} h \\ \begin{array}{|c|} \hline \begin{array}{c} g \\ 6 \\ g \end{array} \\ \hline \end{array} \\ \frac{17}{2} \end{array} \lambda \\
 &\langle [g^2 \times d]_{\frac{17}{2}+} || E3 || [g^2 \times h]_{\frac{23}{2}-} \rangle = \sqrt{24 \cdot 6} W(6 \frac{11}{2} \frac{17}{2} 3 : \frac{23}{2} \frac{5}{2}) \langle d_{\frac{5}{2}} || E3 || h_{\frac{11}{2}} \rangle \\
 &B(E3; (g_{\frac{7}{2}}^2 h_{\frac{11}{2}})_{\frac{23}{2}-} \rightarrow (g_{\frac{7}{2}}^2 d_{\frac{5}{2}})_{\frac{17}{2}+}) = \frac{18}{24} \times .6667 \langle d_{\frac{5}{2}} || E3 || h_{\frac{11}{2}} \rangle^2 \\
 &= 8659 \text{ e}^2 \text{fm}^6 \tag{6.12}
 \end{aligned}$$

The transition energy is 1695 keV, so the partial width can be calculated to be $\Gamma = 1.3076 \cdot 10^{-7} \text{ eV}$. Assuming no other decay routes for the $\frac{23}{2}^-$ level, and pure

configurations, the upper bound for this lifetime is:

$$\boxed{\tau = 5.03 \text{ ns}} \quad (6.13)$$

6.3 Measurement of the $\frac{23}{2}^-$ level lifetime in ^{135}I

The possibility of measuring the lifetime of the $\frac{23}{2}^-$ level in ^{135}I is suggested from the comparison of the thick source and thin source data. The γ -ray spectra from these two data sets, with the same summed gates applied on the $\frac{17}{2}^+ \rightarrow \frac{15}{2}^+$, $\frac{15}{2}^+ \rightarrow \frac{11}{2}^+$, and $\frac{11}{2}^+ \rightarrow \frac{7}{2}^+$ transitions in ^{135}I , are shown in Figure 6.3. The spectrum in Figure 6.3a was obtained from the “prompt” γ -rays, that is the Doppler correction was applied, so only the γ -rays emitted in-flight before the nuclei reach the PPACs are recovered. The observed intensity of 1695 keV $E3$ transition de-exciting the $\frac{23}{2}^-$ relative to the 1661 keV $E1$ transition de-populating the $\frac{19}{2}^-$ level in the thin source data is 44% that of the thick source. The $E1$ can be used to normalize the $E3$ intensity for comparison of the thick and thin source data. Transitions with $E1$ multipolarity are faster than transitions with $E3$ multipolarity, and hence, the intensity of the $E1$ transition should include all of the population of the $\frac{19}{2}^-$ level. The lower $E3/E1$ intensity ratio in the thin source data suggests that the lifetime of the $E3$ transition might be long enough that a significant fraction of the decay occurs after the nuclei implant in the PPACs, which occurs after a calculated average time-of-flight of 12.6 ns. The intensities of the prompt and delayed peaks can be used to measure the lifetime of the level.

The “delayed” component of the $E3$ decay, that which decays after the nuclei implant in the PPACs, was searched for in the thin source data by sorting the γ rays, without applying any Doppler correction, into a three-dimensional histogram. The resultant gated spectra should give sharp γ -ray peaks for transitions occurring after the nuclei stop in the PPACs. The “delayed” intensity of the $E3$ transition was then obtained by applying the same gates as were applied as in generation of the prompt ^{135}I spectra. There was no γ -ray peak observed at the expected energy of 1695 keV, but an upper limit on the intensity was obtained by a fit at the expected location.

There is an apparent discrepancy in the intensity of the $E3$ transition comparing

the thick and thin source data. The ratio of the total (prompt plus delayed) $E3$ intensity to $E1$ intensity in the thin source data is less than in the thick source data. Possible explanations for the difference in observed ratios are efficiency and line shape considerations. The reduced $E3$ intensity in the thin source could result from a decrease in peak-efficiency of GAMMASPHERE as the nuclei recoil from the source. To check this possibility the peak-efficiency was simulated with the Monte Carlo code GEANT [81] (Figure. 6.4). The simulation was performed for a 1695 keV γ ray emitted at 0.0, 6.4, and 12.8 cm from the center of GAMMASPHERE. The simulation was performed without the CHICO detector, but the relative efficiencies are expected to be similar (see Section 3.3.7). The peak-efficiency is shown to remain relatively flat over the flight path of the nuclei. Other possible reasons for the discrepancy between the two data sets are related to the γ -ray line shapes. In the thin source data the angle between the γ -ray direction and recoil direction, used in calculating the Doppler correction, assumes the nucleus is at the center of GAMMASPHERE. As the nucleus travels from the source this angle is no longer correct, and the resultant γ -ray peak after the Doppler correction would broaden. It is also possible that the $E1$ transition in the thick source has a component which is broadened due to the stopping time of the recoiling fragment in the source resulting in a reduction in the observed $E1$ intensity. The broadening of the line shapes could result in lost intensity in the gated spectra.

Since the differences in the $E3$ intensity between the thick source and thin source data are not well quantified, the lifetime of the $E3$ transition was estimated using the thin source data alone. The measured prompt and delayed intensities, I_p and I_d , respectively, can give the lifetime, τ , through the relation

$$\exp\left(\frac{-t}{\tau}\right) = \frac{I_d}{I_p + I_d} \quad (6.14)$$

where t is the average time of flight to the PPACs. The lifetime obtained for the $E3$ transition from the thin source experiment is $4.0^{+1.0}_{-2.6}$ ns. The high limit of the measurement, 5.0 ns, is an upper bound on the lifetime since it is possible that some of the intensity of the prompt peak is not observed due to experimental considerations. This value agrees well with the shell model prediction of 5.0 ns calculated

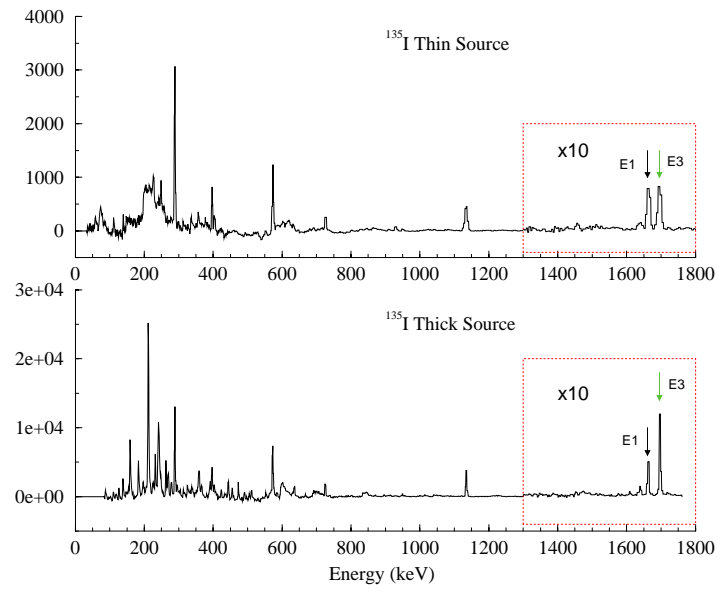
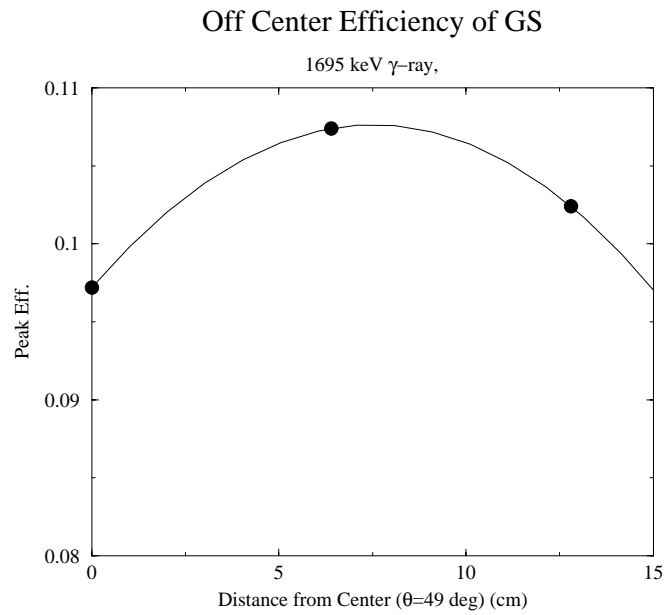
Figure 6.3: ^{135}I spectrum

Figure 6.4: GEANT calculation of the peak-efficiency away from the center of GAM-MA SPHERE [81]

in Section 6.2. Extraction of more quantitative information about this transition, such as collective enhancement of the $E3$ transition rate, requires a more accurate measurement of the lifetime.

Chapter 7

High Spin Results

One of the advantages of performing spectroscopic studies of $^{252}\text{Cf}(\text{SF})$ products with a thin source, as discussed in Section 4.6.4, is the ability to observe levels at higher spins and excitation energies. By performing the Doppler correction on the γ -rays emitted during the flight of the fission products, sharp line shapes can be recovered for γ rays emitted from levels which have lifetime on the order of 1 ps. Extending rotational bands to higher spins allows the ability to study the nuclear structure related properties, such as band crossings and shape properties, at higher excitation energy. The purpose of this chapter is to illustrate the capabilities of this technique by showing the results from a few nuclei.

7.1 ^{112}Ru

The role of tri-axiality in the structure of ^{112}Ru has been discussed recently in the literature[52, 53]. Some of the evidence for tri-axial behavior in this nucleus is the very low lying 2_2^+ state, the γ -ray branching ratios from the γ -band to the ground band, and the staggered spacing of the levels in the γ -band. In the present work the ground band has been extended to $20\hbar$ and γ -band has been extended from spin 10^+ to 17^+ (Figure 7.1), and the strong stagger continues at higher spin indicating that the centroid of the shape parameter γ remains non-zero. To extract a rough value for the γ shape parameter, the level structure of the γ -band was compared

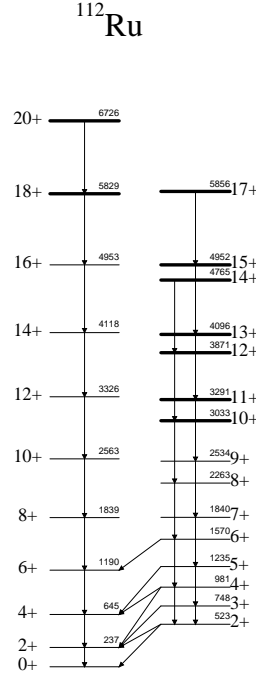


Figure 7.1: Level diagram for ^{112}Ru . New levels added from the present work are shown as thick lines in the level diagram.

to the Rigid Tri-axial Rotor (RTR) model predictions [82]. The RTR model does not include effects such as variable moment of inertia and as a consequence, the predicted energies of the levels are higher than the observed levels. To correct for this in comparing the observed level to the RTR predictions, ratios of differences in energy of levels in the experimental spectra were compared to the same ratios from the RTR model as follows,

$$\left. \frac{E(I+1) - E(I)}{E(I) - E(I-1)} \right|_{RTR} = \left. \frac{E(I+1) - E(I)}{E(I) - E(I-1)} \right|_{expt} \quad (7.1)$$

The γ -value satisfying the equality were extracted. This analysis indicates that the centroid of the γ deformation ranges from 12° to 15° at higher spins, which is reduced from 26.4° given by the RTR model based on the ratio of $2_2^+/2_1^+$ energies (Figure 7.2).

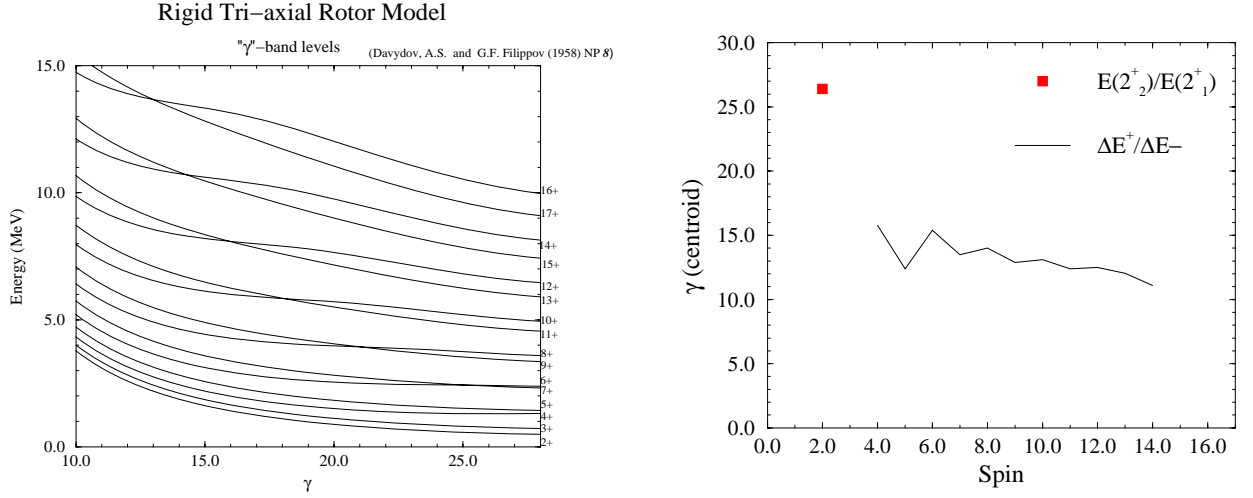


Figure 7.2: The left figure shows the RTR model predictions for the energy levels of the γ -band as a function of the γ shape parameter. The right figure shows the value of the shape parameter γ extracted from the level diagram.

7.2 ^{102,104,106,108}Mo

The neutron-rich nuclei ^{104,108}Mo have been observed in ²⁴⁸Cm(SF) up to spins of 12 \hbar and 10 \hbar , respectively, in the ground band, and to a spin of 10 \hbar in the γ -band of ¹⁰⁴Mo [83]. The ground bands of ^{102,104,106,108}Mo were extended to spins of 12 \hbar , 14 \hbar , 14 \hbar , and 12 \hbar , respectively, by Zhu *et al.* [10]. In the present work the ground band for these nuclei were extended to spins of 14 \hbar , 18 \hbar , 20 \hbar and 18 \hbar , respectively, and the γ -band of ¹⁰⁴Mo was extended to 16 \hbar . Zhu *et al.* noted that there was an indication of a band crossing in ground band of ¹⁰⁴Mo at spin 14 \hbar . By extending this rotational band by three levels the rest of the band crossing region is observed (Figure 7.4). The band crossing also occurs in the odd and even spin sequences of the γ -band (Figure 7.5).

7.3 ^{150,152,154,156}Nd

The ground state rotational bands of the neutron-rich nuclei ^{152,154,156}Nd have been observed to spins of 16 \hbar in the spontaneous fission of ²⁴⁸Cm [40]. ^{150,152,154,156}Nd also

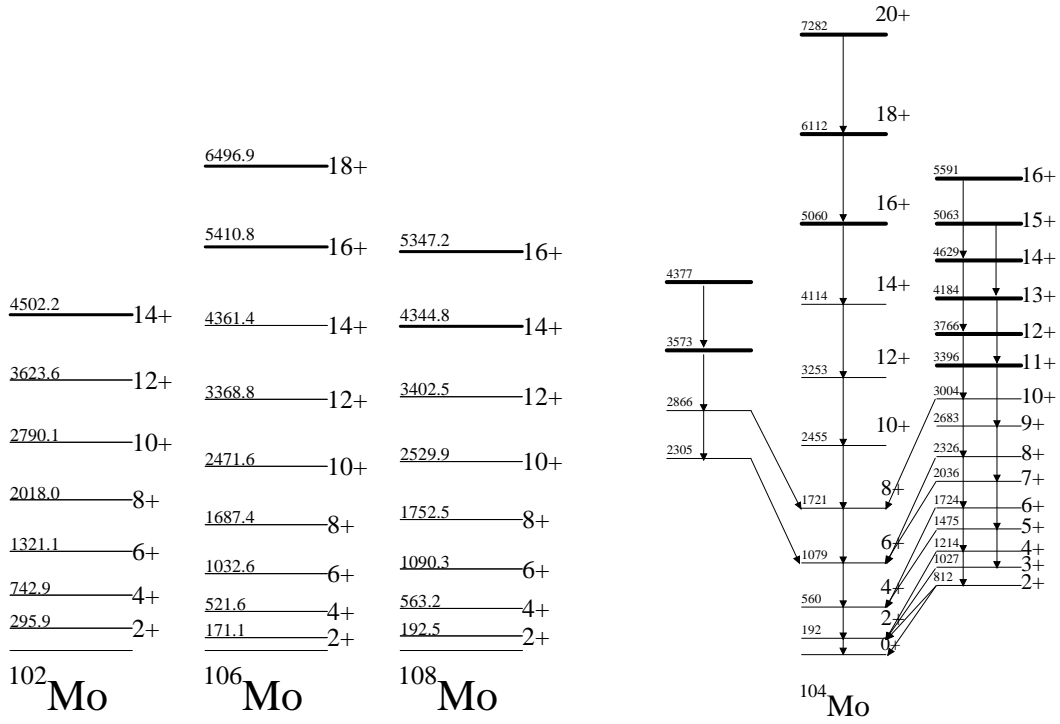


Figure 7.3: Level diagram for $^{102,104,106,108}\text{Mo}$. New levels observed in the present work are shown as thick lines.

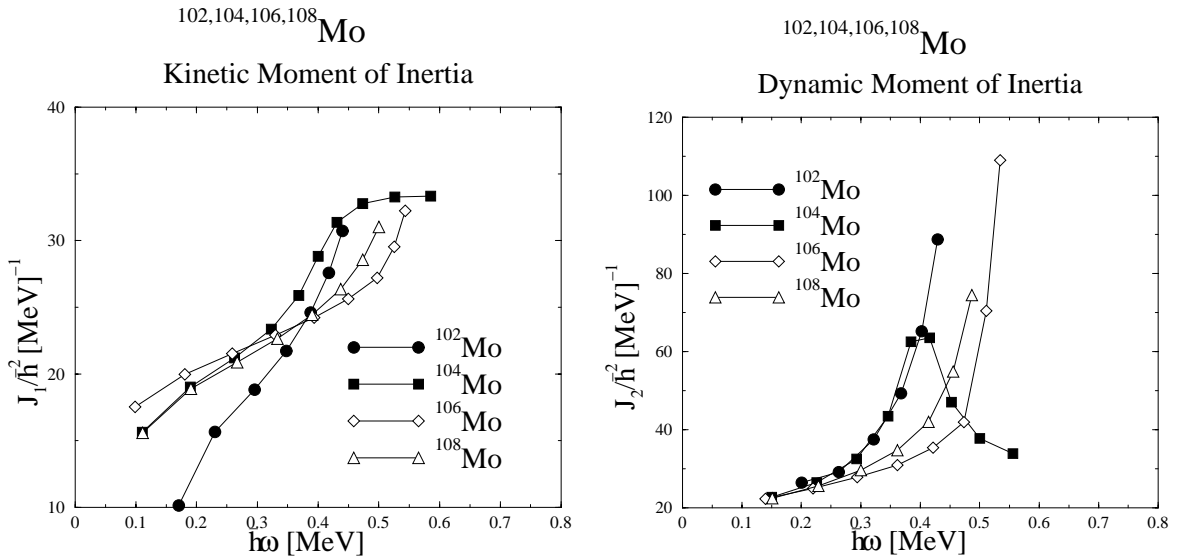


Figure 7.4: Kinetic and dynamic moments of inertia for the ground bands of $^{102,104,106,108}\text{Mo}$.

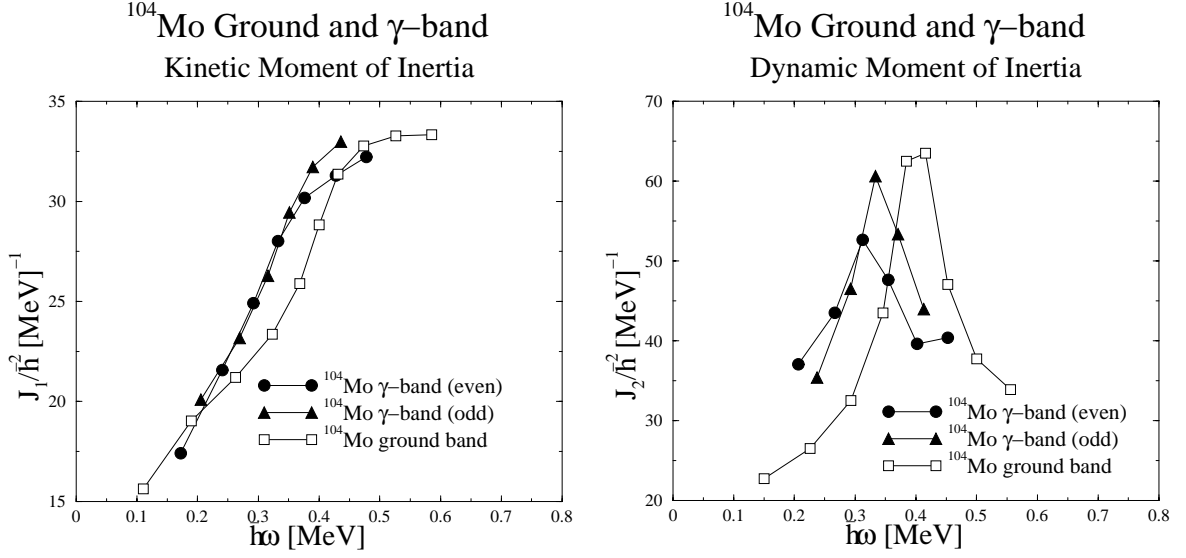
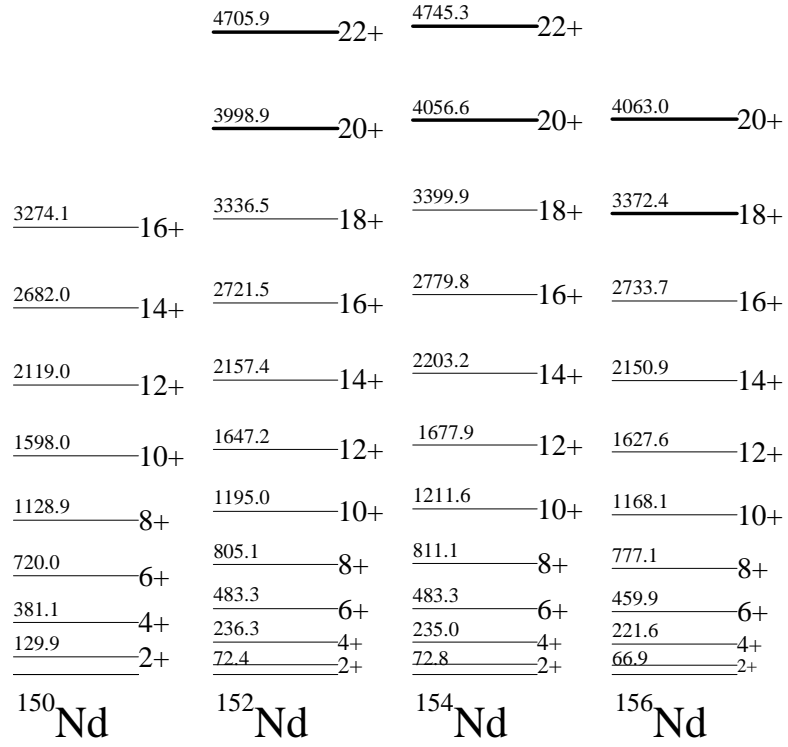
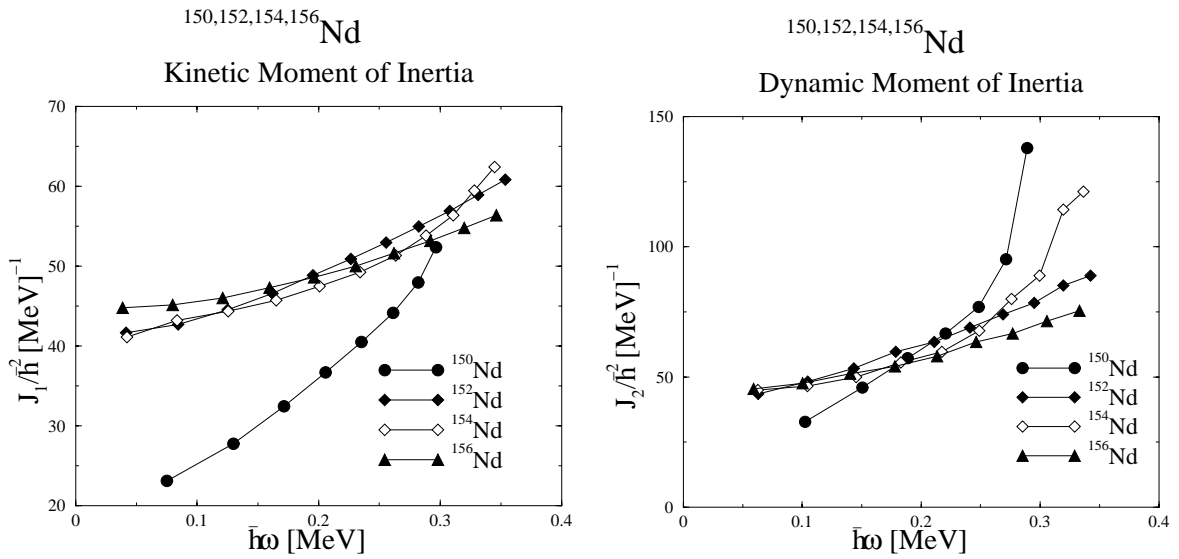


Figure 7.5: Kinetic and dynamic moments of inertia for ^{104}Mo ground and even and odd spin sequences of the γ -band.

have been observed in $^{252}\text{Cf}(\text{SF})$ to maximum spins of $16 \hbar$ [84], $18 \hbar$ [84, 85], $20 \hbar$ [85], and $16 \hbar$ [84], respectively. The rotational bands in ^{152}Nd and ^{154}Nd have been extended to $18 \hbar$ and $20 \hbar$, respectively [85]. In the present work, ^{150}Nd was also observed to a spin of $16 \hbar$, the ground bands of $^{152,154}\text{Nd}$ were extended to $22 \hbar$, and ^{156}Nd was extended to $20 \hbar$. The transition energies from this work agree well with those assigned in Ref. [85], except for the $20 \rightarrow 18$ transition in ^{152}Nd , which this work indicates is 662.4 keV instead of 669.3 keV. The newly identified levels with spin $22 \hbar$ in $^{152,154}\text{Nd}$ are the highest angular momentum yet observed in spontaneous fission products. The extended level diagrams for $^{150,152,154,156}\text{Nd}$ are shown in Figure 7.6 and the kinetic and dynamic moments of inertia are shown in Figure 7.7.

7.4 $^{156,158,160}\text{Sm}$

The ground state rotational bands of $^{156,158}\text{Sm}$ were identified in early spectroscopic studies of fission products to spins of $6 \hbar$ and $8 \hbar$, respectively [9]. In more recent work [86] the ground state rotational band in ^{160}Sm was identified to a spin of $14 \hbar$, and the bands in $^{156,158}\text{Sm}$ were extended to $14 \hbar$. In the present work the

Figure 7.6: Level diagrams for the ground bands of ^{150,152,154,156}NdFigure 7.7: Kinetic and dynamic moments of inertia for the ground bands of ^{150,152,154,156}Nd.

bands in $^{156,158,160}\text{Sm}$ were extended to spins of $18 \hbar$, $20 \hbar$ and $18 \hbar$, respectively. The level diagrams are shown in Figure 7.8, and the moments of inertia are shown in Figure 7.9. The authors of Ref. [86] note that there is an indication of a band crossing occurring in ^{156}Sm at spin $14 \hbar$. The rapid change in the dynamic moment of inertia at the higher observed spins in the present work shows that this band crossing does occur.

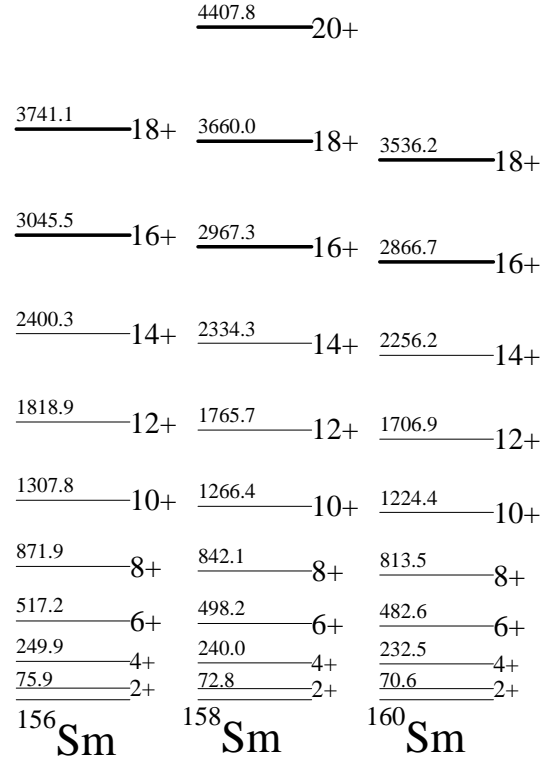
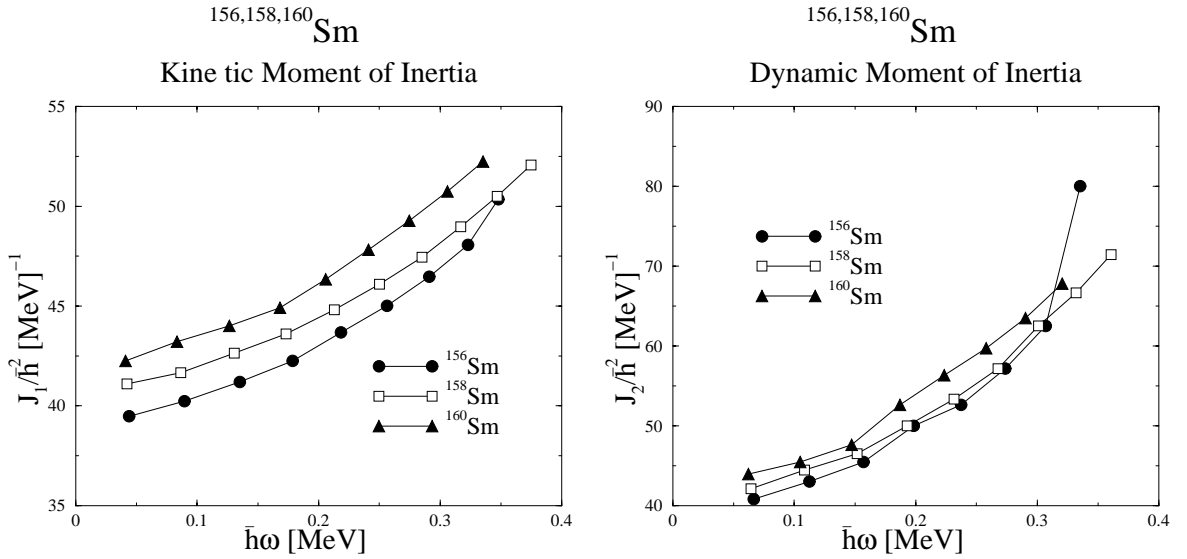
7.5 Summary

The spectroscopic study of $^{252}\text{Cf}(\text{SF})$ fission products using a thin source technique, described in Chapter 4, allows the observation of transitions occurring at higher spin and excitation energy than is possible with the thick source technique. Rotational bands can typically be extended by one to three levels allowing the structure of the nuclei to be studied at higher excitation energy.

The ground band of ^{112}Ru was extended two levels to a spin of $20 \hbar$ and the γ -band was extended seven levels to a spin of $17 \hbar$. The staggered spacing of the energy levels in the γ -band, when compared to the Rigid Tri-axial Rotor model, indicate that non-zero centroid of the γ shape parameter evident a low spin persists at higher spins.

The rotational bands in $^{102,104,106,108}\text{Mo}$ were extended, with the ground band in ^{104}Mo extended to a spin of $20 \hbar$, and the γ -band extended six levels to a spin of $16 \hbar$. The high spin states in ^{104}Mo allow the observation of the band crossing occurring in the ground band, and indicate that the γ -band also undergoes a similar crossing.

The ground bands in $^{152,154,156}\text{Nd}$ and $^{156,158,160}\text{Sm}$ were also extend one to three levels. $^{152,154}\text{Nd}$ were extended to a spin of $22 \hbar$, which is currently the highest observed angular momentum in spontaneous fission products.

Figure 7.8: Level diagrams for the ground bands of $^{156,158,160}\text{Sm}$ Figure 7.9: Kinetic and dynamic moments of inertia for the ground bands of $^{156,158,160}\text{Sm}$.

Chapter 8

Conclusion

This thesis consists of the development of a new method for studying neutron-rich nuclei produced in the spontaneous fission of ^{252}Cf . The technique involves coupling a large solid-angle charged-particle detector system with a large γ -ray detector array and using a thin fission source. Greater sensitivity and selectivity is offered by adding the particle- γ ray coincident technique to the high-statistics, high-fold γ -ray data collected by GAMMASPHERE. By detecting the fission products, which recoil freely into vacuum, the masses of the fission products can be deduced, and the γ rays can be unambiguously assigned to either the heavy or light fission partner. The mass information can be used to select γ rays from a specific mass region making it easier to analyze the resultant spectra. Regions of low-yield mass production also can be selectively enhanced. The mass gating has been used to extend the spectroscopic sensitivity to transitions from a nucleus produced at a level of less than 5×10^{-5} per fission. Level diagrams can be extended to higher spins and excitation energy in the thin source experiment since the line shapes for the γ rays from these short-lived transitions are not Doppler broadened, as in thick source experiments.

A major component of this work was the development of the charged-particle detector system, CHICO. The construction of this large solid-angle detector capable of handling high count rates was a necessary development enabling the thin source fission experiment to be carried out. The detector also extends the research opportunities studying other binary reactions with GAMMASPHERE. CHICO in conjunction with

GAMMASPHERE has been used to study nuclear structure via Coulomb excitation, transfer, and fusion-fission reactions. The detector comprises an array of 20 parallel plate avalanche counters (PPACs) covering an angular range of $12^\circ < \theta < 85^\circ$ and $95^\circ < \theta < 168^\circ$ and 280° in ϕ for a total solid angle of 2.8 sr. The PPACs have segmented anodes and a three-layer delay line cathode which provide an angular resolution of 9.4° in ϕ and 1° in θ . The time-of-flight difference of the reaction products can be measured with 500 ps resolution allowing a mass resolution of $\Delta m/m=5\%$ for beam reactions, and 8 mass units for spontaneous fission.

The added sensitivity and selectivity of this new technique was exploited in the study of the neutron-rich nuclei produced in $^{252}\text{Cf}(\text{SF})$. The ability to distinguish prompt γ rays from delayed γ rays via the Doppler correction was used to set limits on the lifetime of the $E3$ decay of the $\frac{23}{2}^-$ level in ^{135}I . The experimental limit of 5.0 ns agrees well with the shell model prediction. The ability to observe levels at higher spin was used to extend rotational bands in $^{102,104,106,108}\text{Mo}$, ^{112}Ru , $^{152,154,156}\text{Nd}$ and $^{156,158,160}\text{Sm}$. The band crossing region occurring in ^{104}Mo was observed to completion, and a band crossing in the γ -band of this nucleus was also observed. The higher spin states observed in ^{112}Ru indicate that the tri-axial behavior exhibited at lower spins continues at higher excitation energy. The ground bands of $^{152,154}\text{Nd}$ were extended to spins of $22 \hbar$. These are the largest angular momenta observed to date in fission products of $^{252}\text{Cf}(\text{Sf})$.

The level diagrams for the even mass neutron-rich Pd were extended and the shape properties were inferred based on identification of the orbitals responsible for the observed band crossings. The yrast bands in $^{112,114,116}\text{Pd}$ were extended to spins of $20 \hbar$. A probable negative parity band in ^{112}Pd and a second band crossing in ^{116}Pd were observed. Rotational structures also were newly identified in the odd mass $^{113,115}\text{Pd}$. The ground band of ^{113}Pd was identified to a spin of $\frac{23}{2} \hbar$ and a rotational band based on the low-lying $\frac{9}{2}^-$ isomeric level was identified to a spin of $\frac{41}{2}$. The ground band of ^{115}Pd was observed to a spin of $\frac{33}{2}$ and the rotational band based on the $\frac{9}{2}^-$ isomeric level was identified to a spin of $\frac{31}{2} \hbar$. The band crossings occurring in the even mass Pd are blocked in the neighboring odd- ν Pd indicating that the

aligning nucleons are a $\nu h(\frac{11}{2})$ neutron pair. This is consistent with the behavior of the band crossings occurring in the odd- π even- ν $^{111,113}\text{Rh}$, where the odd proton does not block the band crossing. Comparison to cranked shell model calculations indicate that the shape of the even mass Pd remains prolate, at least through ^{116}Pd .

The technique developed in this thesis of studying the neutron-rich fission products from $^{252}\text{Cf}(\text{SF})$ by the collection of high-statistics, high-fold γ -ray data in conjunction with the detection of the recoiling fission partners complements and extends the thick source experimental technique. The level diagrams of many nuclei have been developed previously using the thick source data. The majority of these nuclei are even-even or even-odd mass, and have been studied first because of their simpler decay schemes. With this new technique the decay schemes of these nuclei can be extended to higher excitation energies. With the added selectivity of this new technique, specifically the ability to assign the γ rays to either the heavy or light fission partner, the development of the decay schemes for the largely unexplored odd-odd nuclei will be an easier task.

The development of new detectors holds promise for future spectroscopic study of fission products. The next generation of γ -ray detector arrays, such as the proposed γ -ray energy tracking array, GRETA [103], will have higher peak efficiencies ($\geq 50\%$) and peak-to-total ratios (~ 0.8), and improved γ -ray position resolution of $\sim 3\text{mm}$. The latter will nearly eliminate the Doppler-broadened line shapes ensuing from the finite size of the γ -ray detectors in the present arrays. The sensitivity provided by the high efficiency and the selectivity provided by the higher γ -ray fold of these new arrays will extend the observable region of neutron-rich nuclei even further.

Bibliography

- [1] I. Y. Lee, S. Asztalos, M.-A. Deleplanque, B. Cederwall, R. M. Diamond, P. Fallon, A. O. Macchiavelli, L. Phair, S. G. Frauendorf, J. A. Becker E. A. Henry, P. F. Hua, D. G. Sarantites, J. X. Saladin, C. H. Yu, Phys. Rev. C **56**, 753 (1997)
- [2] R. Broda, B. Fornal, W. Królas, ttttt. Pawlat, D. Bazzacco, S. Lunardi, C. Rossi-Alvarez, R. Menegazzo, G. de Angelis, P. Bednarczyk, J. Rico, D De Acuña, P. J. Daly, P. H. Mayer, M. Sferrazza, H. Grawe, K. H. Maier, R. Scubart, Phys. Rev. Lett. **74**, 868 (1995)
- [3] C. Y. Wu, M. W. Simon, D. Cline, G. A. Davis, A. O. Macchiavelli, K. Vetter, Phys. Rev. C **57**, 3466 (1998)
- [4] M. Bernas, S. Czajkowski, P. Armbruster, H. Geissel, Ph. Dessagne, C. Donzaud, H-R. Faust, E. Hanelt, A. Heinz, M. Hesse, C. Kozhuharov, Ch. Mieke, G. Müzenberg, M. Pfützner, C. Röhl, K.-H. Schmidt, W. Schwab, C. Stéphan, K. Sümmerer, L. Tassan-Got, B. Voss, Phys. Lett. B **331** 19, (1994)
- [5] H. Scheit, T. Glasmacher, B. A. Brown, J. A. Brown, P. D. Cottle, P. G. Hansen, R. Harkewicz, M. Hellström R. W. Ibbotson, J. K. Jewell, K. W. Kemper, D. J. Morrissey, M. Steiner, P. Thirolf, M. Thoennessen, Phys. Rev. Lett. **77**, 3967 (1996)
- [6] K. Rykaczewski, R. Grzywacz, M. Lewitowicz, M. Pfützner, H. Grawe, Proceedings of the International Conference on Fission and Properties of Neutron Rich Nuclei. Sanibel Island Fl November 10-15 1997 , World Scientific Publishing Co., 416

- [7] H. R. Bowman, S. G. Thompson, J. O. Rasmussen Phys. Rev. Lett. **12**, 195 (1964)
- [8] E. Cheifetz, R. C. Jared, S. G. Thompson, J. B. Wilhelmy, Phys. Rev. Lett. **25**, 38 (1970)
- [9] J. B. Wilhelmy, S. G. Thompson, R. C. Jared, E. Cheifetz, Phys. Rev. Lett. **25**, 1122 (1970)
- [10] J. H. Hamilton, A. V. Ramayya, S. J. Zhu, G. M. Ter-Akopian, Yu Ts Oganessian, J. D. Cole, J. O. Rasmussen, M. A. Stoyer, Prog. in Nucl. and Part. Phys. **35**, 635 (1995)
- [11] M. G. Mayer, Phys. Rev. **75**, 1969 (1949)
- [12] S. B. Nilsson, Mat.-fys. Med. **29**, 1 (1955)
- [13] D. L. Hill, J. A. Wheeler, Phys. Rev. **89**, 1102 (1953)
- [14] K. Kumar, *The Electromagnetic Interaction in Nuclear Spectroscopy* ed. W. D. Hamilton, (North Holland Publishing Company, 1975) 55
- [15] *Nuclear Theory*, J. M. Eisenberg, W. Greiner, (North-Holland Physics Publishing, 1987)
- [16] D. R. Inglis, Phys. Rev. **96**, 1059 (1953)
- [17] M. J. A. de Voigt, J. Dudek, Z. Szymanski, Rev. Mod. Phys. **55**, 949 (1983)
- [18] R. K. Sheline, Nuc. Phys. A **195**, 321 (1972)
- [19] S. M. Harris, Phys. Rev. B **138**, 509 (1965)
- [20] Gammasphere, A National Gamma-ray Facility, The Proposal, ed. M. A. Deleplanque, R. M. Diamond, March 1988, Lawrence Berkeley Lab. Publ., 5202 (1988)
- [21] D. Cline, An. Rev. of Nucl. and Part. Sci. **36**, 683 (1986)

- [22] C. Y. Wu, W. von Oertzen, D. Cline, M. W. Guidry, *An. Rev. of Nucl. and Part. Sci.* **40**, 285 (1990)
- [23] I. Y. Lee, *Proceedings of the Workshop on Gammasphere Physics*, ed. M. A. Deleplanque, I. Y. Lee and A. O. Machiavelli, World Scientific, 50 (1995)
- [24] *GAMMASPHERE The Beginning...1993-1997*, ed. M. A. Riley
- [25] H. Stelzer, *Nucl. Instr. and Meth. A* **133**, 409 (1976)
- [26] D. Cline, B. Kotlinski, *UR-NSRL Biennial Report 1982-83*, 363
- [27] D. Cline, E. G. Vogt, J. Hall, A. E. Kavka, W. J. Kernan, *UR-NSRL Annual Report 1987*, 149
- [28] RCG Research, Inc., Indianapolis IN
- [29] C. Long, personal communication
- [30] R. W. Gray, personal communication
- [31] GEANT, version 3.159, R. Brun, F. Bruyant, M. Maire, A. C. McPherson, P. Zancarini, *GEANT3 User's Guide*, DD/EE/84-1, CERN, 1987
- [32] C. Y. Wu, D. Cline, M. W. Simon, C. Fahlander, T. Härtlein, A. O. Macchiavelli, K. Vetter, L. Corradi, to be published, 1998
- [33] K. Vetter, A. O. Macchiavelli, D. Cline, H. Amro, S. J. Assztalos, B. C. Busse, R. M. Clark, M. A. Delaplanque, R. M. Diamond, P. Fallon, R. Gray, R. V. F. Janssens, R. Krucken, I.Y. Lee, R. W. MacLeod, G. J. Schmid, M. W. Simon, F. S. Stephens, C. Y. Wu, *Phys. Rev. C* **58**, R2631 (1998)
- [34] K. Vetter, A. O. Macchiavelli, S. J. Asztalos, R. M. Clark, M. A. Deleplanque, R. M. Diamond, P. Fallon, I. Y. Lee, F. S. Stephens, D. Ward, H. Amro, R. V. F. Janssens, J. Gerl, H.-J. Wollersheim, D. Cline, M. W. Simon, C. Y. Wu, proposal submitted to Argonne National Laboratory, 1998

- [35] D. Cline, G. A. Davis, C. Y. Wu, M. W. Simon, R. Teng, I.Y. Lee, A. O. Macchiavelli, K. Vetter, Proc. of Nucl. Phys. Fall Meeting, Bull. Amer. Phys. Soc. 43, 1584 (1998)
- [36] K. Vetter *et al.*, proposal submitted to Lawrence Berkeley National Laboratory, 1996
- [37] M. Devlin, R. J. Charity, F. L. Lerma, D. G. Sarantites, D. Cline, M. W. Simon, C. Y. Wu, proposal submitted to Argonne National Laboratory, 1998
- [38] Ch. Schlegel, D. Cline, J. Gerl, T. Härtlein, E. Lubkiewicz, M. Rejmund, M. W. Simon, K. Vetter, H. J. Wollersheim, C. Y. Wu, proposal submitted to Argonne National Laboratory, 1998
- [39] A. G. Smith, J. L. Durell, W. R. Phillips, M. A. Jones, M. Leddy, W. Urban, B. J. Varley, I. A. Ahmad, L. R. Morss, M. Bentaleb, A. Guessous, E. Lubkiewicz, N. Schulz, R. Wyss, Phys. Rev. Lett. **77**, 1711 (1996)
- [40] A. G. Smith, W. R. Phillips, J. L. Durell, W. Urban, B. J. Varley, C. J. Pearson, J. A. Shannon, I. Ahmad, C. J. Lister, L. R. Morss, K. L. Nash, C. W. Williams, M. Bentaleb, E. Lubkiewicz, N. Schulz, Phys. Rev. Lett. **73**, 2540 (1994)
- [41] J. K. Hwang, A. V. Ramayya, J. H. Hamilton, L. K. Peker, J. Kormicki, B. R. S. Babu, T. N. Ginter, G. M. Ter-Akopian, Yu. Ts. Oganessian, A. V. Daniel, W. C. Ma, P. G. Varrette, J. O. Rasmussen, S. J. Asztalos, S. Y. Chu, K. E. Gregorich, A. O. Macchiavelli, R. W. Macleod, J. Gilat, J. D. Cole, R. Aryaeinejad, K. Butler-Moore, M. W. Digert, M. A. Stoyer, Y. X. Dardenne, J. A. Becker, L. A. Bernstein, R. W. Loughheed, K. J. Moody, S. G. Prussin, H. C. Griffin, R. Donangelo, Phys. Rev. C **56**, 1344 (1997)
- [42] J. H. Hamilton, A.V. Ramayya, J.K. Hwang, J. Kormicki, B. R. S. Babu, A. Sandulescu, A. Florescu, W. Greiner, G.M. Ter-Akopian, Yu. Ts. Oganessian, A.V. Daniel, S. J. Zhu, M. G. Wang, T. Ginter, J. K. Deng, W. C. Ma, G. S. Popeko, Q. H. Lu, E. Jones, R. Dodder, P. Gore, W. Nazerewicz, J. O. Rasmussen, S. Asztalos, I. Y. Lee, S. Y. Chu, K. E. Gregorich, A. O. Macchiavelli,

- M. F. Mohar, S. Prussin, M. A. Stoyer, R. W. Lougheed, K. J. Moody, J. F. Wild, L. A. Bernstein, J. A. Becker, J. D. Cole, R. Aryaeinejad, Y. X. Dardenne, M. W. Drigert, K. Butler-Moore, R. Donangelo, H. C. Griffin, *Prog. in Nucl. Part. Phys.* **38**, 273 (1997)
- [43] *Table of Isotopes*, 8th ed., edited by R. Firestone and V. S. Shirley (Wiley, New York, 1996)
- [44] H. W. Schmitt, J. H. Neiler, F. J. Walter, *Phys. Rev. C* **141**, 1146 (1966)
- [45] A. Gavron, Z. Fraenkel, *Phys. Rev. C* **9**, 632 (1974)
- [46] P. David, J. Debrus, F. Lübke, H. Mommsen, R. Schoenmackers, *Phys. Lett. B* **60**, 445 (1976)
- [47] U. Brosa, S. Grossmann, A. Müller *Z. Naturforsch. A* **41**, 1341 (1986)
- [48] H. Ernst, in *ENELOSS (Ion Ranges in Matter)*, modified by K. Lesko, (Argonne National Laboratory, IL, 1981)
- [49] D. C. Radford, *Nucl. Inst. and Methods A* **361**, 297 (1995)
- [50] D. C. Radford, *Nucl. Inst. and Methods A* **361**, 306 (1995)
- [51] T. R. England, B. F. Rider, LA-UR-94-3106
- [52] J. A. Shannon, W. R. Phillips, J. L. Durell, B. J. Warley, W. Urban, C. J. Pearson, I. Ahmad, C. J. Lister, L. R. Morss, K. L. Nash, C. W. Williams, N. Schultz, E. Lubkiewicz, M. Bentaleb, *Phys. Rev. Lett. B* **73**, 2540 (1994)
- [53] Q. H. Lu, K. Butler-Moore, S. J. Zhu, J. H. Hamilton, A. V. Ramayya, V. E. Oberacker, W. C. Ma, B. R. S. Babu, J. K. Deng, J. Kormicki, J. D. Cole, R. Aryaeinejad, Y. X. Dardenne, M. Drigert, L. K. Peker, J. O. Rasmussen, M. A. Stoyer, S. Y. Chu, K. E. Gregorich, I. Y. Lee, M. F. Mohar, J. M. Nitschke, N. R. Johnson, F. K. McGowan, G. M. Ter-Akopian, Yu. Ts. Oganessian, J. B. Gupta, *Phys. Rev. C* **52**, 1348 (1995)

- [54] J. Skalski, S. Mizutori, W. Nazarewicz, Nucl. Phys. A **617**, 282 (1997)
- [55] P. Möller, J. R. Nix, At. Data Nucl. Data Tables **26**, 165 (1981)
- [56] P. Möller, J. R. Nix, W. D. Myers, W. J. Swiatecki, At. Data Nucl. Data Tables, **59**, 185 (1995)
- [57] K. R. Pohl, P. H. Regan, J. E. Bush, P. E. Raines, D. P. Balamuth, D. Ward, A. Galindo-Uribarri, V. P. Janzen, S. M. Mullins, S. Pilotte, Phys. Rev. C **53**, 2682 (1996)
- [58] P. H. Regan, T. M. Menezes, C. J. Pearson, W. Gelletly, C. S. Purry, P. M. Walker, S. Juutinen, R. Julin, K. Helariutta, A. Savelius, P. Jones, P. Jämsen, M. Muikku, P. A. Butler, G. Jones, P. Greenlees, Phys. Rev. C **55**, 2305 (1997)
- [59] T. Kutsarova, A. Minkova, M.-g. Porquet, I. Deloncle, E. Gueorguieva, F. Azaiez, S. Bouneau, C. Boureois, J. Duprat, B. J. P. Gall, C. Gautherin, F. Hoellinger, R. Lucas, N. Schulz, H. Serolle, Ts. Venkova, A. Wilson, Phys. Rev. C **58**, 1966 (1998)
- [60] J. Äystö, C. N. Davids, J. Hattula, J. Honkanen, K. Honkanen, P. Jauho, R. Julin, S. Juutinen, J. Kumpulainen, T. Lönnroth, A. Pakkanen, A. Passoja, H. Penttilä, P. Taskinen, E. Verho, A. Virtanen, M. Yoshii, Nucl. Phys. A **480**, 104 (1988)
- [61] H. Penttilä, T. Enqvist, P.P. Jauho, A. Jokinen, M. Leino, J.M. Parmonen, J. Äystö, Nucl. Phys. A **561**, 416 (1993)
- [62] J. Äystö, P. Taskinen, M. Yoshii, J. Honkanen, Jauho, H. Penttilä, C.N. Davids, Phys. Lett. B **201**, 211 (1988)
- [63] R. Bengtsson, S. Frauendorf, F.-R. May, At. Data Nucl. Data Tables **35**, 15 (1986)
- [64] R. Aryaeinejad, J. D. Cole, R. C. Greenwood, S. S. Harrill, N. P. Lohstreter, K. Butler-Moore, S. Zhu, J.H. Hamilton, A. V. Ramayya, X. Zhao, W. C. Ma, I.

- Y.Lee, N. R. Johnson, F. K. McGowan, G. Ter-Akopian, Y. Oganessian, Phys. Rev. C **48**, 566 (1993)
- [65] J.Blachot, G.Marguier, Nucl. Data Tables **67**, 1 (1992)
- [66] H. Penttilä, J. Äystö, K. Eskola, P. P. Jauho, A. Jokinen, M. E. Leino, J-M. Parmonen, 6th Int. Conf. on Nuclei Far From Stability & 9th Int. Conf. on Atomic Masses and Fundamental Constants, Bernkastel-Kues, 647 (1992)
- [67] H. Penttilä, J. Äystö, P. Jauho, A. Jokinen, J. M. Parmonen P. Taskinen, K. Eskola, M. Leino, P. Dendooven, C. N. Davids, Phys. Scr. T **32**, 935 (1990)
- [68] G. Lhersonneau, B. Pfeiffer, J. Alstad, P. Dendooven, K. Eberhardt, S. Hankonen, I. Klöckl, K.-L. Kratz, A. Nähler, R. Malmbeck, J. P. Omtvedt, H. Penttilä, S. Schoedder, G. Skarnemark, N. Trautmann, J. Äystö, Eur. Phys. J. A **1**, 285 (1998)
- [69] J. Rogowski, J. Alstad, M. M. Fowler, D. De Frenne, K. Heyde, E. Jacobs, N. Kaffrell, G. sKarnemark, N. Trautmann Z. Phys A **337**, 233 (1990)
- [70] B. Fogelberg, E. Lund, Y. Zongyuan, B. Ekström, Proc. 5th Int. Conf. on nuclei far from stability, I. S. Towner(ed.), Rosseau Lake, Ontario, Canada, 296 (1987)
- [71] K. Heyde, V. Paar, Phys. Lett. B **179**, 1 (1986)
- [72] J. Gilat, personal communication
- [73] A. Bohr, B. R. Mottelson (W. A. Benjamin, Inc., Reading MA) *Nuclear Structure* v. II, 1975
- [74] B. Fogelberg, M. Hellström, D. Jerrestam, H. Mach, J. Blomqvist, A. Kerek, L. O. Norlin, J. P. Omtvedt, Phys. Scr. T **56**, 79, (1995)
- [75] P. Bhattacharyya, C. T. Zhang, B. Fornal, P. J. Daly, Z. W. Grabowski, I. Ahmad, T. Lauritsen, L. R. Morss, W. R. Phillips, J. L. Durell, M. J. Leddy, A. G. Smith, W. Urban, B. J. Varley, N. Schulz, E. Lubkiewicz, M. Bentaleb, J. Blomqvist, Phys. Rev. C **56**, R2363 (1997)

- [76] C. T. Zhang, P. Bhattacharyya, P. J. Daly, R. Broda, Z. W. Grabowski, D. Nisius, I. Ahmad, M. P. Carpenter, T. Lauritsen, L. R. Morss, W. Urban, J. L. Durell, W. R. Phillips, M. J. Leddy, A. G. Smith, B. J. Varley, N. Schulz, E. Lubkiewicz, M. Bentaleb, J. Blomqvist, *Z. Phys. A* **358**, 9 (1997)
- [77] C. T. Zhang, P. Bhattacharyya, P. J. Daly, R. Broda, Z. W. Grabowski, D. Nisius, I. Ahmad, T. Ishii, M. P. Carpenter, L. R. Morss, W. R. Phillips, J. L. Durell, M. J. Leddy, A. G. Smith, W. Urban, B. J. Varley, N. Schultz, E. Lubkiewicz, M. Bentaleb, J. Blomqvist, *Phys. Rev. Lett.* **77**, 3743 (1996)
- [78] J. P. Omtvedt, H. Mach, B. Fogelberg, D. Jerrestam, M. Hellström, L. Spanier, K. I. Erokhina, V. I. Isakov, *Phys. Rev. Lett.* **75**, 3090 (1995)
- [79] *Theory of the Nuclear Shell Model*, R. D. Lawson, (Claredon Press, 1980)
- [80] F. Andreozzi, L. Coraggio, A. Covello, A. Gargano, T. T. S. Kuo, A. Porrino, *Phys. Rev. C* **56**, R16 (1997)
- [81] M. Devlin, personal communication
- [82] A. S. Davydov, G. F. Filippov, *Nucl. Phys.* **8**, 237 (1958)
- [83] A. Guessous, N. Schulz, M. Bentaleb, E. Lubkiewicz, J. L. Durell, C. J. Pearson, W. R. Phillips, J. A. Shannon, W. Urban, B. J. Varley, I. Ahmad, C. J. Lister, L. R. Morss, K. L. Nash, C. W. Williams, S. Khazrouni, *Phys. Rev. C* **53**, 1191 (1996)
- [84] S. J. Zhu, J. H. Hamilton, Q. H. Lu, A. V. Ramayya, M. G. Wang, B. R. S. Babu, T. N. Ginter, W. C. Ma, J. K. Deng, D. Shi, J. Kormicki, J. D. Cole, R. Aryaeinejad, Y. X. Dardenne, M. W. Drigert, N. R. Johnson, I. Y. Lee, F. K. McGowan, G. M. Ter-Akopian, Yu. Ts. Oganessian, J. O. Rasmussen, M. A. Stoyer, S. Y. Chu, K. E. Gregorich, M. F. Mohar, S. Prussin, *J. Phys. G* **21**, L75 (1995)
- [85] X. Q. Zhang, J. H. Hamilton, A. V. Ramayya, L. K. Peker, J. K. Hwang, E. F. Jones, J. Komicki, C. J. Beyer, P. M. Gore, B. R. S. Babu, T. N. Ginter, S.

- J. Asztalos, S. Y. Chu, K. E. Gregorich, I. Y. Lee, A. O. Macchiavelli, R. W. Macleod, J. O. Rasmussen, J. Gilat, G. M. Ter-Akopian, Yu. Ts. Oganessian, A. V. Daniel, W. C. Ma, P. G. Varmette, J. D. Cole, R. Aryaeinejad, D. Butler-Morre, Y. X. Dardenne, M. W. Drigert, M. A. Stoyer, J. F. Wild, J. A. Becker, L. A. Bernstein, R. W. Loughheed, K. J. Moody, R. Donangelo, S. G. Prussin, H. C. Griffin, *Phys. Rev. C* **57**, 2040 (1998)
- [86] S. J. Zhu, J. H. Hamilton, A. V. Ramayya, B. R. S. Babu, Q. H. Lu, W. C. Ma, T. N. Ginter, M. G. Wang, J. Kormicki, J. K. Deng, D. Shi, J. D. Cole, R. Aryaeinejad, J. Rasmussen, M. A. Stoyer, S. Y. Chu, K. E. Gregorich, M. F. Mohar, S. Prussin, G. M. Ter-Akopian, Yu. Ts. Oganessian, N. R. Johnson, I. Y. Lee, F. K. McGowan, *J. Phys. G.* **21**, L57 (1995)
- [87] E. G. Vogt, D. Cline, T. Czosnyka, A. E. Kavka, W. J. Kernan, C. Y. Wu, R. M. Diamond, F. S. Stephens, M. A. Deleplanque, J. deBoer, Ch. Lauterbach, C. Fahlander, B. Varnevig UR-NSRL Annual Report 1987, 14
- [88] E. G. Vogt, D. Cline, F. Kowalik, D. Kotlinski, C. Y. Wu, P. Butler, N. Clarkson, G. Jones, C. White UR-NSRL Annual Report 1988, 22
- [89] T. Czosnyka, D. Cline, C. Y. Wu, 'GOSIA users manual' UR-NSRL-305, 1991, and *Bull. Amer. Phys. Soc.* **28**, 745 (1983)
- [90] E. G. Vogt, personal communication
- [91] P. H. Stelson, L. Grodzins, *Nuclear Data A* **1**, 21 (1965)
- [92] R. A. Bark, personal communication
- [93] R. Ibbotson, B. Kotlinski, D. Cline, K.G. Helmer, A. E. Kavka, A. Renalds, E. G. Vogt, P. A. Butler, C. A White, R. Wadsworth, D. L. Watson, *Nucl. Phys. A* **530**, 199 (1991).
- [94] B. Kotlinski, D. Cline, A. Bäcklin, D. Clark, *Nucl. Phys. A* **503**, 575 (1989)

- [95] C. Y. Wu, D. Cline, E. G. Vogt, W. J. Kernan, T. Czosnyka, K. G. Helmer, R. Ibbotson, A. E. Kavka and B. Kotlinski, Nucl. Phys. A **533**, 359 (1991)
- [96] N. Anyas-Weiss, R. Griffiths, N. A. Jelley, W. Randolph, J. Szücs, T. K. Alexander, Nucl. Phys. A **201**, 513 (1973)
- [97] M. W. Guidry, R. J. Sturm, N. R. Johnson, E. Eichler, G. D. O'Kelly, N. c. Singhal, R. O. Sayer, Phys. Rev. C **13**, 1164 (1976)
- [98] D. Cline, NSRL Annual Report 1981, 236
- [99] L. K. Peker, Nucl. Data Sheets **65**, 439 (1992)
- [100] C. Y. Wu, personal communication
- [101] R. J. Storm and M. W. Guidry, Nucl. Inst. and Meth. **138**, 345 (1976)
- [102] F. Rosel, H. M. Fries, K. Adler and H. C. Pauli, At. And Nucl. Data Tables, **21** (1978)
- [103] I. Y. Lee, Proceedings of the Workshop on GRETA Physics, A Slide Report, Ernest Orlando Lawrence Berkeley National Laboratory February 5-7 1998, 3

Appendix A

Lifetime Measurement of low-lying levels in ^{165}Ho

A.1 Introduction

^{165}Ho is a well deformed nucleus with an unpaired proton in the $\frac{7}{2}[523]$ Nilsson orbital. ^{165}Ho also has $K=\frac{3}{2}^-$ and $K=\frac{11}{2}^-$ levels which have been interpreted as γ -vibrations. The configurations of these γ -vibrational levels involve the coupling of a $K=2$ quadrupole phonon to the $\frac{7}{2}^-$ ground state. These two collective levels indicate that ^{165}Ho exhibits a γ -degree of freedom. Because of this nuclei's strong quadrupole deformation the level diagram also exhibits collective rotational bands built on the ground state and the two γ -vibrational states. These collective vibrational and rotational features make this nucleus a good candidate to test the validity of collective models in strongly deformed odd-A nuclei. For this purpose a study of this nucleus had been initiated with the goal of measuring the complete set of electric and magnetic matrix elements connecting the low-lying collective states by using Coulomb excitation. Coulomb excitation preferentially populates the collective states of a nucleus making it the ideal probe for such an investigation. The motivation for the present recoil-distance method (RDM) lifetime measurement of the low-lying levels of ^{165}Ho was to confirm the results from Coulomb excitation experiments performed by E. Vogt *et al* [87, 88].

A.1.1 The Coulomb Excitation Experiments

Several Coulomb excitation experiments of ^{165}Ho were performed previously using ^{16}O , ^{58}Ni , and ^{208}Pb beams [87]. By measuring the excitation process using projectiles with different nuclear charge over a wide range of scattering angles, it is possible to over-determine the values of the electro-magnetic matrix elements connecting the low-lying levels. In these experiments four rotational bands were observed, the negative parity ground-state band, the negative parity $K=\frac{11}{2}^-$ and $K=\frac{3}{2}^-$ γ -vibrational bands, and a positive parity $K=\frac{3}{2}^+$ band based on the $\pi\frac{3}{2}[411]$ orbital. A diagram of levels observed in these experiments is presented in Figure A.1. The ground band was observed to a spin of $\frac{53}{2}$, the $K=\frac{11}{2}^-$ and $K=\frac{3}{2}^-$ bands were populated to spins of $\frac{37}{2}$ and $\frac{21}{2}$, respectively, and the positive parity band was populated to a spin of $\frac{11}{2}$. The matrix elements from the experimental γ -ray yields and scattering angles were determined from a fit to the data using the Coulomb excitation least squares search code GOSIA [89]. The complete error analysis for matrix elements and lifetimes from these experiments has not been completed and the errors presented are preliminary and may underestimate the true errors.

The electro-magnetic matrix elements measured [90] via these Coulomb excitation experiments indicate that the intrinsic quadrupole moment, eQ_0 , of the $K=\frac{11}{2}^-$ and $K=\frac{3}{2}^-$ γ -vibrational bands are anomalously large, 15 to 40 percent larger than that of the ground band. This result is surprising when interpreted within the framework of the collective model. In this model the γ bands are not expected to have a deformation, or hence an intrinsic quadrupole moment, significantly different than the ground state. The significant difference in deformation of the γ -vibrational band and ground-state band might be explained by a change in the underlying microscopic configuration of the valence nucleons. This, however, is not supported by calculations [92]. The origin of the larger than expected quadrupole moments of the γ bands remains an unanswered question.

A.1.2 Intrinsic Moments of Bands in ^{165}Ho from In-Band Matrix Elements

The in-band electric matrix elements of a rotational band give a direct measure of its intrinsic quadrupole moment, eQ_0 . Assuming axial symmetry of the nucleus, the intrinsic quadrupole moment is related to the in-band reduced matrix elements

by the relation given in [73]:

$$\langle KI_2 || M(E2) || KI_1 \rangle = (2I_1 + 1)^{\frac{1}{2}} \langle I_1 K 20 | I_2 K \rangle \left(\frac{5}{16\pi} \right)^{\frac{1}{2}} eQ_o \quad (\text{A.1})$$

For the simple collective model the intrinsic moment eQ_o also can be related to the quadrupole deformation parameter β_2 in a model dependent way by

$$Q_o = \frac{3}{\sqrt{5\pi}} Z \left(1.2 A^{\frac{1}{3}} \right)^2 \beta_2 \quad (\text{A.2})$$

$$\beta_2 = \beta'_2 \left(1 + 0.16\beta'_2 + 0.20\beta'^2_2 \right) \quad (\text{A.3})$$

where equation A.2 gives the value of β_2 assuming small deformations. The third order expansion in equation A.3 defines the deformation parameter β'_2 , which assumes a spheroidal shape for the nucleus, even for larger deformations, and a sharp radial cutoff for the nuclear charge distribution [91].

The values for the intrinsic quadrupole moment extracted from the measured static ($\Delta J=0$) and transitional ($\Delta J=1,2$) matrix elements from Vogt *et al.*, assuming axial symmetry (Equation A.1), are shown in Table A.1. The intrinsic quadrupole moments listed in the table are weighted averages of the measured matrix elements of a particular ΔJ for the given band. The β'_2 are calculated only from the $\Delta J=2$ matrix elements, since experimentally these are more accurately measured because of their pure E2 nature. The intrinsic quadrupole moments and deformations deduced from the in-band matrix elements for the $K=\frac{3}{2}^-$ and $K=\frac{11}{2}^-$ are significantly larger than for the ground band. The $K=\frac{11}{2}^-$ band's deformation of $\beta'_2 = 0.43 \pm 0.04$ is unusually large when compared to typical deformations in the rare-earth region of $\beta_2 \sim 0.3$.

A.1.3 Motivation for the Lifetime Measurement Experiment

For a complex level spectrum, such as the level spectrum of odd-A ^{165}Ho , there can be several hundred matrix elements which need to be fit simultaneously. A difficulty with the Coulomb excitation least squares search analysis, since the parameter space is so large, is ensuring that the minimum found actually is a global minimum.

	$\Delta J = 0$ (eb)	$\Delta J = 1$ (eb)	$\Delta J = 2$ (eb)	$\beta'_2(\Delta J = 2)$
$K=\frac{7}{2}^-$	$eQ_o = 5.68 \pm 0.44$	$eQ_o = 6.3 \pm 1.3$	$eQ_o = 7.45 \pm 0.38$	$.316 \pm .014$
$K=\frac{11}{2}^-$	$eQ_o = 7.3 \pm 1.2$	$eQ_o = 8.85 \pm 0.71$	$eQ_o = 10.5 \pm 1.2$	$.430 \pm .042$
$K=\frac{3}{2}^-$	$eQ_o = 8.0 \pm 2.4$	$eQ_o = 8.1 \pm 2.0$	$eQ_o = 8.56 \pm 0.34$	$.359 \pm .012$

Table A.1: Quadrupole moments and deformations of the $K=\frac{7}{2}^-$ ground band and the $K=\frac{11}{2}^-$, $\frac{3}{2}^-$ γ -bands of ^{165}Ho measured by Coulomb excitation.

Extracting matrix elements from a local rather than the global minimum would give erroneous results not representative of the best fit to the data. The surprising result of larger than expected intrinsic quadrupole moments in the γ -bands from the Coulomb excitation analysis suggest the need for additional experiments to provide independent confirmation that the Coulomb excitation results are correct, and are not an artifact of the analysis finding a non-global minimum.

In the present work, an additional experiment, a direct measure of the lifetimes of the low-lying levels by the recoil-distance method (RDM), was performed to provide an independent measurement of the properties of the low-lying levels of ^{165}Ho . The directly measured lifetimes and deduced matrix elements from the recoil-distance experiment can be compared to the lifetimes and matrix elements derived from the Coulomb excitation work.

A.2 The Recoil-Distance Lifetime Experiment

A.2.1 Experimental Method

The mean lifetimes of low-lying levels of ^{165}Ho are expected to be in the picosecond range. The measurement of the lifetimes was performed using the recoil-distance method (RDM), which can measure lifetimes in the picosecond range. This experiment is similar to previous lifetime measurements of ^{148}Nd [93], ^{110}Pd [94], and $^{182,184}\text{W}$ [95]. A detailed description of the recoil-distance method can be found in references [96, 97].

The experimental setup is shown in Figure A.2. A beam of 230 MeV ^{58}Ni ions, accelerated by the Rochester MP Tandem Van de Graaff, was used to Coulomb excite a $280\text{ }\mu\text{g}/\text{cm}^2$ ^{165}Ho target. The target was prepared by sputtering ^{165}Ho onto a $480\text{ }\mu\text{g}/\text{cm}^2$ Ni foil. The foil was then stretched to form a flat, reflective surface. The backscattered ^{58}Ni ions were detected in an annular parallel plate avalanche counter (PPAC) [98] placed 5.4 cm upstream from the target. The PPAC covers a scattering angular range of 138° to 168° corresponding to a calculated recoil for the ^{165}Ho nuclei into a forward cone extending from 3.9° to 14.2° . The recoiling nuclei were slowed by a movable $2.8\text{ mg}/\text{cm}^2$ stretched ^{58}Ni foil (shifter foil) mounted between the target and the γ -ray detector. The target foil and shifter foil were optically aligned to be parallel within 0.05° , corresponding to $2.46\text{ }\mu\text{m}$ variation in distance over the beam spot diameter. The shifter foil reduces the velocity of the recoiling nuclei to a value of $\beta = 0.0228 \pm 0.0005$, measured by the Doppler effect, where β is the fraction of the speed of light ($\frac{v}{c}$). The initial recoil velocities of the nuclei were measured by replacing the shifter foil with a foil ($11.3\text{ mg}/\text{cm}^2$ Ni) sufficiently thick to stop the recoils. The Doppler shifted energy of γ rays from the recoiling nuclei compared to the un-shifted γ -ray energy of the stopped nuclei yielded a measurement of the average initial recoil velocity to be $\beta = 0.0421 \pm 0.0007$, introducing a difference in the Doppler shifted energy between γ rays emitted before the shifter foil (“fast” γ rays) and γ rays emitted after the shifter foil (“slow” γ rays). This difference in the Doppler shifted energy allows the “fast” and “slow” peaks to be distinguished easily. For a 431 keV

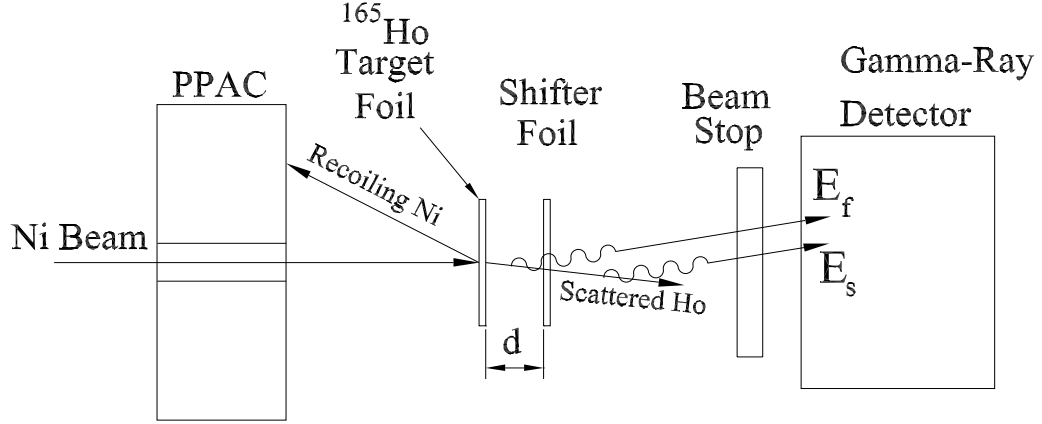


Figure A.2: Schematic of the Recoil-Distance Lifetime Experiment

γ ray the peak-to-peak separation between the “fast” and “slow” peak is 8.3 keV. The γ rays were detected by a Compton suppressed Ge detector, placed at 0° with respect to the beam axis, in coincidence with backscattered ^{58}Ni ions.

An “Inchworm” transducer was used to adjust the separation distance between the target and shifter foil. For distances less than $40\mu\text{m}$ a capacitive measurement was used to determine the separation to within $\pm 1\mu\text{m}$. Larger separations were measured to an accuracy of $\pm 2\mu\text{m}$ using a optical readout installed on the “Inchworm” transducer. Gamma ray spectra were collected at 10 separate distances from $12\mu\text{m}$ to $1300\mu\text{m}$. These separation distances between the target and shifter foils correspond to flight times for the recoiling ^{165}Ho nuclei ranging from 0.95 ps to 102.9 ps.

A.2.2 Lifetime analysis

The lifetimes are measured by comparing the intensities of the “fast” (I_f) and “slow” (I_s) component of a transition as a function of the separation distances (d) between the target and shifter foil. For a constant recoil velocity v , the mean lifetime τ of a level is given to first order by the exponential decay described by $\ln R = -d/v\tau$.

R is the ratio defined by

$$R = \frac{I_s}{I_s + I_f} \quad (\text{A.4})$$

in the case where both the “fast” and “slow” peak can be fit. For cases where the fast peak could not be fit reliably due to contamination from other transitions, R was calculated using

$$R = \frac{I_s}{N} \quad (\text{A.5})$$

where N is the total number of recoil nickel ions detected in the PPAC and is proportional to total yield of a transition, $I_f + I_s$.

To first order, in a plot of $\ln R$ vs d , the slope of the data is $-1/v\tau$. Since N is proportional to the total yield of a given transition, the slope (and hence τ) should be the same using either Equation A.4 or A.5. For transitions in which both peaks could be fit, the lifetimes extracted using Equations A.4 or A.5 are in good agreement, which validates the use of A.5. Using Equation A.5, however, results in larger errors since the decay curve is no longer constrained to go through the point $\ln R = 1$ at $d = 0$. There are levels for which the lifetimes could be measured by more than one decay branch. For these levels, the quoted lifetime is a weighted average of the lifetimes measured from each decay path.

There are several effects which cause deviations in the measured ratio R from simple exponential decay behavior. These effects (nuclear de-orientation, feeding from higher states, solid angle effects, and different γ -ray detection efficiencies for the “fast” and “slow” peaks due to their different energies) were corrected using a modified version of the computer code ORACLE [101]. Additional modifications [100], beyond those mentioned in Ref. [93], were made to the code ORACLE to include the ability for the code to handle non-sequential decay patterns, such as for bands that have both $\Delta J=1$ (cascade) and $\Delta J=2$ (crossover) transitions. Examples of the decay curves, showing the raw data along with the data corrected for the above mentioned effects and fitted lifetimes, are shown in Figures A.3, A.4, and A.5.

In the present work, the lifetimes of the lowest 10 levels in the $K=\frac{7}{2}^-$ ground band and the lowest 6 levels in the $K=\frac{11}{2}^-$ band were measured. A total of 23 observed transitions were strong enough to yield lifetime information, 15 of these were GSB

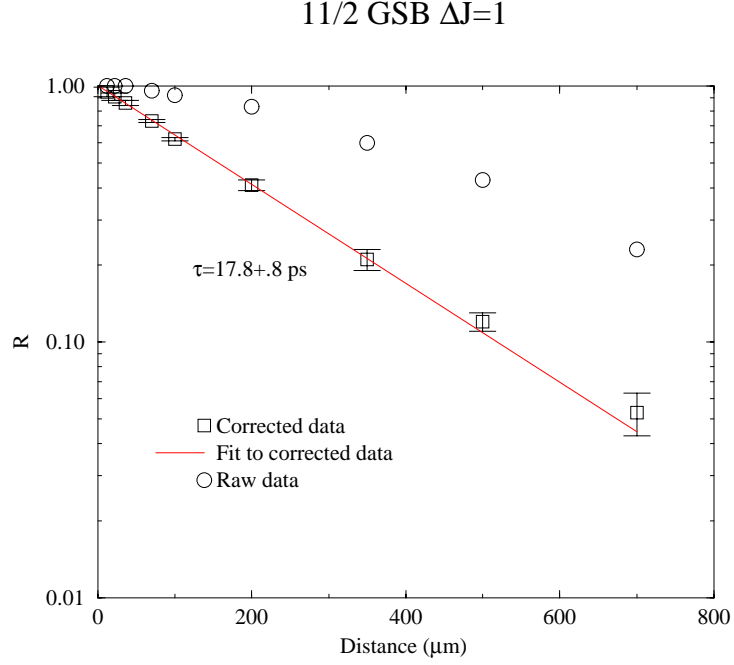


Figure A.3: Lifetime of the $\frac{11}{2}$ GSB level measured from the $\frac{11}{2}$ GSB \rightarrow $\frac{9}{2}$ GSB transition

transitions, and 8 were $K=\frac{11}{2}^-$ transitions. Peak intensities of the “fast” and “slow” component of the transitions were used where possible. For the $\frac{19}{2} \rightarrow \frac{15}{2}$ $\Delta J=2$, $\frac{17}{2} \rightarrow \frac{15}{2}$ $\Delta J=1$, and the $\frac{15}{2} \rightarrow \frac{11}{2}$ $\Delta J=2$ transitions in the $K=\frac{11}{2}^-$ band the fast peak could not be fit and the lifetimes were measured using the ratio R as defined in Equation A.5.

The measured lifetimes are shown in Tables A.2 and A.3. These lifetimes are in good agreement with published values [99] and the results from the Coulomb excitation work [90]. That is the present recoil distance lifetime measurement provides independent confirmation of the validity of the earlier Coulomb excitation results.

A.3 Matrix elements derived from the lifetime measurement

The determination of the electro-magnetic transition matrix element from level lifetimes, in principle, is straight forward if the decay branching ratios, transition

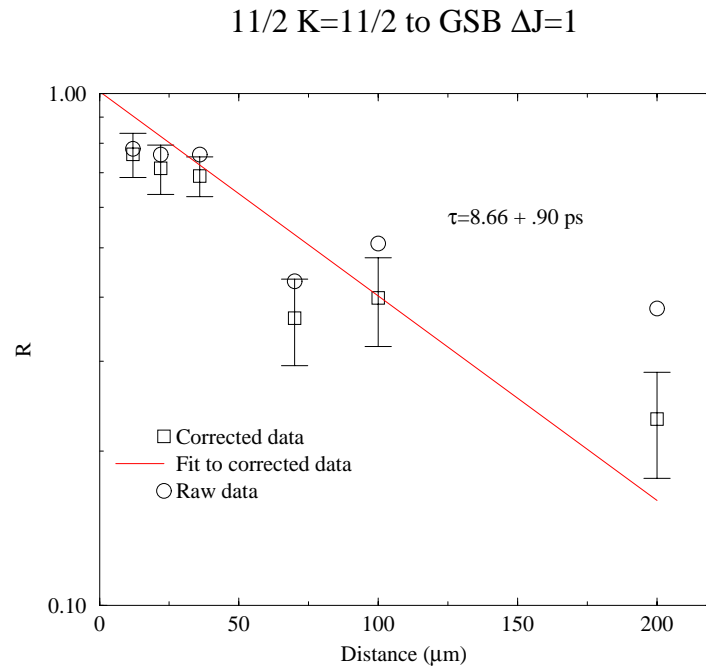


Figure A.4: Lifetime of the $\frac{11}{2} \text{ } K=\frac{11}{2}$ level measured from the $\frac{11}{2} \text{ } K=\frac{11}{2} \rightarrow \frac{9}{2} \text{ GSB}$ transition

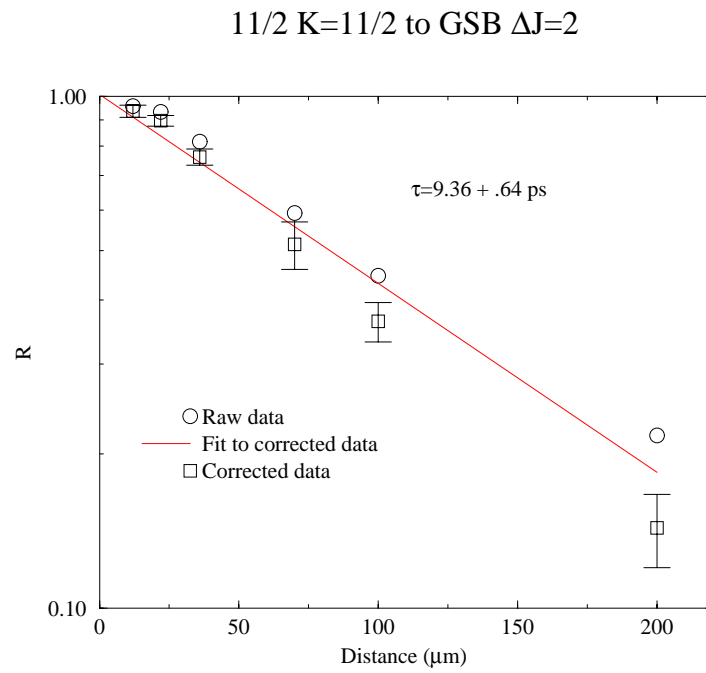


Figure A.5: Lifetime of the $\frac{11}{2} \text{ } K=\frac{11}{2}^-$ level measured from the $\frac{11}{2} \text{ } K=\frac{11}{2} \rightarrow \frac{7}{2} \text{ GSB}$ transition

Ground Band Transitions					
transition		Recoil Distance		Vogt [90](ps)	Nucl. Data Sheets [99] (ps)
level	type	measured τ (ps)	average τ (ps)		
$\frac{27}{2}^-$	$\Delta J=2$	$1.14 \pm .12$	$1.14 \pm .12$	$0.91 \pm .005$	
$\frac{25}{2}^-$	$\Delta J=2$	$1.16 \pm .05$	$1.29 \pm .24$	$1.15 \pm .04$	
	$\Delta J=1$	$1.76 \pm .10$			
$\frac{23}{2}^-$	$\Delta J=2$	$1.83 \pm .09$	$1.87 \pm .08$	$1.63 \pm .06$	
	$\Delta J=1$	$2.00 \pm .15$			
$\frac{21}{2}^-$	$\Delta J=2$	$2.52 \pm .10$	$2.52 \pm .10$	$2.10 \pm .08$	
$\frac{19}{2}^-$	$\Delta J=2$	$3.75 \pm .12$	$3.88 \pm .14$	$3.27 \pm .01$	
	$\Delta J=1$	$4.02 \pm .12$			
$\frac{17}{2}^-$	$\Delta J=2$	$5.47 \pm .14$	$5.61 \pm .14$	$5.18 \pm .03$	
	$\Delta J=1$	$5.76 \pm .16$			
$\frac{15}{2}^-$	$\Delta J=2$	$6.56 \pm .18$	$7.26 \pm .82$	$8.07 \pm .05$	
	$\Delta J=1$	$8.21 \pm .21$			
$\frac{13}{2}^-$	$\Delta J=1$	$12.23 \pm .64$	$12.23 \pm .64$	$10.22 \pm .07$	
$\frac{11}{2}^-$	$\Delta J=1$	$17.83 \pm .83$	$17.83 \pm .83$	$19.37 \pm .13$	$18.47 \pm .87$
$\frac{9}{2}^-$	$\Delta J=1$	34.4 ± 1.4	34.4 ± 1.4	$32.16 \pm .45$	$31.74 \pm .57$

Table A.2: ^{165}Ho Ground Band Lifetimes

$K=\frac{11}{2}^-$ Band Transitions					
transition		Recoil Distance		Vogt [90](ps)	Nucl. Data Sheets [99] (ps)
level	type	measured τ (ps)	average τ (ps)		
$\frac{19}{2}^-$	$\Delta J=1$	$2.43 \pm .28$	$2.51 \pm .30$	$1.97 \pm .11$	
	$\Delta J=2$	3.6 ± 1.0			
$\frac{17}{2}^-$	$\Delta J=1$	$2.79 \pm .69$	2.79 ± 0.69	$2.38 \pm .36$	
$\frac{15}{2}^-$	$\Delta J=2$	5.5 ± 1.5	5.7 ± 1.1	$3.16 \pm .23$	
$\frac{13}{2}^-$	$\Delta J=2$ to GSB	6.0 ± 1.7	$6.32 \pm .60$	5.8 ± 1.1	
	$\Delta J=2$ to GSB	$6.32 \pm .60$			
$\frac{11}{2}^-$	$\Delta J=1$ to GSB	$8.66 \pm .90$	$9.12 \pm .52$	11.9 ± 1.3	10.5 ± 2.7
	$\Delta J=2$ to GSB	$9.36 \pm .64$			

Table A.3: ^{165}Ho $K=\frac{11}{2}$ Band Lifetimes

multipolarities, and mixing ratios for all the decay paths are known. In the RDM experiment, the decay branching ratios can be reconstructed from the measured γ -ray yields, but no measure of the E2/M1 mixing ratios for the $\Delta J=1$ transitions are made. However, with a few reasonable assumptions, it is possible to set limits on the electro-magnetic matrix elements.

The quantities actually measured in this experiment are $y(0^\circ)$, the γ -ray yields at 0° . These γ -ray yields for the various decay paths de-exciting a given level were measured by adding the intensities of the slow and fast ($I_s + I_f$) peaks in the γ -spectrum summed over all distances. For the transitions where the fast peak could not be fit, the fast peak intensities were calculated by:

$$I_f = I_s \cdot \frac{I'_f}{I'_s} \quad (\text{A.6})$$

where the I' are intensities of clean decay branches originating from the same level. These γ -ray intensities were then corrected for the energy efficiency, ϵ , of the γ -ray detector at the energy of the observed γ ray and for the angular distribution, $W(0^\circ)$, of the γ ray. The angular distribution correction factors were calculated with the Coulomb excitation code GOSIA. The corrected γ -ray intensities are given by:

$$I_i = \frac{y(0^\circ)}{\epsilon_i W(0^\circ)} \quad (\text{A.7})$$

A part of the decay for a given branch proceeds through internal conversion and is unobserved by the γ -ray detectors in this experiment. Thus, the branching ratios (BR) are given by

$$BR_i = \frac{I_i \cdot (1 + \alpha_i)}{\sum_l I_l \cdot (1 + \alpha_l)} \quad (\text{A.8})$$

where the α_i are the internal conversion coefficients as calculated in Ref. [102]. The electro-magnetic part of the partial width for a specific decay path now is given by

$$\Gamma_{iEM} = \frac{BR_i \cdot \hbar}{(1 + \alpha_i) \cdot \tau_i} \quad (\text{A.9})$$

For $\Delta J=2$ transitions, which have pure E2 multipolarity, this partial decay width is directly related to the transition probability $B(E\lambda)$ and, hence, also is related to

the square of the matrix element. For the $\Delta J=1$ mixed multipolarity transitions, the electric and magnetic partial decay widths can be separated by

$$\Gamma_{EM} = \Gamma_{E2} + \Gamma_{M1} = \Gamma_{E2}(1 + \delta^{-2}) \quad (\text{A.10})$$

where δ is the E2/M1 mixing ratio of the transition. Since this experiment made no measure of the mixing ratio, it is necessary to add an additional constraint to the $\Delta J=1$ transitions in order to have enough information to set limits on the matrix elements. For all in-band transitions in both the $K=\frac{7}{2}^-$ and the $K=\frac{11}{2}^-$ band the $\langle J || E2 || J-1 \rangle$ matrix element was allowed to vary between 0 to 2 times the value given by the rotor relation:

$$\langle J || E2 || J-1 \rangle = \sqrt{2 \cdot (J-1) + 1} \langle (J-1)K20 || JK \rangle \sqrt{\frac{5}{16\pi}} eQ_0 \quad (\text{A.11})$$

with $eQ_0=7.67$ eb [99]. No constraints were placed on the E2/M1 mixing ratios for the $\Delta J=1$ inter-band ($K=\frac{11}{2}^-$ band to $K=\frac{7}{2}^-$ band) transitions. These transitions were allowed to vary in multipolarity from pure M1 to pure E2. The limits on the transition matrix elements were calculated with these constraints.

A.3.1 Ground Band Matrix Elements

The derived electric and magnetic in-band matrix elements for the ground band from the RDM lifetime measurement experiment and from the Coulomb excitation experiments are shown in Figures A.6 and A.7, respectively. The results from the two experiments are in reasonable agreement. The measured electric and magnetic matrix elements from both experiments show good agreement with the axially symmetric rotor model with an intrinsic quadrupole moment of $eQ_0=7.67$ eb and a difference in gyromagnetic factors of $(g_K - g_R) = 0.93 \pm 0.01$.

A.3.2 $K=\frac{11}{2}^-$ In-Band Matrix Elements

The matrix elements from the Coulomb excitation and RDM experiments for the $K=\frac{11}{2}^-$ in-band transitions are shown in Figures A.8 and A.9. As mentioned

Ground Band E2 $\Delta J=2$ Matrix Elements

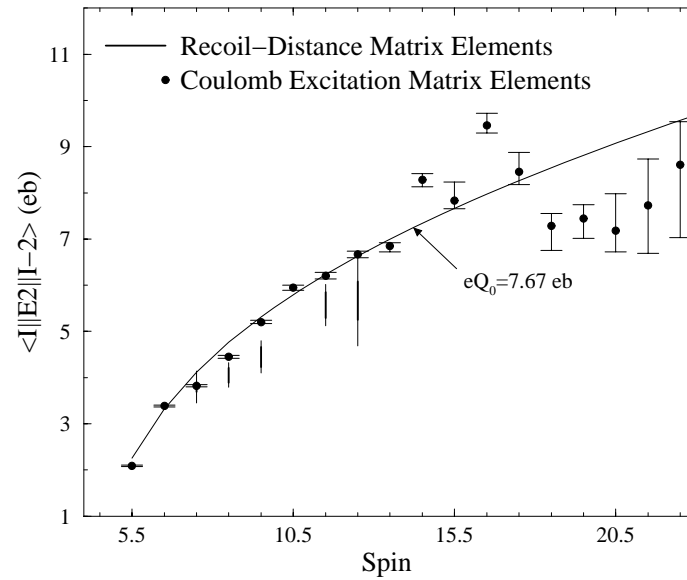


Figure A.6: Ground Band E2 matrix elements from the Coulomb excitation work and from the Recoil-Distance lifetime measurement.

Ground Band M1 $\Delta J=1$ Matrix Elements

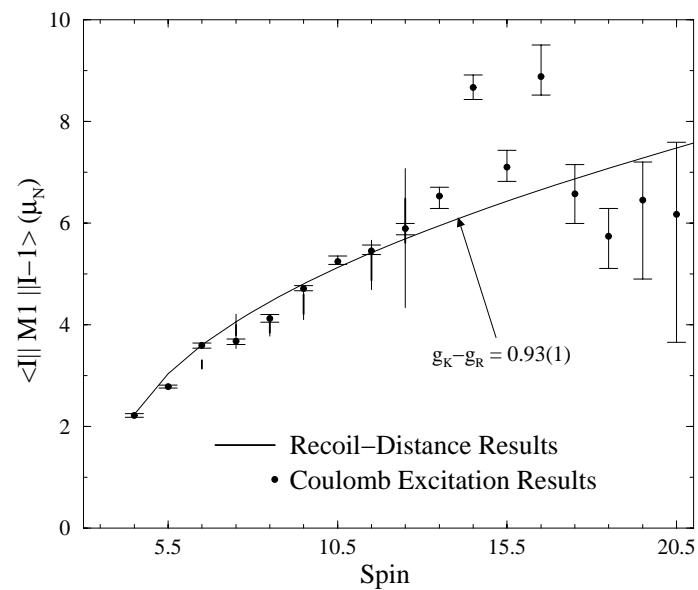


Figure A.7: Ground Band M1 matrix elements from Coulomb excitation work and Recoil-Distance lifetime measurement

K=11/2 Band Inband E2 $\Delta J=2$ Matrix Elements

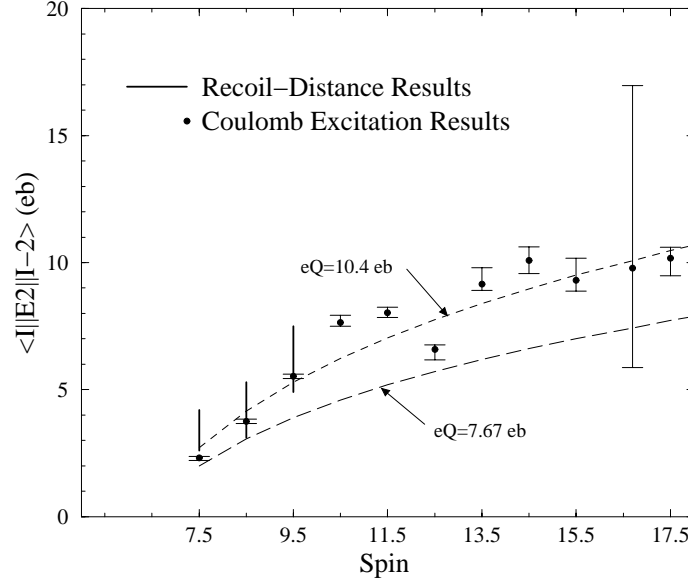


Figure A.8: E2 matrix elements for $K=\frac{11}{2}$, from $\Delta J=2$ in-band transitions

previously, the error analysis for the Coulomb excitation work has not been completed and the errors presented for the matrix elements are still preliminary. Hence, a quantitative comparison between the two data sets is not possible. The in-band $\Delta J=2$ matrix elements for the $K=\frac{11}{2}^-$ band from the RDM experiment show good agreement with the Coulomb excitation results, and are consistent with this band having a quadrupole moment $eQ_0=10.4\pm 1.2$ eb. The difference in the gyromagnetic factors for this band is $g_k - g_R = 0.90\pm 0.10$, suggesting the same microscopic structure as the ground band.

A.3.3 $K=\frac{11}{2}^-$ Band to Ground Band Matrix Elements

The $E2\Delta J=2$, $E2\Delta J=1$, and M1 matrix elements for the $K=\frac{11}{2}^-$ to $K=\frac{7}{2}^-$ ground band transitions are shown in Figures A.10, A.11, A.12. The RDM $E2\Delta J=1$ and M1 matrix elements from the $K=\frac{11}{2}^-$ band to the ground band show good agreement with the Coulomb excitation results. The derived limits for these matrix elements cover a fairly large range since no restrictions were placed on the E2/M1 mixing ratio. Thus,

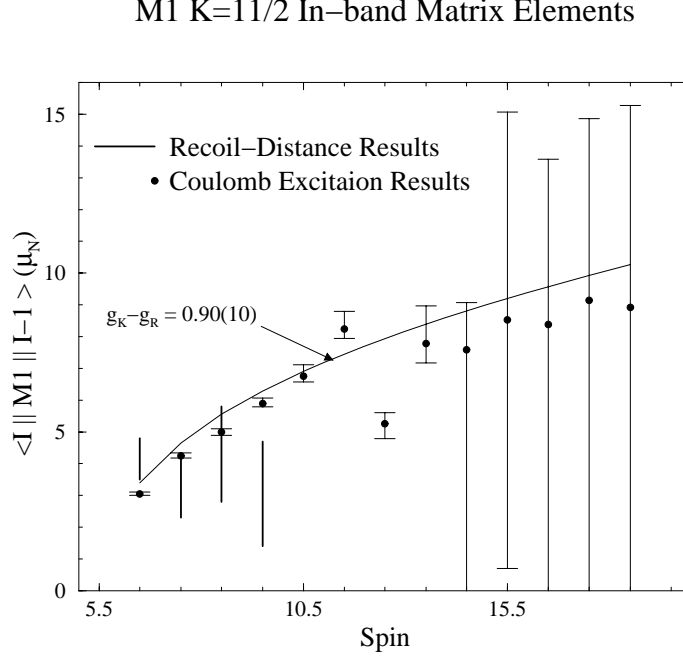


Figure A.9: $K=\frac{11}{2}$ M1 in-band matrix elements

these do not present as sensitive a comparison with the Coulomb excitation results. The $\Delta J=2$ $K=\frac{11}{2}^-$ to ground band matrix elements show only marginal agreement with the Coulomb excitation results.

A.4 Summary

The recoil-distance method was used to measure the lifetimes of the 10 lowest levels (up to spin $\frac{27}{2}$) of the ground band and the 5 lowest levels (up to spin $\frac{19}{2}$) of the $K=\frac{11}{2}^-$ band. The measured lifetimes from the recoil-distance experiment are in good agreement with the lifetimes derived from the Coulomb excitation experiments. Limits on the transition matrix elements were extracted from the lifetimes and measured γ -ray yields. These matrix elements show reasonable agreement with the results from previous Coulomb excitation experiments performed by Vogt *et al.* [90]. The results from the recoil-distance lifetime measurement are consistent with the γ -vibration $K=\frac{11}{2}^-$ band having an intrinsic quadrupole moment $eQ_0=10.4 \pm 1.1$ eb, correspond-

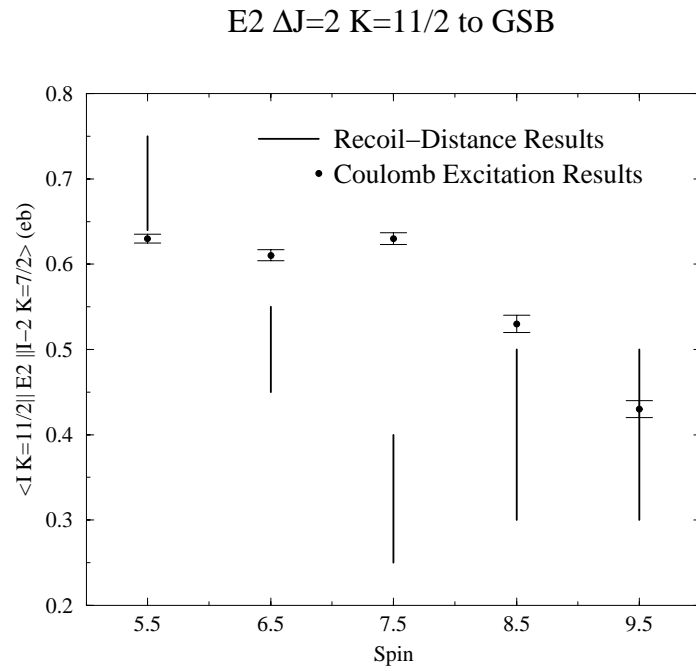


Figure A.10: E2 $\Delta J=2$ matrix elements connecting the $K=\frac{11}{2}$ band to the ground band

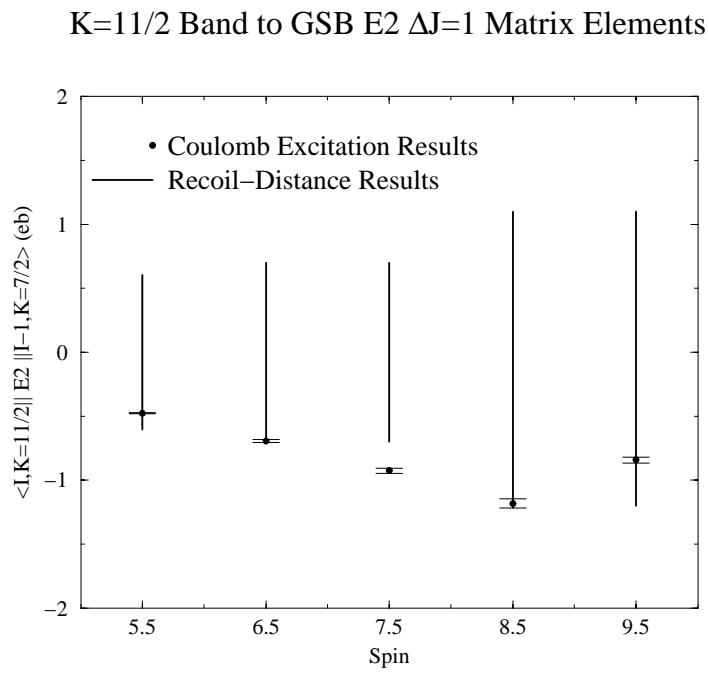


Figure A.11: E2 $\Delta J=1$ matrix elements connecting the $K=\frac{11}{2}$ band to the ground band

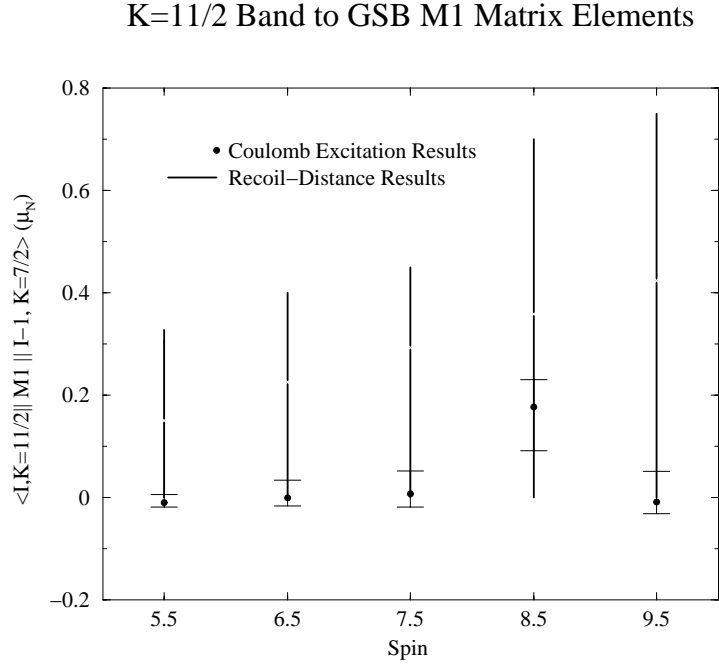


Figure A.12: M1 matrix elements connecting the $K=\frac{11}{2}$ band to the ground band

ing to an unusually large quadrupole deformation of $\beta=.43\pm.04$, which is 40% larger than the ground state band deformation. The similarity of the difference of the gyromagnetic factors $g_K - g_R$ between the ground band and the $K=\frac{11}{2}^-$ band suggests that these two bands have the same microscopic structure. The agreement between the results from the RDM experiment and Coulomb excitation experiments confirms that the surprising result of larger than expected quadrupole deformations in the γ -bands is a real effect and not an artifact of the Coulomb excitation analysis. Further investigation is required to understand the origin of the anomalously large deformation observed in the γ -vibrational bands of ^{165}Ho .

Appendix B

Gammasphere Calibration

The method for calibrating the energy and relative efficiency of the Ge the energy of BGO elements of the GAMMASPHERE array are described in this appendix.

B.1 Energy and Efficiency Calibration

The energy spectra of the individual Ge detectors were calibrated using ^{182}Ta and ^{152}Eu sources. A sample calibration curve is shown in Figure B.1. The intrinsic energy resolution of the GAMMASPHERE array was obtained from the measured full-width-half-maximum of the peaks in the summed energy spectra, and these were fit to the formula given in 4.7. The result is shown in Figure B.2. The relative energy efficiency of GAMMASPHERE was measured from the intensities of the γ -ray peaks in the summed calibration data, and is shown in Figure B.3. The relative efficiency measurement was performed with 0.127 mm Cu and 0.127mm Ta absorber over Ge detectors.

The energy spectra of the BGO detectors were calibrated using a ^{88}Y source. The resultant summed spectra of all the BGO elements is shown in Figure B.4. The energy resolution of the BGOs is 18%.

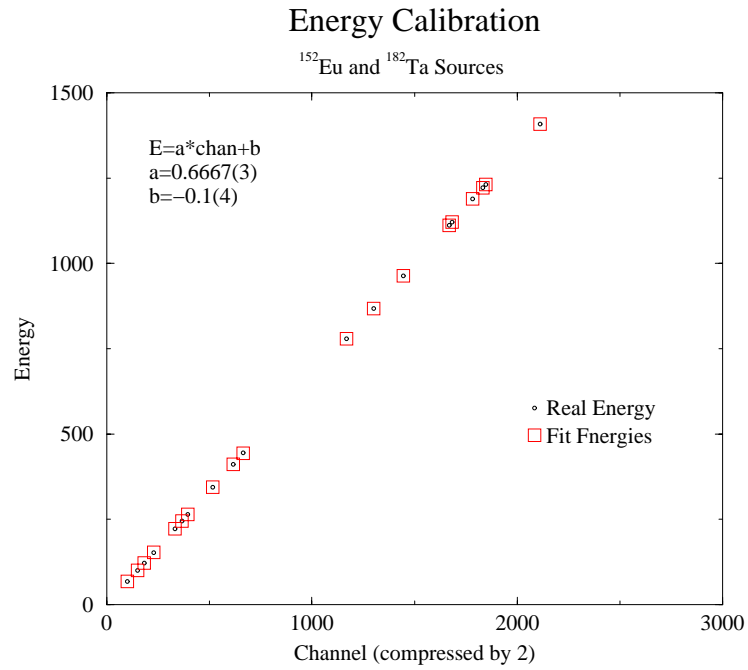
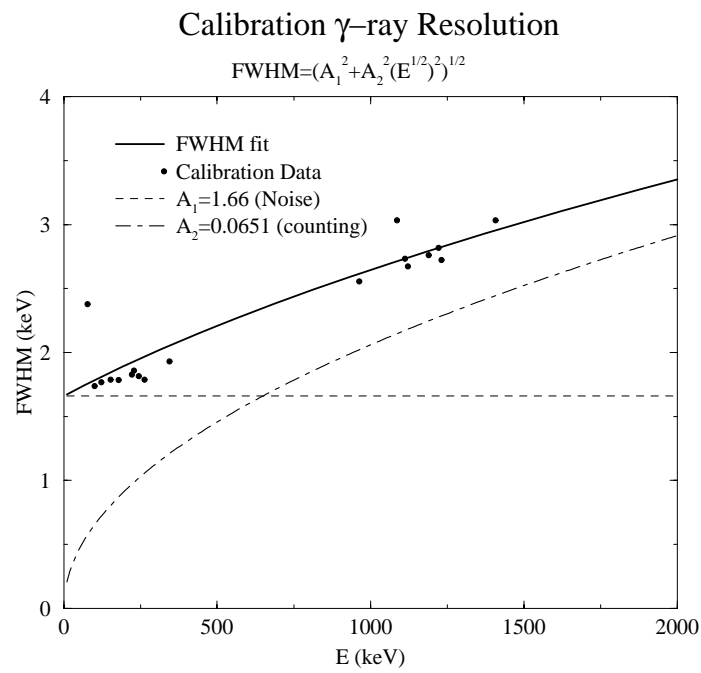


Figure B.1: Energy Calibration curve for GAMMASPHERE.

Figure B.2: Intrinsic γ ray energy resolution for GAMMASPHERE

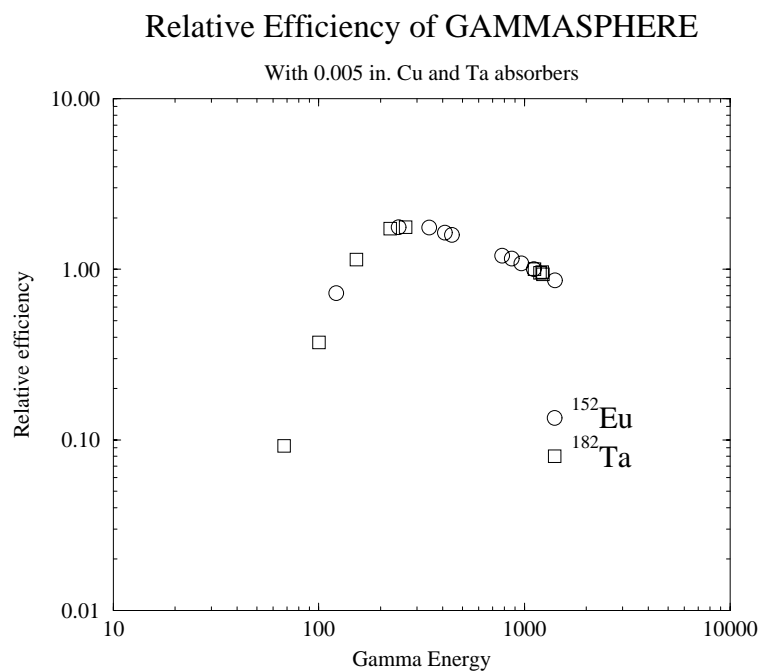


Figure B.3: Relative efficiency curve for GAMMASPHERE.

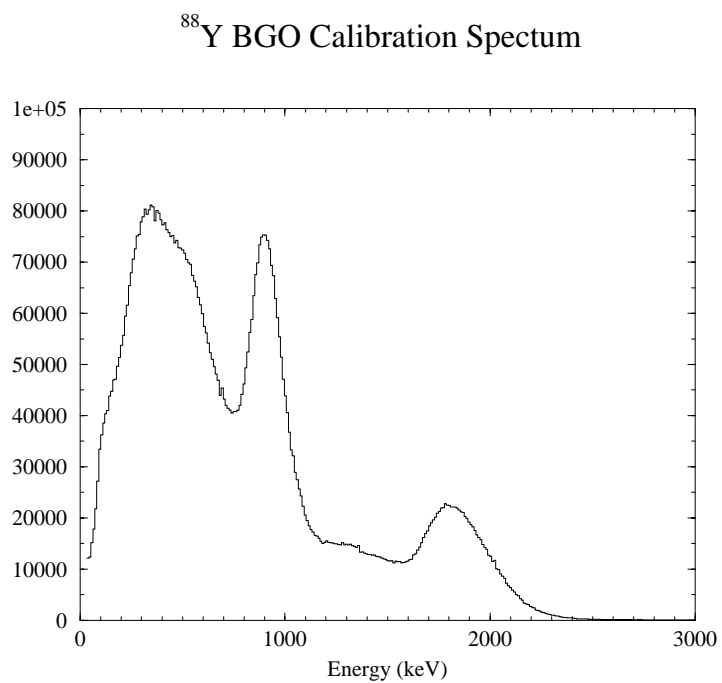


Figure B.4: BGO calibration spectra. The spectrum shown is the sum of all the BGO elements of the GAMMASPHERE array.